University College of Southeast Norway
Faculty of Technology, Natural Sciences
and Maritime Sciences

Doctoral dissertation no. 21
2017

Sindre Tøsse

The rapid depressurization and evaporation of liquified carbon dioxide

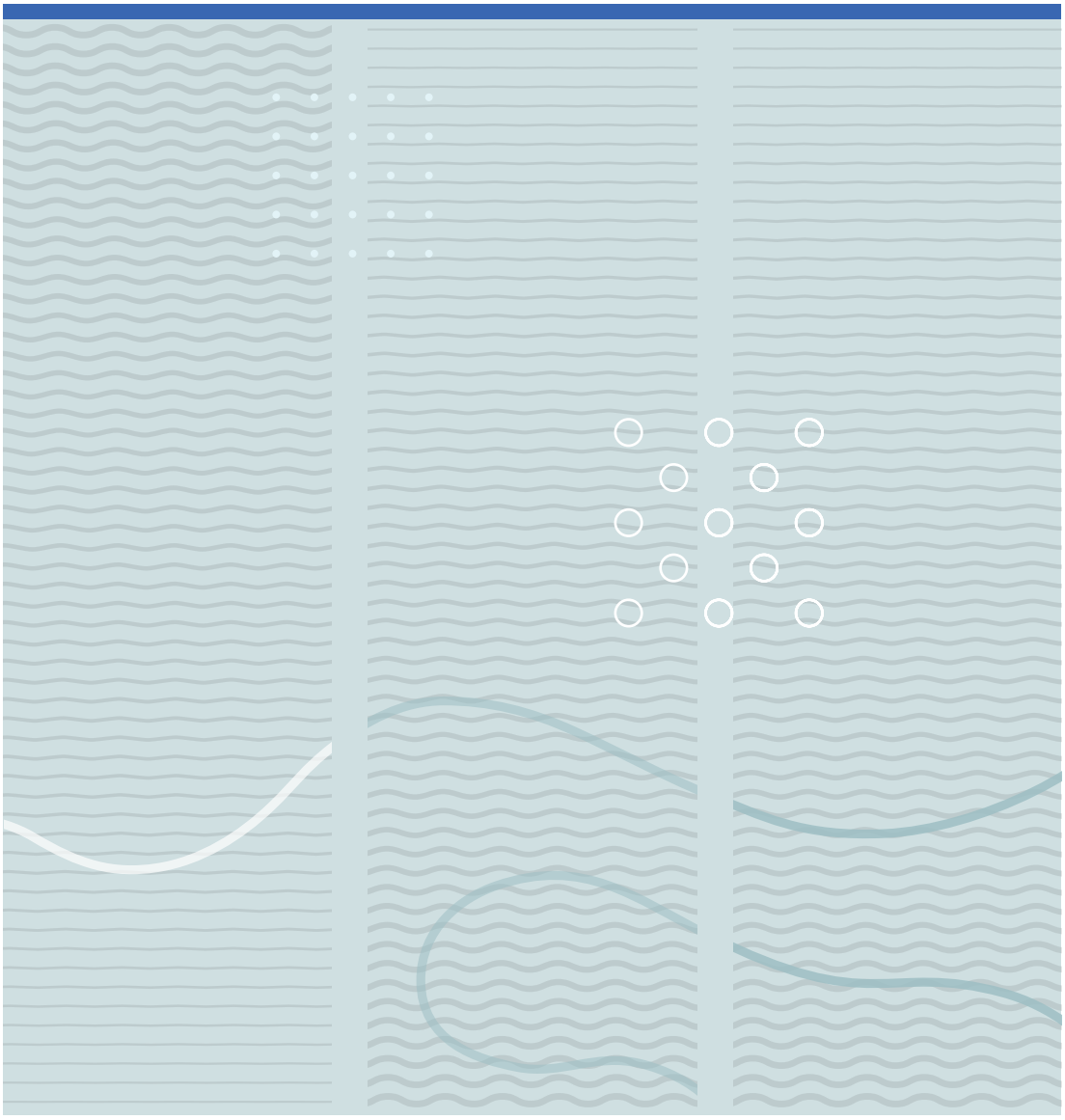

HSN

Sindre Tøsse

The rapid depressurization and evaporation of liquified carbon dioxide

A PhD dissertation in
Process, Energy and Automation Engineering

Faculty of Technology, Natural Sciences and Maritime Sciences
University College of Southeast Norway
Kongsberg, 2017
Doctoral dissertations at the University College of Southeast Norway no. 20

ISSN: 2464-2770 (print)
ISSN: 2464-2483 (electronic)
ISBN: 978-82-7206-435-7 (print)
ISBN: 978-82-7206-436-4 (electronic)

Print: **University College of Southeast Norway**

Acknowledgments

This thesis is dedicated to my wife Ragnhild and my son Brage.

I would like to express my sincere gratitude towards my supervisor Knut Vågsæther for his advice and guidance towards this work. I would also like especially thank my co-supervisor Dag Bjerketvedt for his valuable input. I would also like to thank my co-supervisor Bjørn Helge Hjertager and the University of Stavanger for being very helpful in providing me with office facilities.

I am very grateful for being welcomed into the process safety research group at Telemark Process Safety and Combustion Lab. In addition to Knut and Dag, André Gaathaug, Joachim Lundberg and Per Morten Hansen made my time at USN memorable and filled with laughter.

I am grateful to my colleagues at Lloyd's Register Consulting Stavanger and Lyse Innovation who have been very supportive towards the end of my work with the thesis.

Contents

Nomenclature

Abbreviations

EOS	Equation of state
SEM	Spinodal Equilibrium Mixture
SG	Stiffened gas
vdW	Van der Waals

Constants

π_M	The mathematical constant π
M	Molar mass [kg/mol]
R	Specific gas constant ($\equiv R_M/M$) [J/(kg K)]
R_M	Molar gas constant [J/(mol K)]

Greek Symbols

α	Volume fraction
δ	Reduced volume
ϵ	Reduced internal energy
γ	Stiffened gas: Heat capacity ratio ($\equiv c_p/c_v$)
γ	Van der Waals: reduced Gibbs free energy
ϕ	Reduced Helmholtz free energy
π	Reduced pressure
ρ	Density [kg/m^3]
τ	Reduced temperature
ξ	Volume fraction pure phase limit
ξ_I	Volume fraction interface limit

Roman Symbols

c	Speed of sound [m/s]
c_p	Isobaric heat capacity [J/K]
c_v	Isochoric heat capacity [J/K]
E	Total energy ($\equiv e + \frac{1}{2}\rho u^2$) [J]

e Internal energy [J]

f Helmholtz free energy [J]

g Gibbs free energy [J]

h Enthalpy [J]

p Pressure [Pa]

s Entropy [J/K]

u Velocity [m/s]

v Specific volume ($\equiv 1/\rho$) [Pa]

Y Mass fraction

Subscripts

sat Saturation

c Critical

H Hugoniot

s Spinodal

Notation and definition of terms

In the context of a two phase mixture, variables without a subscript are mixture variables. An exception to this is the volume fraction α and the mass fraction Y, which denotes vapor volume and mass fractions when no subscript is used.

Thermodynamics

Binodal curve
: The binodal curve is defined as the loci of all vapor-liquid states that are in thermodynamic equilibrium

Spinodal curve
: The spinodal curve is defined as the loci of $\left(\frac{\partial p}{\partial v}\right)_T = 0$

Spinodal state
: A state that lies on the spinodal curve

Sub-spinodal region
: The region in p-v space with pressure below the spinodal. Sometimes referred to only as the spinodal region

Spinodal-equilibrium curve
: The spinodal-equilibrium curve is defined as the loci of all states that are in thermal and mechanical equilibrium with the spinodal states.

Spinodal equilibrium mixture
: A two phase mixture where one phase is in the spinodal state and both phases are in thermal and mechanical equilibrium.

Numerical terms

Numerical vapor/liquid
: Vapor or liquid that is generated in order to maintain a physically valid solution, as part of the spinodal equilibrium mixture equation of state

True vapor/liquid
: Vapor or liquid generating numerical liquid or vapor, as part of the spinodal equilibrium mixture equation of state

Cell vapor/liquid
: The two phases in a computational cell. May refer to a mixture of true vapor and numerical liquid or true liquid and numerical vapor

Chapter 1

Introduction

1.1 Motivation

In the context of carbon capture and storage (CCS), pressurized carbon dioxide is stored in liquid form. This can pose a significant safety hazard, as the amount of energy in even a small vessel is sufficient to cause structural damage and even fatal accidents. In addition, the dispersion of CO_2 can cause suffocation accidents in enclosed or semi-enclosed areas. A structural failure in a pressurized vessel containing liquefied gas can cause a rapid vaporization and expansion process that is referred to as a BLEVE (Boiling Liquid Expanding Vapor Explosion). If the released substance is chemically inert or not ignited, the process is often referred to as a cold BLEVE. The phase transition and expansion process is governed by complex thermodynamics and kinetics. Knowledge about this process is vital in the prevention and mitigation of accidents in storage and transport of pressurized liquid gas.

An idealized schematic of the expansion of saturated liquid and vapor with the onset of an evaporation wave is shown in figure 1.1. This one-dimensional problem will be explored both experimentally and numerically in the present work. Note that this situation does not fit the definition of a BLEVE. However, the research is still relevant for BLEVE-type scenarios as the governing kinetics and thermodynamics are the same.

Computational Fluid Dynamics (CFD) is used in a broad range of fields, ranging from spacecraft engineering to process plant safety. It is a very efficient tool for investigations involving fluid flow. By using a computer to simulate such problems, one is able to conduct numerical experiments, varying individual parameters systematically. In addition, problems too complex to solve analytically can be explored using various numerical methods. Nevertheless, the numerical representation of a real situation will always be inaccurate, due to the limited precision of a computer and inaccuracies in the numerical modelling. Because of this, CFD should not be regarded as a substitute to theoretical or experimental methods, but rather as a supplement to such [1].

In the context of process safety, CFD is frequently used to model dispersion of gas from accidental releases from process equipment, as well as fire and/or explosion modelling. The length scale of industrial scale applications are often on the order of 100 m, with typical computational cell sizes on the order of 1 m. To facilitate such coarse computational grids, sub-grid models are used. An example of this is the Reynolds-Averaged Simulation (RAS) that is used to handle turbulence effects by a range of commercial software. Using this model, averaged flow variables are used in the numerical resolution of the flow field. The effect of the fluctuations from the average values (turbulence) are accounted for by various models, e.g. the $k - \epsilon$ model for high Reynolds number flow. There are two main reasons for using sub-grid models. The first, and perhaps the most obvious, is the need to have as few computational cells as possible. It is not practically possible to resolve industrial scale problems with the numerical resolution needed to resolve the smallest turbulent eddies in the flow (Direct Numerical Simulation - DNS). This would require a cell size on the order of millimeters and below. Decreasing the cell size from meters to millimeters would require 10^9 times the number of computational cells. Since the computational time step is proportional to the cell size by the CFL-condition, the number of time steps would be increased by a factor of 10^3. The time needed to resolve the numerical problem would thus be increased by at least a factor of 10^{12}. Such an approach is certainly not practical, however it is also not necessary,

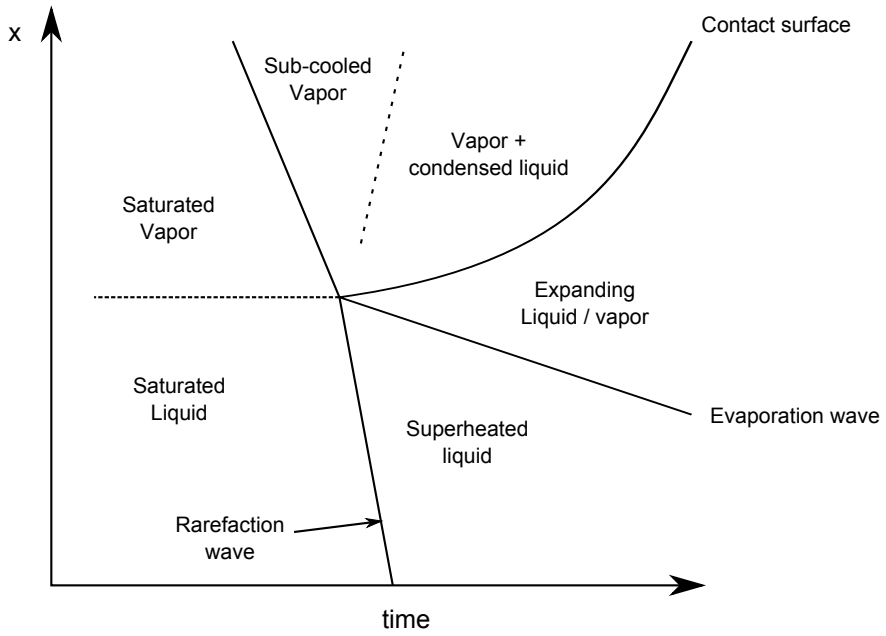

Figure 1.1: x-t overview of the depressurization of saturated vapor and liquid. Note that the wave speeds are not to scale.

which leads to the second reason for using sub-grid models. In most cases, the detailed resolution of the turbulent eddies are not of any practical interest. It is sufficient to treat turbulent fluctuations as stochastic variables and only resolve the averaged flow field. Hence, the sub-grid model utilizes a general assumption about the behavior a phenomenon, eliminating the need to solve the "same" problem over and over again.

In some incompressible commercial CFD-software (KFX, FLACS), under-expanded jet leaks are modeled by the super-cell approach. The under-expanded jet has a complex structure with rarefaction and compression waves, as shown in fig. 1.2. To resolve this structure numerically, a compressible solver with fine spatial and temporal resolution is needed. This is not feasible in industrial scale calculations. Instead, the conditions at the Mach disk are calculated and used as source terms in a super-cell, correcting for entrainment of surrounding air. The super-cell method for implementing under-expanded jet leaks demonstrates the need for detailed knowledge about complex flow structures in order to develop sub-grid models to be applied in industrial scale numerical calculations. When it comes to releases from a reservoir of liquefied gases, a similar approach may be chosen. A multi-phase numerical solver with detailed thermodynamics and kinetics is needed to resolve the immediate vicinity of the leak. If the leak is very rapid, so that equilibrium cannot be maintained inside the equipment (e.g. equipment structural failure), the inside may need to be resolved numerically. However, the level of detail needed to resolve the flow situation, both in terms of spatial/temporal resolution and thermodynamics is neither feasible nor needed for the entire computational domain. Additionally, the multi-phase flow situation in the failing equipment spans the whole region from pure liquid to pure vapor, so that an Eulerian two fluid model is needed. Further away from the leak, it is sufficient to model liquids and solids as dispersed particles/droplets using a Lagrangian model. This is illustrated in fig. 1.3.

The focus of this thesis is to develop a numerical model capable of resolving the two-phase flow situation in the depressurization of a vessel containing liquefied gas, as illustrated by the red borders in fig. 1.3. Sublimation of solid particles will not be addressed, since liquid-vapor interaction is the dominant process inside and in the immediate vicinity of the vessel. However, the sublimation of solids is assumed to play a major role in the dispersion of vapor to the surroundings and should be a part of a complete liquefied gas dispersion model. In order to get the necessary level of accuracy in the thermodynamic calculations, a non-monotonic equation of state is chosen. For CO_2, the most accurate liquid-vapor EOS available is the Span-Wagner multiparameter EOS [2]. It would be extremely challenging to implement this type of EOS into a numerical code, but the author regards this as the end-goal of the present work.

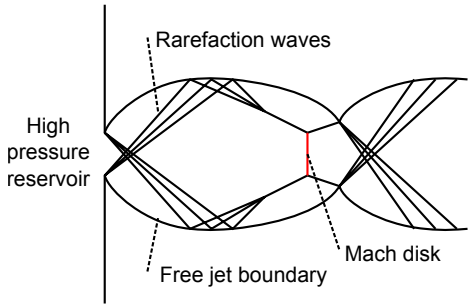

Figure 1.2: The structure of an under-expanded jet

The usage of a non-monotonic EOS in a numerical solver raises a number of issues, since both the liquid and vapor states have a limited region of existence. In order to deal with these issues, the simplest form of a non-monotonic EOS, namely the cubic van der Waals EOS, is used in the development of a numerical code. Menikoff and Plohr [3] state that the Maxwell equal-area rule must be applied to modify the equation of state in order to avoid imaginary speed of sound in the van der Waals loop. Saurel et al. [4] propagate the misconception that the square speed of sound is negative in the spinodal zone. In the present work however, a less strict method is applied to allow metastable states, while maintaining a real speed of sound.

While quantitatively inaccurate, the van der Waals equation of state provides a qualitative representation of every major feature of real gas behavior. Combined with its simple formulation, this makes it an often used EOS in model development and academic work. In numerical fluid dynamics, very few two-phase solvers use a single non-monotonic equations of state to model both phases because of the complexity of the algorithms needed. Still, in problems involving metastable states and rapid phase transitions, this may be necessary to describe the process in a physically accurate way. Using a non-monotonic equation of state in a numerical solver raises a number of issues. It is therefore necessary to develop robust solving algorithms that are capable of handling two phase flow in the vicinity of spinodal states. The van der Waals EOS is chosen to develop a proof of concept, because its simple formulation allows for analytical expressions for many thermodynamic parameters, e.g. the spinodal curve.

1.2 Litterature

There are several definitions of the term BLEVE, an overview of which is provided by Abbasi and Abbasi [5]. Some of the definitions involve complete failure of the vessel, like the one given by Birk et al. [6]: *A BLEVE is the explosive release of expanding vapour and boiling liquid when a container holding a pressure liquefied gas fails catastrophically.* Birk et al. notes that a BLEVE fits the definition of an explosion because it generates a shock wave. They do however state that the shock is likely caused by the vapor space at the initial opening of the vessel, and thus is not a product of the evaporating liquid. They also make the important notion that the BLEVE does not cause the tank rupture, but rather is a result of the sudden opening of the vessel. Experimental results from a 2000 l container of propane clearly shows a weak shock wave that overtakes the cloud release following the tank rupture.

There has been some discussion of the importance of homogeneous nucleation in explosive evaporation. It is not clear whether the evaporation of the superheated liquid is fast enough to create a shock. Reid [7] claims that explosive evaporation can only occur when the initial temperature of the pressurized liquid exceeds the superheat limit temperature. The superheat limit temperature is defined as the lowest saturation temperature where the superheat limit can be reached at atmospheric pressure. Two different definitions of the superheat limit exists, namely the thermodynamic superheat limit (TSL) and the kinetic superheat limit (KSL). The former follows the definition of cubic equations of state, as the lowest possible pressure where a liquid can exist for a given temperature. It is defined by the spinodal curve. The kinetic superheat limit is defined as the state when vapor nuclei are spontaneously generated without the presence of nucleation sites. This process is discussed in great detail by Debenedetti [8].

The superheat limit theory imposes strict requirements for the creation of a BLEVE. As Birk et al. [6]

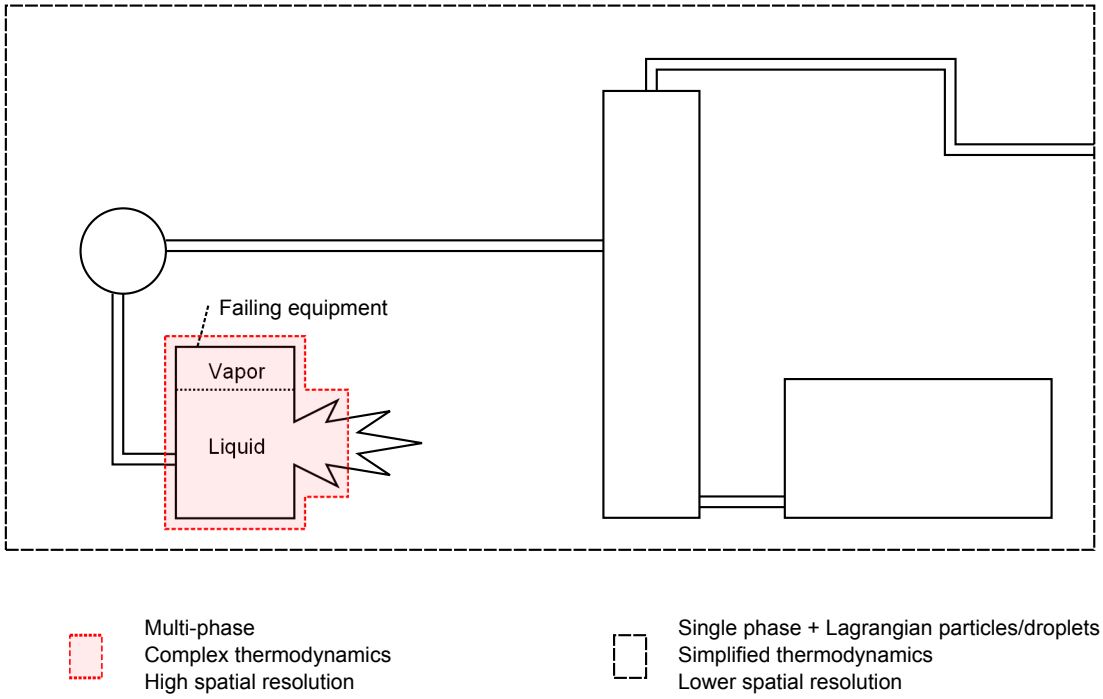

Figure 1.3: Numerical resolution of a process plant with structural failure in a container with liquefied gas.

points out, reaching the superheat limit in a real world situation is highly unlikely. In lab experiments, great care is needed to suppress nucleation sites on walls and impurities so that the limit of superheat can be reached. The violent nature of a large scale BLEVE makes it very difficult to obtain precise measurements of the kinetic and thermodynamic conditions inside the vessel at the time of rupture. It is however reasonable to assume that heterogeneous nucleation plays a major role in any large scale scenario with total loss of containment. It is likely that this will prevent the bulk of the liquid to reach atmospheric pressure, and thus downplay the importance of the superheat limit temperature as a criterion for BLEVEs.

Due to the difficulty of obtaining accurate experimental data on the kinetic and thermodynamic processes at work in a BLEVE, numerical simulations can be an appropriate tool for better understanding. By carefully developing a numerical model capable of handling metastability and finite rate phase transition one can examine in detail the levels of superheat that are generated in rapid de-pressurization of saturated liquids. Such a model would need extensive experimental validation, both in simple setups like evaporation tubes and more complex ones involving near-field monitoring of regular BLEVEs.

Evaporation waves are a less violent phenomenon than BLEVEs, but similar in the sense that pressure liquefied gas undergoes a rapid de-pressurization so that it enters a metastable state. Rather than violent bulk evaporation, the liquid evaporates in a narrow well defined region that propagates into the upstream superheated liquid, generating a high velocity mixture of vapor and liquid droplets or solid particles. From a numerical perspective, this is a much simpler situation, since it can be approximated as a one-dimensional phenomenon. The thermodynamic and kinetic processes that govern evaporation waves are assumed to be similar to a BLEVE-type scenario. Modelling an evaporation wave numerically is therefore an important step in being able to model a BLEVE in detail.

There have been a number of experimental publications on evaporation waves. Grolmes and Fauske [9] observed evaporation waves in water, refrigerant 11 and methyl alcohol in tubes with diameters from 5 mm to 380 mm. They found that the onset of evaporation waves was dependent on initial degree of superheat and tube diameter. Das et al. [10] found that the boiling front velocity varied linearly with the degree of superheat and the cross-sectional area of the tube, and decreased with impurities in the liquid. They proposed a model for the front propagation involving mixing of small bubbles by turbulent eddies.

Reinke and Yadigaroglu [11] did a series of experiments with explosive vaporization in propane, butane and refrigerant R-134a int tubes with diameters from 14 mm to 80 mm. They did not find any significant influence of the cross-sectional area on the boiling front velocity, except when the tube diameter was on the same order as the scale of the bubbly structures in the boiling front. Bjerketvedt et al. [12] conducted a series of small-scale experiments with CO_2 BLEVEs.

Thompson et al. [13] described evaporation waves as a wave-splitting phenomenon, where a single pressure discontinuity is split into a de-pressurization wave and an evaporation wave. The de-pressurization wave is described as an acoustic expansion wave and the evaporation wave propagation velocity is approximated by the Chapman-Jouguet condition for deflagration. The C-J deflagration analogy was also discussed by Hill [14], who did a series of studies on evaporation waves in a superheated liquid (Refrigerant 12 and 114). Simoes-Moreira and Shepherd [15] also performed a series of experiments with superheated dodecane, on which the C-J jump conditions were discussed.

Some work has been done to develop numerical models that are capable of describing evaporation waves. Saurel et al. [16] developed a Godunov method for compressible multiphase flow that was later applied to the subject of phase transition in metastable liquids [4]. They were able to qualitatively reproduce the evaporation front velocities measured by Simoes-Moreira and Shepherd. Zein et al. [17] used the same numerical model to reproduce the results of Simoes-Moreira and Shepherd with better accuracy. Yeom and Chang [18] later modified the HLLC scheme used by Zein et al. Romenski et al. [19] used the GFORCE and GMUSTA fluxes in conjunction with the MUSCL-Hanckock method with different levels of pressure relaxation. They presented a hierarchy of one-dimensional two-phase governing equations with varying thermodynamic coupling. Rose et al. [20] did a comparative analysis between experiments of a liquid nitrogen jet and the six equation model with the addition of a total energy equation. Diot et al. [21] developed a higher-order scheme for compressible multi-material flows based on the concepts of Multidimensional Optimal Order Detection (MOOD). Niu et al. [22] has done some work on compressible liquid-gas flows using the AUSMDV scheme. In recent years, there have been several attempts to model blast waves from BLEVE-type scenarios [23–25].

Kunz et al. [26] presented an algorithm for the computation of viscous two-phase flows, using a model of finite rate phase transition. La Spina et al. [27] also used finite rate phase transitions, with a single temperature two-phase model. Lallemand et al. [28] examined different forms of pressure relaxation procedures for multiphase compressible flows.

Most compressible two-phase solvers use some form of stiffened gas equation of state or a more generalized Mie Gruneisen form equation of state. Even though it can be written on Mie-Gruneisen form, the van der Waals equation of state has been little used in the context of two phase numerical fluid dynamics. Slemrod [29] analyzed the dynamic phase transitions in a van der Waals fluid. Zheng et al. [30] used an interface capturing method with a generalized equation of state on the Mie-Gruneisen form where, among others, the van der Waals equation of state was used. To the authors knowledge, no solvers allowing metastable two-phase compressible flow with phase transition using the van der Waals equation of state exists.

1.3 Contents

The chapters of this thesis are divided as follows.

Chapter 2 provides an overview of Helmholtz free energy type equations of state, as well as detailed descriptions of the stiffened gas equation on state and the van der Waals equation of state. A new spinodal equilibrium mixture equation of state is also described.

Chapter 3 contains an overview of the numerical model that was developed by Saurel et al [16] and the extension to the van der Waals equation of state. An analytical Riemann solver with the extension to equilibrium evaporation waves are also provided.

In Chapter 4, validation cases for both the stiffened gas and the van der Waals equations of state are given. The interface criterion for stiff thermodynamic relaxation is examined in a grid-dependency analysis.

Chapter 5 contains a description of and results from a series of experiments that was conducted as part of the PhD work. The contents of this chapter has been published as an independent article.

In Chapter 6, the experiments in chapter 5 are compared to similar numerical calculations.

Chapter 7 contains concluding remarks, as well as suggestions for further work.

Mathematical and physical constants that were used in the work are listed in Appendix A.

Appendix B contains an overview of important algorithms in the numerical solver. The algorithms are described in pseudo-code.

Publications that were submitted as part of the PhD are provided as an addendum to the thesis.

Chapter 2

Theory

The theory of metastable fluid flow with phase transitions is heavily dependent on thermodynamics. When developing numerical models for such phenomena, the choice of equation of state is crucial. Because of this, the present chapter describes two equations of state in detail, namely the Stiffened Gas Equation of State (SG-EOS) and the van der Waals Equation of State (vdW-EOS). The SG-EOS has been used by several authors in order to develop numerical two-phase solvers, so the section on this is intended as a reference section provided for clarity, since formulations may differ between publications. The section on the vdW-EOS goes more into detail on various thermodynamic properties, in order to derive the necessary formulations to be used in the extension of the numerical two-phase solver. Since some of the formulations are non-standard, derivation steps are included for clarity where needed. A discussion on the existence of a two phase equilibrium state in terms of mixture specific volume and phasic volume fractions are also provided. The last section in this chapter defines a new two-phase mixture equation of state, where both phases are in thermal and mechanical equilibrium and one phase is on the spinodal curve. To the authors knowledge, this type of EOS has not been described before. The new type of mixture EOS is therefore denominated as The Spinodal Equilibrium Mixture Equation of State. It is intended to circumvent the problem of the non-existence of two-phase solutions in the spinodal region in the two-phase numerical solver.

2.1 Helmholtz free energy type equations of state

If the Helmholtz free energy function for a pure substance is known along with its partial derivatives, all other thermodynamic parameters can be determined. For this reason, multi-parameter equations of state like the Span-Wagner EOS are often formulated on the form of the Helmholtz free energy as a function of specific volume and temperature, $f(v, T)$, providing expressions for the partial derivatives. The Span-Wagner EOS is formulated on reduced dimensionless form.

Some of the thermodynamic parameters that can be obtained by the Helmholtz free energy function are given in Table 2.1.

2.2 The stiffened gas equation of state

The stiffened gas equation of state (SG-EOS) is often used when considering liquids under high pressures. It is a variant of the ideal equation of state, with a correction factor p_∞ added to the pressure. A fluid that is governed by the SG-EOS behaves like an ideal gas that is already under the pressure p_∞. That is, for $p_\infty = 0$, the SG-EOS is reduced to the ideal gas EOS. The SG-EOS is defined by the following constant parameters:

p_∞: Pressure correction

c_v: Isochoric heat capacity

γ: Heat capacity ratio

Thermodynamic parameter	Symbol	Helmholtz formulation
Pressure	p	$-\left(\frac{\partial f}{\partial v}\right)_T$
Entropy	s	$-\left(\frac{\partial f}{\partial T}\right)_v$
Internal energy	e	$f - T\left(\frac{\partial f}{\partial T}\right)_v$
Isochoric heat capacity	c_v	$\left(\frac{\partial e}{\partial T}\right)_v$
Enthalpy	h	$e(v,T) + v\ p(v,T)$
Gibbs free energy	g	$h(v,T) - T\ s(v,T)$

Table 2.1: Different thermodynamic parameters given by the Helmholtz free energy function and its partial derivatives.

q: Energy correction

q': Entropy correction

From these, the following constants can be derived:

$$c_p = \gamma c_v \text{ (Isobaric heat capacity)}$$
$$\beta = \frac{1}{\gamma - 1}$$
$$\eta = \gamma p_\infty \beta$$

The stiffened gas EOS can be written on Mie Gruneisen form [16]:

$$\rho e = \beta p + \eta \tag{2.1}$$

The numerical values of the coefficients that were used in numerical calculations can be found in Appendix A.1.

Thermodynamic properties

Pressure:

$$p = (\gamma - 1)c_v T\rho - p_\infty \tag{2.2}$$

Internal energy:

$$e = c_v T + \frac{p_\infty}{\rho} + q \tag{2.3}$$

Entropy:

$$s = c_v \log\left(\frac{T^\gamma}{(p + p_\infty)^{\gamma-1}}\right) + q' \tag{2.4}$$

Speed of sound:

$$c^2 = \gamma\frac{p + p_\infty}{\rho} \tag{2.5}$$

Gibbs free energy:

$$g = T(\gamma c_v - q') + q - Tc_v \log\left(\frac{T^\gamma}{(p + p_\infty)^{\gamma-1}}\right) \tag{2.6}$$

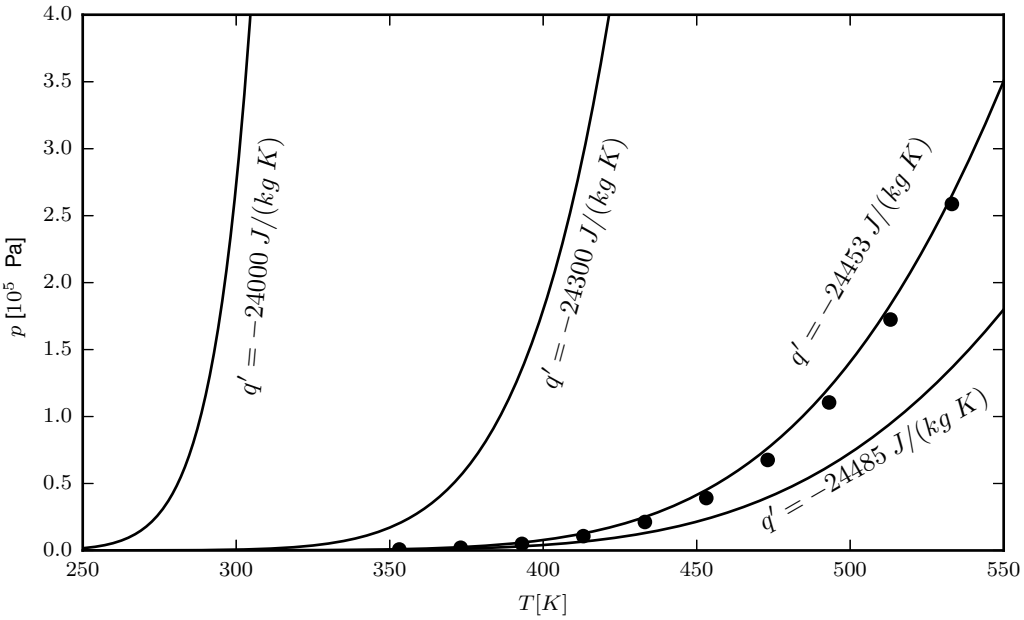

Figure 2.1: Saturation curves of dodecane for different values of q' (vapor) with the SG-EOS. The dotted curve represents experimental saturation data [32]

Entropy correction in reference literature

Le Metayer et al. [31] showed a procedure where the coefficients used in the SG-EOS can be derived from experimental data. However, they fail to specify the required precision of the derived constants to achieve satisfactory agreement with the experimental curves. Specifically, the saturation curve is extremely sensitive to the entropy correction coefficient as is shown in Figure 2.1. For dodecane vapor, Le Metayer et al. specify the value $q'_v = -2.4 \times 10^4$ J/(kg K), which gives a saturation curve that differs severely from the experimental curve. They also give the value $q'_v = -2.4485 \times 10^4$ J/(kg K) in the article text, but this value does not match the experimental saturation curve, nor reproduce the curve that is provided in the article. Saurel et al. [4] and Zein et al. [17] both claim to use $q'_v = -2.4 \times 10^4$ J/(kg K), but given the results of their numerical tests, they clearly use a more accurate value in their calculations. The same inaccuracies are present for q' for water. As the calculations with the SG-EOS are for validation purposes only, values of q' are chosen to yield results that are close to those of [4] and [17].

2.3 The van der Waals equation of state

The van der Waals equation of state (vdW-EOS) is the simplest form of a cubic equation of state. It is classified as cubic because it can be written on the form

$$v^3 + a_2 v^2 + a_1 v + a_0 = 0 \tag{2.7}$$

where v is the specific volume and a_k are pressure and/or temperature dependent coefficients. The vdW-EOS can be derived from the ideal gas EOS by adding correction terms for the excluded volume occupied by finite-sized particles and inter-molecular forces. On its classical form, the vdW-EOS reads

$$\left(p + \frac{n^2 a}{V}\right)(V - nb) = nR_M T \tag{2.8}$$

where n is the number of moles occupying the volume V at pressure p and temperature T. R_M is the ideal gas constant. a is a measure of the attraction between particles and b is the volume excluded by one

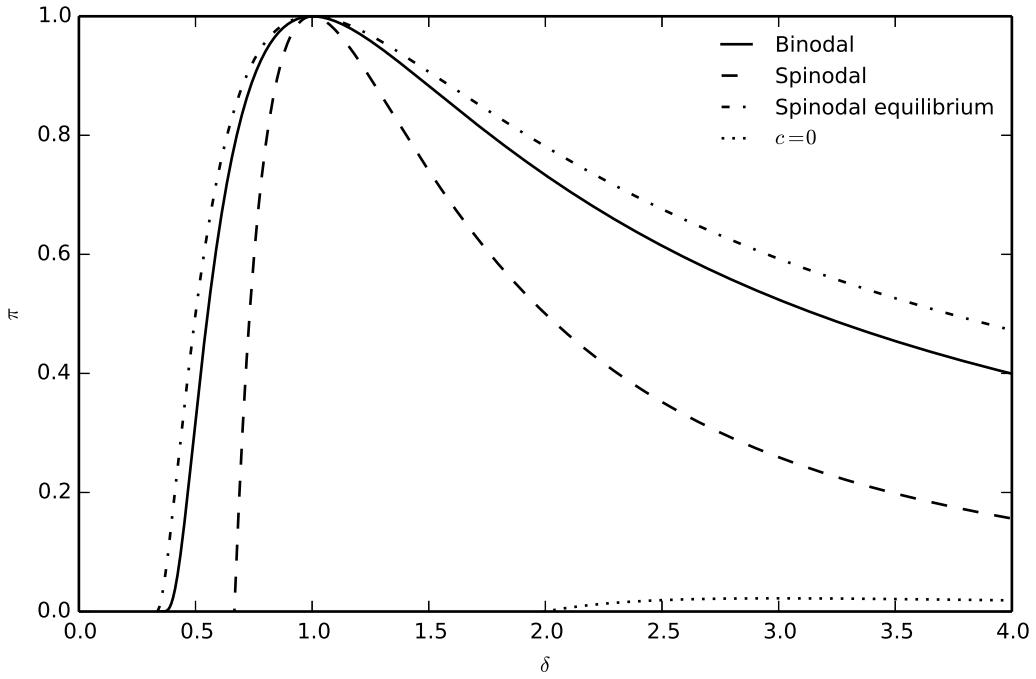

Figure 2.2: The binodal, spinodal and spinodal equilibrium curves of a van der Waals fluid in $\pi - \delta$ (reduced pressure and volume) space. The loci of zero speed of sound are also shown.

mole of particles (molecules). As the volume tends to infinity, the vdW-EOS converges to the ideal gas law. The special case of $V = nb$ corresponds to a situation where the volume V is completely filled by the particles. At this point, the pressure tends to infinity. This implies that the van der Waals equation of state is only valid for $V > nb$. In terms of the volume at the critical point, this limit can be written as $\frac{v}{v_c} > \frac{1}{3}$. By using the definition of the critical point $\left(\frac{\partial p(V,T)}{\partial V} = \frac{\partial^2 p(V,T)}{\partial V^2} = 0\right)$, one can show that

$$p_c = \frac{a}{27b^2} \tag{2.9}$$

and

$$T_c = \frac{8a}{27bR_M}. \tag{2.10}$$

Figure 2.2 shows the binodal, spinodal and spinodal equilibrium curves of a van der Waals fluid.

2.3.1 Helmholtz free energy formulation

The specific Helmholtz free energy of a van der Waals fluid is defined by [33]

$$f = -Nk_BT\left[\log\left(\frac{V - bN}{N}\right) + \frac{3}{2}\log(k_BT) + X\right] - a\left(\frac{N^2}{V}\right), \tag{2.11}$$

where log is the natural logarithm and X is a gas specific constant. This can be re-written on reduced form as

$$\phi = \frac{f}{RT_c} = -\tau\left[1 + \log\frac{(\delta - \frac{1}{3})\tau^{3/2}}{c'}\right] - \frac{9}{8\delta}, \tag{2.12}$$

where R is the specific gas constant (R_M/M),

$$\tau = \frac{T}{T_c}, \tag{2.13}$$

$$\delta = \frac{v}{v_c} \tag{2.14}$$

and c' is a (gas-specific) dimensionless constant. Changing it will add a term proportional to τ to the specific free energy. Since the pressure, internal energy, speed of sound and Gibbs free energy difference $(g_v - g_l)$ at equal temperature is invariant of c', its value does not influence the numerical calculations in the present work. Hence, we use $c' = 1$ for all calculations. Note that the critical specific volume v_c of a van der Waals fluid is defined by

$$v_c \equiv \frac{3RT_c}{8p_c} \tag{2.15}$$

and will differ from the specific volume of a given physical fluid at the critical point.

Derivatives of the reduced Helmholtz free energy

$$\phi_\delta = \left(\frac{\partial\phi(\tau,\delta)}{\partial\delta}\right)_\tau = \frac{3\tau}{1-3\delta} + \frac{9}{8\delta^2} \tag{2.16}$$

$$\phi_{\delta\delta} = \left(\frac{\partial^2\phi(\tau,\delta)}{\partial\delta^2}\right)_\tau = \frac{\tau}{(\delta-\frac{1}{3})^2} - \frac{9}{4\delta^3} \tag{2.17}$$

$$\phi_\tau = \left(\frac{\partial\phi(\tau,\delta)}{\partial\tau}\right)_\delta = -\log\frac{(\delta-\frac{1}{3})\tau^{3/2}}{c'} - \frac{5}{2} \tag{2.18}$$

$$\phi_{\tau\tau} = \left(\frac{\partial^2\phi(\tau,\delta)}{\partial\tau^2}\right)_\delta = -\frac{3}{2\tau} \tag{2.19}$$

$$\phi_{\tau\delta} = \left(\frac{\partial^2\phi(\tau,\delta)}{\partial\tau\partial\delta}\right) = \frac{3}{1-3\delta} \tag{2.20}$$

Derivatives of the specific Helmholtz free energy

$$\left(\frac{\partial f(T,v)}{\partial v}\right)_T = \frac{RT_c}{v_c}\phi_\delta \tag{2.21}$$

$$\left(\frac{\partial^2 f(T,v)}{\partial v^2}\right)_T = \frac{RT_c}{v_c^2}\phi_{\delta\delta} \tag{2.22}$$

$$\left(\frac{\partial f(T,v)}{\partial T}\right)_v = \frac{RT_c}{T_c}\phi_\tau = R\phi_\tau \tag{2.23}$$

$$\left(\frac{\partial^2 f(T,v)}{\partial T^2}\right)_v = \frac{R}{T_c}\phi_{\tau\tau} \tag{2.24}$$

$$\left(\frac{\partial^2 f(T,v)}{\partial T\partial v}\right) = \frac{RT_c}{v_cT_c}\phi_{\tau\delta} = \frac{R}{v_c}\phi_{\tau\delta} \tag{2.25}$$

Thermodynamic properties

Pressure:

$$p(v,T) = -\left(\frac{\partial f}{\partial v}\right)_T = -\frac{RT_c}{v_c}\phi_\delta \tag{2.26}$$

Entropy:

$$s(v,T) = -\left(\frac{\partial f}{\partial T}\right)_v = -R\phi_\tau \tag{2.27}$$

The isentrop of the van der Waals EOS is given by

$$(\delta - \frac{1}{3})\tau^{3/2} = \text{const.} \tag{2.28}$$

Internal Energy:

$$e(v,T) = f - T\left(\frac{\partial f}{\partial T}\right)_v = RT_c(\phi - \tau\phi_\tau) \tag{2.29}$$

$$= RT_c\left(-\tau\left[1 + \log\frac{(\delta - \frac{1}{3})\tau^{3/2}}{c'}\right] - \frac{9}{8\delta} - \tau\left[-\log\frac{(\delta - \frac{1}{3})\tau^{3/2}}{c'} - \frac{5}{2}\right]\right) \tag{2.30}$$

$$= RT_c\left(-\frac{9}{8\delta} + \tau\frac{3}{2}\right) \tag{2.31}$$

Isochoric heat capacity:

$$c_v(v,T) = \left(\frac{\partial e}{\partial T}\right)_v = \left(\frac{\partial f}{\partial T}\right)_v - \left[\left(\frac{\partial f}{\partial T}\right)_v + T\left(\frac{\partial^2 f}{\partial T^2}\right)\right] = -\tau R\phi_{\tau\tau} = \frac{3}{2}R \tag{2.32}$$

Enthalpy:

$$h(v,T) = e(v,T) + v\ p(v,T) = RT_c(\phi - \tau\phi_\tau - \delta\phi_\delta) \tag{2.33}$$

Gibbs free energy:

$$g(v,T) = h(v,T) - T\ s(v,T) = RT_c(\phi - \delta\phi_\delta) \tag{2.34}$$

Reduced thermodynamic properties

Reduced pressure:

$$\pi(\delta,\tau) \equiv -\frac{8}{3}\phi_\delta = \frac{8\tau}{3\delta - 1} - \frac{3}{\delta^2} \tag{2.35}$$

Note that the scaling factor of $8/3$ is introduced to ensure $\pi(1,1) = 1$. This can be rearranged to obtain a formulation for the reduced temperature:

$$\tau(\delta,\pi) = \frac{(3\delta - 1)(\delta^2\pi + 3)}{8\delta^2} \tag{2.36}$$

Reduced internal energy:

$$\epsilon(\delta,\tau) \equiv \frac{e(v,T)}{e(v_c,T_c)} = 4\tau - \frac{3}{\delta} \tag{2.37}$$

Reduced Gibbs free energy:

$$\gamma(\delta,\tau) \equiv \frac{g(v,T)}{RT_c} = \phi - \delta\phi_\delta \tag{2.38}$$

Note that the reduced Gibbs free energy at the critical point is not equal to one ($\gamma(1,1) \neq 1$).

2.3.2 Mie Gruneisen formulation

The van der Waals EOS can be written on Mie Gruneisen form [34]:

$$e = c_v T + a(v), \tag{2.39}$$

$$p = \frac{\Gamma c_v T}{v} - a'(v) \tag{2.40}$$

where

$$a(v) = -\frac{9v_cT_cR}{8v}, a'(v) = \frac{9v_cT_cR}{8v^2} \tag{2.41}$$

and

$$\Gamma \equiv v\left(\frac{\partial p}{\partial e}\right)_v = \frac{2v}{3v - v_c}. \tag{2.42}$$

2.3.3 Two phase thermal and mechanical equilibrium state

For a two phase state with reduced volumes δ_1 and δ_2 in thermal and mechanical equilibrium ($\tau_1 = \tau_2$ and $\pi_1 = \pi_2$), the following relations can be derived from Equation 2.35:

$$\tau = \frac{(3\delta_1 - 1)(3\delta_2 - 1)(\delta_1 + \delta_2)}{8\delta_1^2\delta_2^2} \tag{2.43}$$

$$\pi = \frac{3\delta_1\delta_2 - \delta_1 - \delta_2}{\delta_1^2\delta_2^2} \tag{2.44}$$

2.3.4 Mixture EOS

The mixture equation of state for a two phase mixture in thermal and mechanical equilibrium can be written as

$$\pi = \left(\frac{\epsilon}{\delta} - \frac{3\alpha(\delta_1 - 1)}{2\delta_1^3} - \frac{3(1-\alpha)(\delta_2 - 1)}{2\delta_2^3}\right)\left(\frac{\alpha}{2\delta_1}(3\delta_1 - 1) + \frac{1-\alpha}{2\delta_2}(3\delta_2 - 1)\right)^{-1} \tag{2.45}$$

2.3.5 Volume roots

Equation 2.35 has three specific volume roots. In the co-existence region, all three roots are real. To find the roots, we can write the pressure equation on cubic form:

$$\delta^3 + a_2\delta^2 + a_1\delta + a_0 = 0 \tag{2.46}$$

where

$$a_2 = -\frac{8\tau}{3\pi} - \frac{1}{3},\ a_1 = \frac{3}{\pi},\ a0 = -\frac{1}{\pi} \tag{2.47}$$

The roots can be found by defining [35]

$$D = Q^3 + R^2,\ Q = \frac{3a_1 - a_2^2}{9},\ R = \frac{9a_1a_2 - 27a_0 - 2a_2^3}{54}. \tag{2.48}$$

In this context, R is a variable and should not be confused with the specific gas constant. The solutions can be divided into three regions:

$D > 0$: one real root (single phase solution)
$D = 0$: three real roots, at least two equal (spinodal/critical solution)
$D < 0$: three real unequal roots (co − existence solution)

For $D \leq 0$, the three roots are

$$\delta_k = 2\sqrt{-Q}\cos\left(\frac{\theta + 2k\ \pi_M}{3}\right) - \frac{a_2}{3} \text{ for } k \in (0, 1, 2) \tag{2.49}$$

where

$$\theta = \arccos\left(\frac{R}{\sqrt{-Q^3}}\right)$$

and π_M is the mathematical constant π. When all three roots are real, the liquid root can be determined as $\delta_l = \min(\delta_0, \delta_1, \delta_2)$ and the vapor root by $\delta_v = \max(\delta_0, \delta_1, \delta_2)$

2.3.6 Speed of sound

The speed of sound is defined as

$$c^2 = \left(\frac{\partial p}{\partial \rho}\right)_s \tag{2.50}$$

To find an expression of the speed of sound as a function of volume and temperature, we first define the reduced temperature as a function of reduced specific volume and specific entropy:

$$\tau = \left(\frac{3c' \exp(\frac{s}{R} - \frac{5}{2})}{3\delta - 1} \right)^{2/3} \tag{2.51}$$

This expression is inserted into the pressure equation (2.35), to find:

$$p(\delta, s) = p_c \left(8 \frac{\left(3c' \exp(\frac{s}{R} - \frac{5}{2})\right)^{2/3}}{(3\delta - 1)^{5/3}} - \frac{3}{\delta^2} \right) \tag{2.52}$$

We can now find the density derivative of the pressure ($\delta = \frac{1}{\rho v_c}$)

$$\left(\frac{\partial p}{\partial \rho} \right)_s = p_c v_c \left(40 \ \frac{\delta^2 \left(3c' \exp(\frac{s}{R} - \frac{5}{2})\right)^{2/3}}{(3\delta - 1)^{8/3}} - \frac{6}{\delta} \right) = p_c v_c \left(\frac{40\tau\delta^2}{(1 - 3\delta)^2} - \frac{6}{\delta} \right) \tag{2.53}$$

so that

$$c = \left[p_c v_c \left(\frac{40\tau\delta^2}{(1 - 3\delta)^2} - \frac{6}{\delta} \right) \right]^{\frac{1}{2}}. \tag{2.54}$$

Since the speed of sound must be real and positive maintain hyperbolicity in the numerical model, an expression for the speed of sound equal to zero is derived:

$$\tau_{\mathrm{c=0}} = \frac{3(3\delta - 1)^2}{20\delta^3} \tag{2.55}$$

or

$$\pi_{\mathrm{c=0}} = \frac{3(\delta - 2)}{5\delta^3} \tag{2.56}$$

2.3.7 The binodal curve

The binodal curve is defined as the loci of $\gamma_1 = \gamma_2$, $\pi_1 = \pi_2$ and $\tau_1 = \tau_2$, where $\delta_1 \neq \delta_2$. Since $\pi_1 = \pi_2$, we know that $\phi_\delta(\delta_1, \tau) = \phi_\delta(\delta_2, \tau)$, so that

$$\gamma_1 - \gamma_2 = \phi(\tau, \delta_1) - \phi(\tau, \delta_2) - \phi_\delta(\delta_1, \tau)\left[\delta_1 - \delta_2\right] = 0 \tag{2.57}$$

or

$$\log\left(\frac{3\delta_1 - 1}{3\delta_2 - 1}\right) - \frac{9}{8\tau}\left(\frac{(\delta_1 - \delta_2)^2}{\delta_1^2 \delta_2}\right) + (\delta_1 - \delta_2)\frac{3}{1 - 3\delta_1} = 0. \tag{2.58}$$

We insert the thermal and mechanical equilibrium temperature (2.43) into the above expression to find:

$$\Delta_g(\delta_1, \delta_2) \equiv \log\left(\frac{3\delta_1 - 1}{3\delta_2 - 1}\right) - 9\frac{\delta_2(\delta_1 - \delta_2)^2}{(3\delta_1 - 1)(3\delta_2 - 1)(\delta_1 + \delta_2)} + (\delta_1 - \delta_2)\frac{3}{1 - 3\delta_1} = 0 \tag{2.59}$$

which can be used in an iterative solver to find the thermodynamic equilibrium state when one reduced volume is known. For this purpose, the partial derivatives of Δ_g are listed:

$$\frac{\partial}{\partial \delta_1}\Delta_g(\delta_1, \delta_2) = \frac{9(\delta_1 - \delta_2)^2\left(\delta_1(3\delta_2 - 1) - 2\delta_2\right)}{(1 - 3\delta_1)^2(3\delta_2 - 1)(\delta_1 + \delta_2)^2} \tag{2.60}$$

$$\frac{\partial}{\partial \delta_2}\Delta_g(\delta_1, \delta_2) = -\frac{9(\delta_1 - \delta_2)^2\left(\delta_1(3\delta_2 - 2) - \delta_2\right)}{(1 - 3\delta_2)^2(3\delta_1 - 1)(\delta_1 + \delta_2)^2} \tag{2.61}$$

The equilibrium isentrop

The equilibrium isentrop can be defined as the as the thermodynamic path of a two phase mixture where the liquid and vapor phase stays in thermodynamic equilibrium with constant mixture entropy. The constant mixture entropy is satisfied by

$$C_{s,\mathrm{sat}} \equiv (3\delta_1 - 1)^{Y + \frac{3}{2}}(3\delta_2 - 1)^{\frac{5}{2} - Y}\left(\frac{\delta_1 + \delta_2}{8}\right)^{\frac{3}{2}}\frac{1}{(\delta_1\delta_2)^3} = \mathrm{const.} \tag{2.62}$$

This expression can be used to derive a mixture speed of sound of a two phase system with infinitely fast thermodynamic relaxation.

2.3.8 The spinodal curve

The spinodal curve is defined by the loci of

$$\left(\frac{\partial \pi}{\partial \delta}\right)_\tau = 0 \tag{2.63}$$

or

$$\frac{\partial}{\partial \delta}\left(\frac{8\tau}{3\delta - 1} - \frac{3}{\delta^2}\right) = 6\left(\frac{1}{\delta^3} - \frac{4\tau}{(1-3\delta)^2}\right) = 0 \tag{2.64}$$

We solve this expression to find the spinodal temperature

$$\tau_s(\delta) = \frac{(1-3\delta)^2}{4\delta^3}, \tag{2.65}$$

the spinodal pressure

$$\pi_s(\delta) = \frac{3\delta - 2}{\delta^3} \tag{2.66}$$

and the internal energy on the spinodal curve

$$\epsilon_s(\delta) = \frac{6\delta^2 - 6\delta + 1}{\delta^3}. \tag{2.67}$$

Spinodal equilibrium state

If we insert the expressions for the spinodal pressure and temperature into the pressure equation (2.35), we get

$$\frac{3\delta_1 - 2}{\delta_1^3} = \frac{2(1-3\delta_1)^2}{(3\delta_2 - 1)\delta_1^3} - \frac{3}{\delta_2^2} \tag{2.68}$$

or

$$\delta_2 = \frac{\delta_1}{3\delta_1 - 2} \tag{2.69}$$

where δ_2 is the specific volume of the other phase in thermal and mechanical equilibrium with the phase at the spinodal. This state is denoted the spinodal equilibrium state and is plotted in Figure 2.2. It is used in the spinodal phase transition algorithm to find the state where one phase is on the spinodal and the other is in thermal and mechanical equilibrium with the spinodal state.

Speed of sound at the spinodal state

The spinodal pressure (2.66) is greater than the pressure at zero speed of sound (2.56) when

$$\frac{3\delta - 2}{\delta^3} > \frac{3(\delta - 2)}{5\delta^3} \tag{2.70}$$

or

$$\delta > \frac{1}{3}. \tag{2.71}$$

Thus, the speed of sound is real and positive for all physical states given by the van der Waals EOS, including the spinodal states.

2.3.9 The Hugoniot curve

We recall the Hugoniot criterion:

$$e_n - e_0 + \frac{p_n + p_0}{2}(v_n - v_0) = 0 \tag{2.72}$$

Since $p_c v_c / e_c = 1$, this can be formulated on reduced form

$$\epsilon_n - \epsilon_0 + \frac{\pi_n + \pi_0}{2}(\delta_n - \delta_0) = 0 \tag{2.73}$$

For a single phase, this can be reformulated to

$$\left(4\tau_n - \frac{3}{\delta_n} - 4\tau_0 + \frac{3}{\delta_0}\right) + \frac{\pi_n + \pi_0}{2}(\delta_n - \delta_0) = 0$$

$$\frac{1}{2}\left((\pi_n + \frac{3}{\delta_n^2})(3\delta_n - 1) - (\pi_0 + \frac{3}{\delta_0^2})(3\delta_0 - 1)\right) - \frac{3}{\delta_n} + \frac{3}{\delta_0} + \frac{(\pi_n + \pi_0)}{2}(\delta_n - \delta_0) = 0$$

$$\pi_n\left[(3\delta_n - 1) + (\delta_n - \delta_0)\right] + \frac{3}{\delta_n^2}(3\delta_n - 1) - (\pi_0 + \frac{3}{\delta_0^2})(3\delta_0 - 1) - \frac{6}{\delta_n} + \frac{6}{\delta_0} + \pi_0(\delta_n - \delta_0) = 0$$

$$\pi_n = -\left[\frac{3}{\delta_n^2}(3\delta_n - 1) - (\pi_0 + \frac{3}{\delta_0^2})(3\delta_0 - 1) - \frac{6}{\delta_n} + \frac{6}{\delta_0} + \pi_0(\delta_n - \delta_0)\right]\frac{1}{(3\delta_n - 1) + (\delta_n - \delta_0)} \tag{2.74}$$

2.3.10 Limits of existence for a two phase state in thermal and mechanical equilibrium

In order to be able to determine the physical state in a computational cell defined by reduced mixture volume δ and mixture internal energy ϵ, we will derive limits for equilibrium states (both thermal and thermodynamic). These limits are defined by upper energy limits, above which an equilibrium solution does not exist. The energy limits are functions of the reduced mixture volume δ.

For any $\delta = Y\delta_v + (1-Y)\delta_l$, where subscripts v and l denotes vapor and liquid phases, there are well defined boundaries to the existence of a two phase state in thermal and mechanical equilibrium. Both the liquid and the vapor root can be distinguished from the intermediate root by enforcing the criterion

$$\left(\frac{\partial\pi(\delta_k, \tau)}{\partial\delta_k}\right)_\tau < 0 \tag{2.75}$$

where δ_k is either the liquid or the vapor reduced volume. A trivial limit of the existence of such state is the critical pressure and temperature ($\pi < 1,\ \tau < 1$). Also, the van der Waals EOS is only valid for $\delta > 1/3$, so that $\delta_l > 1/3$. By using the expression for the equal pressure temperature (2.43), the spinodal temperature (2.65) and the spinodal equilibrium reduced volume (2.69) in combination with the volume fraction saturation criterion

$$\frac{1}{\delta} = \frac{\alpha}{\delta_v} + \frac{1-\alpha}{\delta_l}, \tag{2.76}$$

we get two limits for the temperature, namely the vapor spinodal (denoted by superscript vs)

$$\tau = \tau_s(\delta_v)\begin{cases}\delta_v^{vs} = \frac{(3\alpha-2)\delta}{3(\alpha-1)\delta+1} \\ \delta_l^{vs} = \frac{(3\alpha-2)\delta}{3\alpha\delta-2}\end{cases} \tag{2.77}$$

and the liquid spinodal (denoted by superscript ls)

$$\tau = \tau_s(\delta_l)\begin{cases}\delta_v^{ls} = \frac{(3\alpha-1)\delta}{3(\alpha-1)\delta+2} \\ \delta_l^{ls} = \frac{(1-3\alpha)\delta}{1-3\alpha\delta}\end{cases} \tag{2.78}$$

The possible states are dependent on the mixture reduced volume δ:

$$\frac{1}{3} < \delta < \frac{2}{3} \qquad \begin{cases} \alpha < 1 - \frac{1}{3\delta} : & \begin{cases} \delta_v^{vs} < \delta_v \\ 1/3 < \delta_l < \delta_l^{vs} \end{cases} \end{cases} \tag{2.79}$$

$$\frac{2}{3} < \delta < 1 \quad \begin{cases} \alpha < 1 - \frac{2}{3\delta} : & \begin{cases} \delta_v^{vs} < \delta_v < \delta_v^{ls} \\ \delta_l^{ls} < \delta_l < \delta_l^{vs} \end{cases} \\ 1 - \frac{2}{3\delta} \leq \alpha < 1 - \frac{1}{3\delta} : & \begin{cases} \delta_v^{vs} < \delta_v \\ 1/3 < \delta_l < \delta_l^{vs} \end{cases} \end{cases} \tag{2.80}$$

$$\delta = 1 \qquad \begin{cases} \frac{1}{3} < \alpha < \frac{2}{3} : & \begin{cases} 1 < \delta_v \\ 1/3 < \delta_l < 1 \end{cases} \end{cases} \tag{2.81}$$

$$1 < \delta \quad \begin{cases} 1 - \frac{2}{3\delta} < \alpha \leq 1 - \frac{1}{3\delta} : & \begin{cases} \delta_v^{ls} < \delta_v \\ 1/3 < \delta_l < \delta_l^{ls} \end{cases} \\ 1 - \frac{1}{3\delta} < \alpha : & \begin{cases} \delta_v^{ls} < \delta_v < \delta_v^{vs} \\ \delta_l^{vs} < \delta_l < \delta_l^{ls} \end{cases} \end{cases} \tag{2.82}$$

Note that the first case ($1/3 < \delta < 2/3$) is just a special case of $\delta < 1$ where the liquid spinodal is not reachable. The possible states are shown for $\delta < 1$ in fig. 2.3 and for $\delta > 1$ in fig. 2.4.

Internal energy

The mixture energy of a two phase state with equal pressure and temperature is given as

$$\epsilon = 4\tau + 3Y\left(\frac{1}{\delta_l} - \frac{1}{\delta_v}\right) - \frac{3}{\delta_l} \tag{2.83}$$

For any state in the two phase region defined by δ, α and δ_v, if δ_v is increased by a small value while holding δ and α constant will result in a small decrease in the vapor mass fraction ($Y = \frac{\delta\alpha}{\delta_v}$). This is the equivalent of a small amount of vapor condensing into liquid, and will release a portion of the internal energy of the system to the surroundings. Hence, we will assume that the internal energy of a system defined by δ and α is monotonically decreasing with increasing δ_v (and decreasing δ_l),

$$\left(\frac{\partial \epsilon}{\partial \delta_v}\right)_{\delta,\alpha} \leq 0, \left(\frac{\partial \epsilon}{\partial \delta_l}\right)_{\delta,\alpha} \geq 0. \tag{2.84}$$

We will also make the following assumptions about the vapor volume partial derivative of the mixture internal energy with constant mixture volume on the spinodal (superscript vs and ls) and saturation (superscript $*$) curves:

$$\delta < 1,\ \alpha < 1 - \frac{1}{3\delta} \begin{cases} \left(\frac{\partial}{\partial \delta_v}\epsilon(\delta_v^{vs}, \delta_l^{vs})\right)_\delta < 0 \\ \left(\frac{\partial}{\partial \delta_v}\epsilon(\delta_v^{*}, \delta_l^{*})\right)_\delta < 0 \end{cases} \tag{2.85}$$

$$\delta > 1,\ \alpha > 1 - \frac{2}{3\delta} \begin{cases} \left(\frac{\partial}{\partial \delta_v}\epsilon(\delta_v^{*}, \delta_l^{*})\right)_\delta < 0 \\ \left(\frac{\partial}{\partial \delta_v}\epsilon(\delta_v^{ls}, \delta_l^{ls})\right)_\delta < 0 \end{cases} \tag{2.86}$$

These assumptions can be justified by the following argument: Since the mixture pressure is monotonically decreasing with increasing vapor specific volume along the spinodal, binodal and spinodal-equilibrium curves, an increase in vapor specific volume is equivalent to a decrease in mixture pressure. If the mixture specific volume is constant, a decrease in mixture pressure is equivalent to a decrease in mixture internal energy.

The above assumptions then give rise to an important conclusion: For any δ, there is a maximum value for the mixture internal energy determining the existence of a two phase solution in thermal and

mechanical equilibrium, and a maximum value for the existence of a two phase solution in thermodynamic equilibrium. These values are taken in the pure phase limit as follows:

$$\epsilon_{\max,\text{thermal}} = \begin{cases} \lim_{\alpha\to 0}\ \epsilon(\delta_v^{vs}, \delta_l^{vs}) \text{ for } \delta < 1 \\ \lim_{\alpha\to 1}\ \epsilon(\delta_v^{ls}, \delta_l^{ls}) \text{ for } \delta > 1 \end{cases} \tag{2.87}$$

$$\epsilon_{\max,\text{thermodynamic}} = \begin{cases} \lim_{\alpha\to 0}\ \epsilon(\delta_v^{*}, \delta_l^{*}) \text{ for } \delta < 1 \\ \lim_{\alpha\to 1}\ \epsilon(\delta_v^{*}, \delta_l^{*}) \text{ for } \delta > 1 \end{cases} \tag{2.88}$$

For $\delta = 1$, we have $\epsilon_{\max,\text{thermal}} = \epsilon_{\max,\text{thermodynamic}} = 1$.

The two energy limits are used in the numerical code to determine whether to look for a solution in thermodynamic equilibrium, thermal equilibrium or mechanical equilibrium. In the numerical code, the vapor volume fraction is confined to the interval $\langle \xi, 1-\xi \rangle$, so that ϵ_{max} is taken at $\alpha = \xi$ for $\delta < 1$ and $\alpha = 1 - \xi$ for $\delta > 1$.

2.4 The spinodal equilibrium mixture equation of state

A problem with using a non-monotonic equation of state when dealing with two phase flow is that a liquid and vapor solution to $p(v, T)$ does not exist for all (v, T). As is shown in Figure 2.5, for any $T < T_c$, the spinodal points denote a lower limit in pressure for the liquid solution and an upper limit for the vapor solution. Beyond these limits, the EOS has only one (single phase) solution. One can also look at the spinodal points as limits for internal energy. For any specific volume v, there is a corresponding internal energy e_s so that $p(v, e_s)$ lies on the spinodal curve (Equation 2.67 for the vdW-EOS). If the internal energy is below this limit, a single phase solution does not exist. In the numerical method used presently, the internal energy of a phase is changed by convection and relaxation processes. There is no guarantee that these energy limits will not be violated. We propose a solution to this problem, namely the spinodal equilibrium mixture equation of state (SEM-EOS). This is a numerical method that restores the existence of the liquid/vapor in the sub-spinodal region by enforcing numerical evaporation/condensation in the sub-spinodal fluid. Since we deal mainly in superheated liquids, we will discuss the method from the liquid point of view, but the methodology is analogous for sub-cooled vapors. The method is not meant to be physically accurate, but is only intended to solve the numerical problem of fluid flow in the presence of absolute limits of metastability while maintaining conservation of energy and mass. In a real metastable liquid, homogeneous nucleation at the kinetic limit of superheat will prevent the liquid from reaching the spinodal state. From a numerical viewpoint, however, there is still a need to adress the spinodal issue, so that an evaporation rate model can be treated independently of the fluid flow. It should be noted that the method can use an arbitrary curve as the metastability limit, as long as a single phase solution exists for all $e(v, T) \geq e_s(v)$. This implies that an approximation of $p_s(v)$ can be used if it is impractical/impossible to find the analytical curve (Span-Wagner EOS) or if the spinodal curve does not exist (SG-EOS).

When discussing a liquid spinodal equilibrium mixture, we denote the spinodal liquid as the true liquid and the vapor as numerical vapor. This is done to separate the vapor that is part of the SEM-EOS from the vapor that is part of a regular two-phase flow.

The spinodal curve in p-v space can be formulated on the form of $p_s(v)$. As discussed above, this translates to an internal energy $e_s = e(v, p_s(v))$. The spinodal equilibrium mixture EOS is used in the case of $e < e_s$. To ensure that the true liquid phase is in the permitted region, we will evaporate part of it, so that the pressure lies on the spinodal curve. The generated vapor will be assumed to be in mechanical and thermal equilibrium with the liquid phase, illustrated by the spinodal-equilibrium points in Figure 2.5. The system will be closed by a mixture equation of state. We now review the plot of the van der Waals EOS in $\pi - \delta$ space in Figure 2.2. The spinodal equilibrium curve is plotted here, showing the state of the vapor/liquid that is in thermal and mechanical equilibrium with the liquid/vapor at the spinodal curve. One way to think about the relation between the spinodal and spinodal equilibrium curves is that they form two "saturation envelopes". One is the liquid spinodal ($\delta < 1$) paired with the vapor equilibrium curve ($\delta > 1$) and the other is the opposite. The analogy to the saturation (binodal) curve is that any liquid state that is heated at constant pressure beyond the spinodal temperature at that pressure will evaporate partly, so that the two states lies on the liquid spinodal-vapor equilibrium

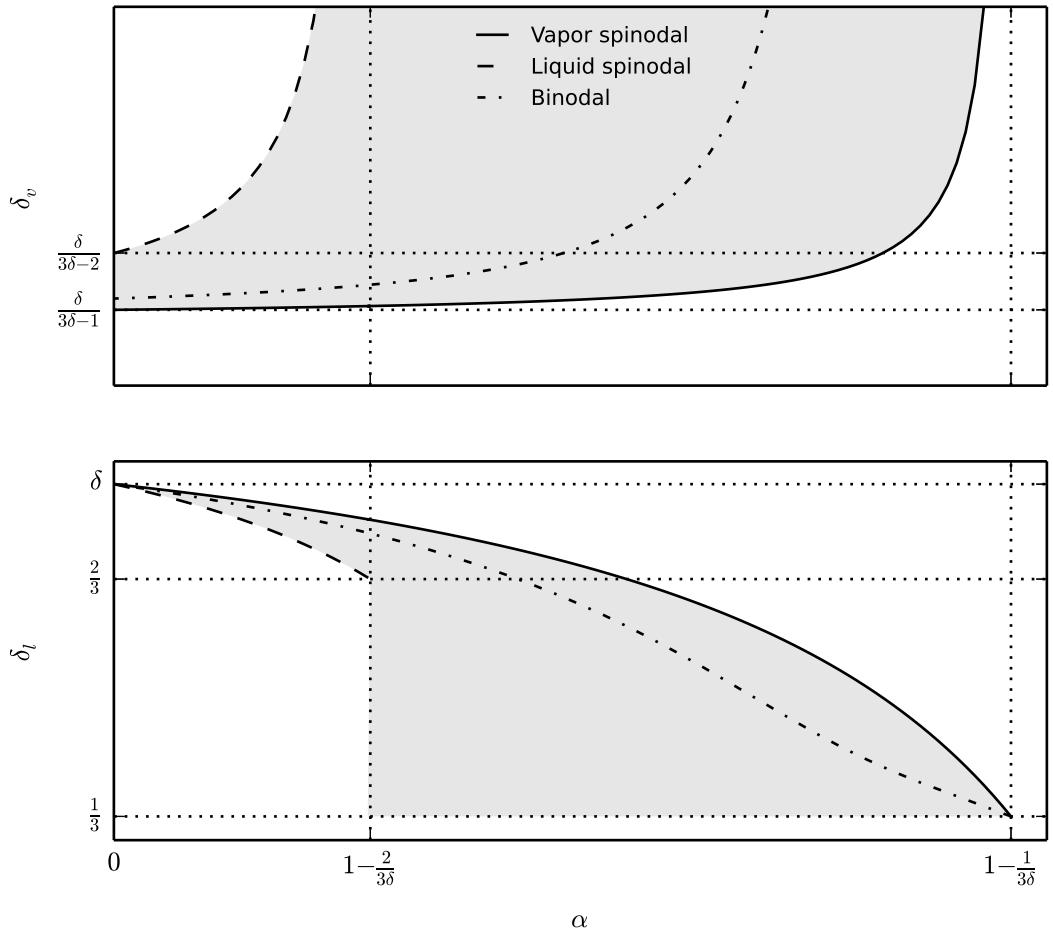

Figure 2.3: $\delta < 1$: Graphical view of the region in α-δ_k space where a two phase solution in thermal and mechanical equilibrium can exist (gray region). The region is bounded by the vapor spinodal (solid line) and the liquid spinodal (dashed line). The binodal curve (dash-dotted line) is also shown. Note that for the special case of $\delta < \frac{2}{3}$, the limit $\alpha = 1 - \frac{2}{3\delta}$ becomes negative, so that only the vapor spinodal is present.

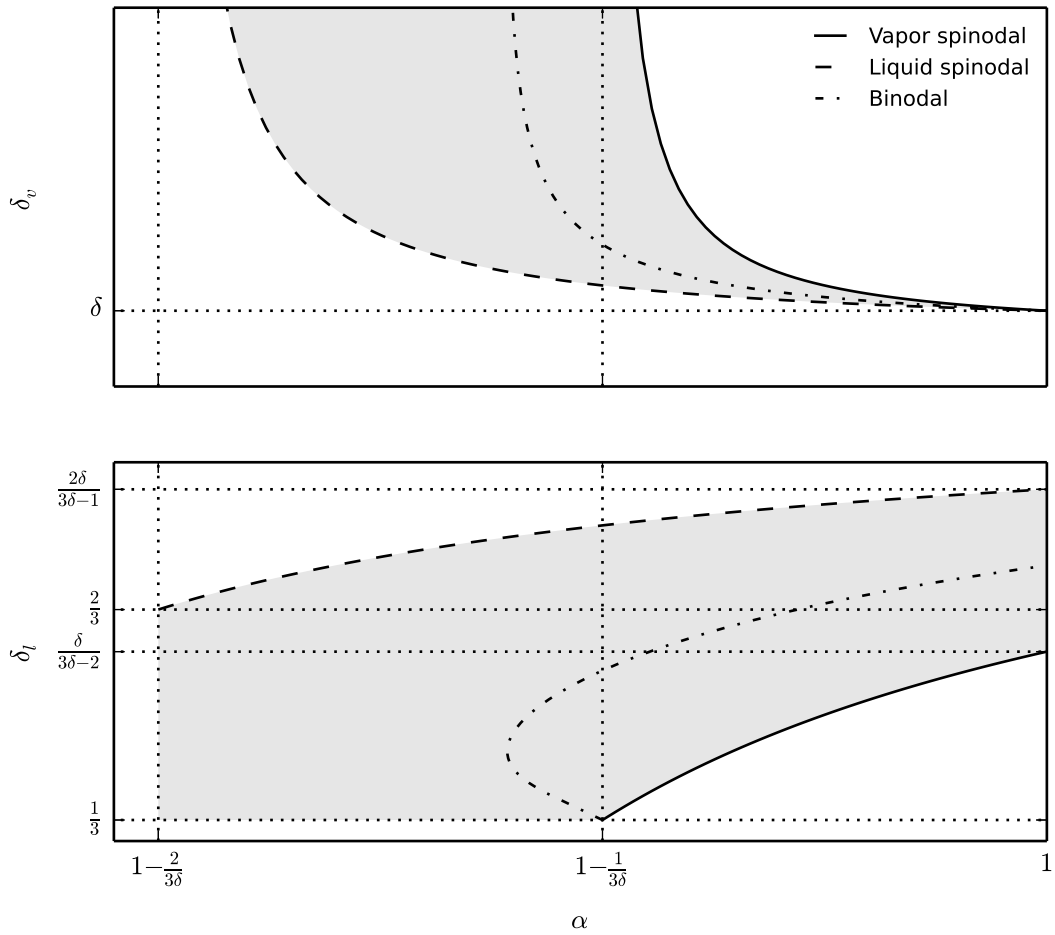

Figure 2.4: $\delta > 1$: Graphical view of the region in α-δ_k space where a two phase solution in thermal and mechanical equilibrium can exist (gray region). The region is bounded by the vapor spinodal (solid line) and the liquid spinodal (dashed line). The binodal curve (dash-dotted line) is also shown.

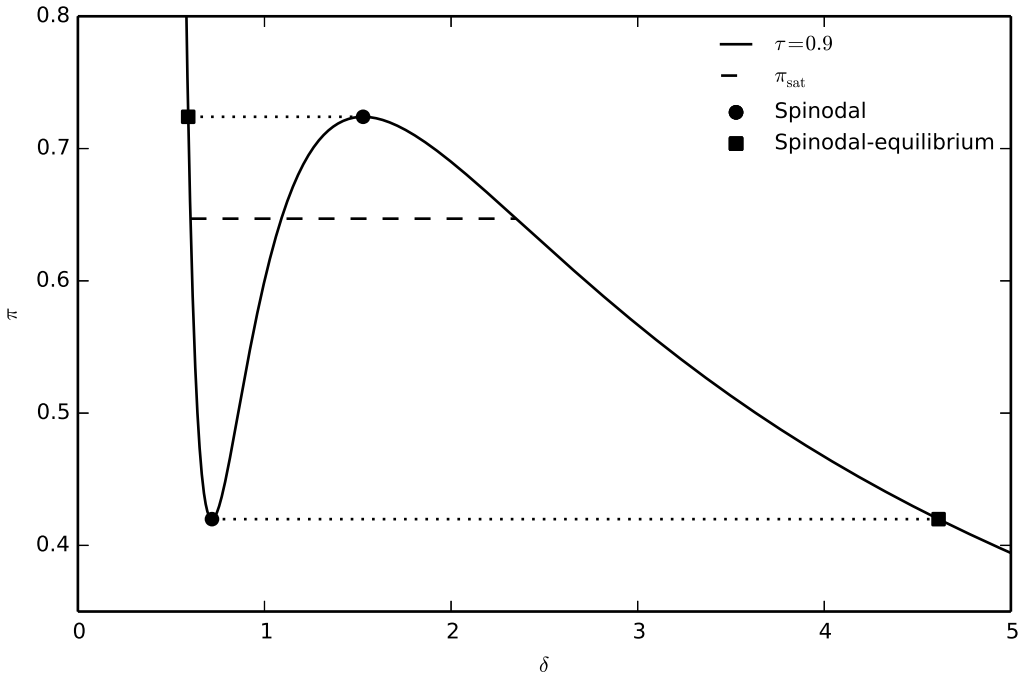

Figure 2.5: Isoterm for $\tau = 0.9$ with the van der Waals EOS

curve, while the temperature remains constant at the equivalent of a boiling point. If enough heat is added, the liquid may evaporate completely and the vapor temperature will rise further. The equivalent is true for a vapor that is cooled beyond the vapor spinodal temperature, but the "saturation curve" here is the liquid equilibrium-vapor spinodal curve. With these observations, we will look at the case of a shock tube with a high pressure liquid region to the left of the discontinuity, a low pressure vapor region to the right and a sub-spinodal plateau in the metastable liquid downstream of the rarefaction wave. One would expect a similarity in the form of the solutions to the shock tube problem with and without thermodynamic relaxation, but different values of pressure and velocities. We will look closer at the numerical solution to such a scenario in section 4.2.4 and see that this is the case.

When used in a two-phase numerical solver, the spinodal equilibrium mixture EOS will yield three distinct thermodynamic states within a computational cell. Theoretically, there can be four states if both original states enter the sub-spinodal region, but for simplicity we look at the case of sub-spinodal liquid only. If the pressure in a cell containing a liquid and a vapor state drops below the liquid spinodal pressure, some of the liquid will evaporate. This is a numerical equivalent of homogeneous nucleation, so the generated vapor can be viewed as nuclei within the liquid body that are in mechanical and thermal equilibrium with the liquid. However, the numerical solver only "sees" two phases, so the original and the generated vapor must relax to a common state. By assuming that the total vapor total mass and energy is conserved during the relaxation process, the generated vapor mass and internal energy can simply be added to the original vapor.

2.4.1 The spinodal equilibrium state with the van der Waals EOS

The total internal energy of a two phase mixture in thermal equilibrium is

$$\epsilon = Y_1(4\tau - \frac{3}{\delta_1}) + (1 - Y_1)(4\tau - \frac{3}{\delta_2}) = 4\tau + 3Y_1(\frac{1}{\delta_2} - \frac{1}{\delta_1}) - \frac{3}{\delta_2}. \tag{2.89}$$

Assuming that phase 1 is in the spinodal state $\tau_1 = \tau_s(\delta_1)$ and that the phases are in thermal and mechanical equilibrium (eq. 2.69), we can formulate the mass fraction of phase 1 as

$$Y_1 = \frac{\delta - \delta_2}{\delta_1 - \delta_2} = \frac{-3\delta_1\delta + 2\delta + \delta_1}{3\delta_1 - 3\delta_1^2}. \tag{2.90}$$

We can then write the reduced mixture energy as

$$\begin{aligned} \epsilon &= 4\frac{(1-3\delta_1)^2}{4\delta_1^3} + 3\frac{-3\delta_1\delta + 2\delta + \delta_1}{3\delta_1 - 3\delta_1^2}(\frac{3\delta_1 - 2}{\delta_1} - \frac{1}{\delta_1}) - 3\frac{3\delta_1 - 2}{\delta_1} \\ &= \frac{-9\delta_1^3 + 9\delta_1^2\delta + 12\delta_1^2 - 6\delta_1\delta - 6\delta_1 + 1}{\delta_1^3}. \end{aligned} \tag{2.91}$$

The only unknown is δ_1, so the system can be solved by an iterative procedure or a cubic solver.

The spinodal equilibrium Hugoniot curve

An initial state defined by (δ_0, ϵ_0) and a new state defined by (δ_n, ϵ_n) satisfies the Hugoniot criterion when

$$\epsilon_n - \epsilon_0 + \frac{\pi_n + \pi_0}{2}(\delta_n - \delta_0) = 0 \tag{2.92}$$

In the case of $\epsilon_n < \epsilon_s(\delta_n)$, the spinodal equilibrium mixture EOS is applied at the new state. Inserting the energy equation of the spinodal equilibrium state (2.91) and the spinodal pressure we get

$$\frac{-3\delta_0\delta_1 + 2\delta_0 - 18\delta_1^3 + 18\delta_1^2\delta_n + 24\delta_1^2 - 9\delta_1\delta_n - 12\delta_1 - 2\delta_n + 2}{2\delta_1^3} - \epsilon_0 + \frac{\pi_0}{2}(\delta_n - \delta_0) = 0. \tag{2.93}$$

This equation can be solved for δ_1, either by iteration or directly, using a cubic root solver and some procedure to determine the correct root. An example of a Hugoniot curve for the spinodal equilibrium mixture EOS is provided in Figure 2.6. Note that the initial state may be in the sub-spinodal region. In this case, δ_0 and ϵ_0 are mixture properties.

Negative pressure solution

For the special case of $\delta_1 \leq \frac{2}{3}$, the liquid spinodal pressure will be zero or negative. In this case, no physically valid vapor equilibrium solution exists, since the pressure in the vapor phase is strictly positive. This is mainly a numerical problem, since the pressure relaxation algorithm will ensure a positive equilibrium pressure in all cells. Still, in the presence of steep pressure gradients, a negative liquid pressure can occur before the pressure relaxation step. There is no point in deriving a physically valid solution to this special case, but the solving algorithm must be able to handle it without violating total mass and energy conservation. The numerical solution to this issue is further discussed in section 3.1.1.

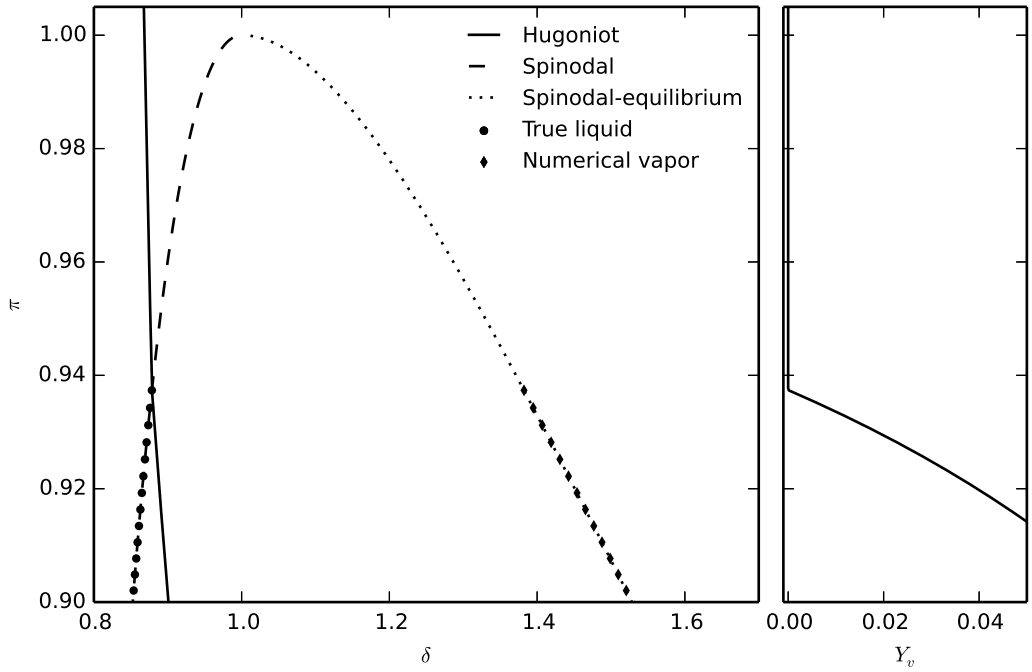

Figure 2.6: The Hugoniot curve for the van der Waals spinodal equilibrium mixture EOS. The plot at the left shows the Hugoniot in π-δ space. When the Hugoniot crosses the spinodal curve, the composition changes from single phase to a true liquid which lies on the spinodal curve and a numerical vapor on the spinodal-equilibrium curve. Inside the spinodal region, the Hugoniot is that of the mixture. The mass fraction of vapor is plotted to the right.

Chapter 3

Numerical solver

3.1 The numerical model

The numerical model used in this work solves the two-pressure 6-equation model given by Saurel et al [36]. Without heat and mass transfer, the model reads:

$$\frac{\partial \alpha_1}{\partial t} + u\frac{\partial \alpha_1}{\partial x} = \mu(p_1 - p_2), \tag{3.1a}$$

$$\frac{\partial \alpha_1\rho_1}{\partial t} + \frac{\partial \alpha_1\rho_1 u}{\partial x} = 0, \tag{3.1b}$$

$$\frac{\partial \alpha_2\rho_2}{\partial t} + \frac{\partial \alpha_2\rho_2 u}{\partial x} = 0, \tag{3.1c}$$

$$\frac{\partial \rho u}{\partial t} + \frac{\partial \rho u^2 + (\alpha_1 p_1 + \alpha_2 p_2)}{\partial x} = 0, \tag{3.1d}$$

$$\frac{\partial \alpha_1\rho_1 e_1}{\partial t} + \frac{\partial \alpha_1\rho_1 e_1 u}{\partial x} + \alpha_1 p_1 \frac{\partial u}{\partial x} = -p_I\mu(p_1 - p_2), \tag{3.1e}$$

$$\frac{\partial \alpha_2\rho_2 e_2}{\partial t} + \frac{\partial \alpha_2\rho_2 e_2 u}{\partial x} + \alpha_2 p_2 \frac{\partial u}{\partial x} = -p_I\mu(p_1 - p_2). \tag{3.1f}$$

The right hand side terms corresponds to pressure relaxation. p_I is the interfacial pressure, estimated by

$$p_I = \frac{Z_2 p_1 + Z_1 p_2}{Z_1 + Z_2}, \tag{3.2}$$

where $Z_k = \rho_k c_k$ is the acoustic impedance of phase k. The numerical method makes use of the redundant total energy transport equation:

$$\frac{\partial \rho(Y_1 e_1 + Y_2 e_2 + \frac{1}{2}u^2)}{\partial t} + \frac{\partial u\left(\rho(Y_1 e_1 + Y_2 e_2 + \frac{1}{2}u^2) + (\alpha_1 p_1 + \alpha_2 p_2)\right)}{\partial x} = 0. \tag{3.3}$$

The mixture speed of sound used in this model is the frozen speed of sound,

$$c_f^2 = Y_1 c_1^2 + Y_2 c_2^2. \tag{3.4}$$

The model is strictly hyperbolic with wave speeds $(u + c_f, u - c_f, u)$. In the present work, we use stiff pressure relaxation ($\mu \to \infty$). As shown in [36], this means the recovery of the 5-equation model.

An overview of the main algorithm can be found in Appendix B.1.

3.1.1 The HLLC Riemann solver

We make use of the HLLC (Harten-Lax-van Leer-Contact) Riemann solver that was introduced by Toro [37]. It was extended to multiphase flow by Saurel et al [36]. It provides an approximate solution to the general Riemann problem defined by

$$U = \begin{cases} U_L \text{ for } x \leq 0 \\ U_R \text{ for } x > 0 \end{cases} \tag{3.5}$$

where

$$U = \begin{pmatrix} \alpha \\ (\alpha\rho)_1 \\ (\alpha\rho)_2 \\ \rho u \\ (\alpha\rho e)_1 \\ (\alpha\rho e)_2 \end{pmatrix} \tag{3.6}$$

The left and right wave speeds are obtained by Davis estimates:

$$S_R = \max(u_L + c_L, u_R + c_R), S_L = \min(u_L - c_L, u_R - c_R) \tag{3.7}$$

where the mixture speed of sound follows relation 3.4. The speed of the contact discontinuity is estimated by the HLL approximation

$$S_M = \frac{(\rho u + p)_L - (\rho u + p)_R - S_L(\rho u)_L + S_R(\rho u)_R}{(\rho u)_L - (\rho u)_R - S_L\rho_L + S_R\rho_R}. \tag{3.8}$$

The mixture variables are defined as

$$p = \alpha_1 p_1 + \alpha_2 p_2, \tag{3.9}$$

$$\rho = \alpha_1\rho_1 + \alpha_2\rho_2. \tag{3.10}$$

The following states are then determined:

$$u^* = SM \tag{3.11}$$

$$(\alpha_k\rho_k)^*_R = (\alpha_k\rho_k)_R \frac{S_R - u_R}{S_R - S_M} \tag{3.12}$$

$$(\alpha_k\rho_k)^*_L = (\alpha_k\rho_k)_L \frac{S_L - u_L}{S_L - S_M} \tag{3.13}$$

$$p^* = p_R + \rho_R u_R(u_R - S_R) - \rho^*_R(S_M - S_R) \tag{3.14}$$

$$E^*_R = \frac{\rho_R E_R(u_R - S_R) + p_R u_R - p * S_M}{\rho^*_R(S_M - S_R)} \tag{3.15}$$

$$E^*_L = \frac{\rho_L E_L(u_L - S_L) + p_L u_L - p * S_M}{\rho^*_L(S_M - S_L)} \tag{3.16}$$

In the absence of relaxation effects, the volume fraction is constant along fluid trajectories:

$$\alpha^*_{kR} = \alpha_{kR}, \alpha^*_{kL} = \alpha_{kL}. \tag{3.17}$$

The fluid densities are then

$$\rho^*_{kR} = \rho_{kR}\frac{S_R - u_R}{S_R - S_M}, \rho^*_{kL} = \rho_{kL}\frac{S_L - u_L}{S_L - S_M}. \tag{3.18}$$

The phasic pressures are determined by the Hugoniot relation,

$$p^*_{kR} = p_{\mathrm{H}}(p_{kR}, \rho_{kR}, \rho^*_{kR}), p^*_{kL} = p_{\mathrm{H}}(p_{kL}, \rho_{kL}, \rho^*_{kL}) \tag{3.19}$$

and the internal energies are determined by the EOS,

$$e^*_{kR} = e(p^*_{kR}, \rho^*_{kR}), e^*_{kL} = e(p^*_{kL}, \rho^*_{kL}) \tag{3.20}$$

The conservative part of U ($U_C = \big((\alpha\rho)_1,\ (\alpha\rho)_2,\ \rho u,\ \rho E\big)^T$) is evolved by (subscript C is omitted for clarity):

$$U^{n+1}_i = U^n_i - \frac{\Delta t}{\Delta x}(F(U^*_{i+1/2}) - F(U^*_{i-1/2})) \tag{3.21}$$

where $F(U_C) = uU_C + \big(0,\ 0,\ \alpha_1 p_1 + \alpha_2 p_2,\ u(\alpha_1 p_1 + \alpha_2 p_2)\big)^T$. The non-conservative variables are determined by

$$\alpha^{n+1}_{1i} = \alpha^n_{1i} - \frac{\Delta t}{\Delta x}((u\alpha_1)^*_{i+1/2} - (u\alpha_1)^*_{i-1/2} - \alpha^n_{1i}(u^*_{i+1/2} - u^*_{i-1/2})) \tag{3.22}$$

and

$$(\alpha\rho e)^{n+1}_{ki} = (\alpha\rho e)^n_{ki} - \frac{\Delta t}{\Delta x}((\alpha\rho eu)^*_{k,i+1/2} - (\alpha\rho eu)^*_{k,i-1/2} - (\alpha p)^n_{ki}(u^*_{i+1/2} - u^*_{i-1/2})). \tag{3.23}$$

Spinodal equilibrium case

If the Hugoniot curves crosses the spinodal curve in the phasic pressure determination step, the spinodal equilibrium EOS will be used. The flux of the sub-spinodal state will then be a mixture of true liquid and numerical vapor, or vice versa. However, no heat or mass transfer will take place between the cell liquid and vapor.

As discussed in section 2.4.1, the liquid Hugoniot curve can reach the spinodal at a negative pressure. We propose the simple solution of setting the liquid state to the intersection state between the Hugoniot and the spinodal curves and the numerical vapor specific volume and pressure to the cell vapor Hugoniot state. The mass fraction of numerical vapor is then calculated from the total liquid density ρ_{lK}^*. The cell liquid internal energy will violate the Hugoniot criterion in this case, as the numerical vapor internal energy is taken as that of the true vapor. However, the mass fraction of numerical vapor will be very small in most cases, so this is a satisfactory approximation. Since the cell interface fluxes are conservative, total mass and energy are conserved.

3.1.2 Second order extension

The HLLC-solver is combined with a MUSCL (Monotone Upstream-centered Scheme for Conservation Laws) type method. The system is assumed to be regular enough to be formulated on primitive variable form:

$$\frac{\partial \alpha_1}{\partial t} + u\frac{\partial \alpha_1}{\partial x} = 0, \tag{3.24a}$$
$$\frac{\partial \rho_1}{\partial t} + u\frac{\partial \rho_1}{\partial x} + \rho_1\frac{\partial u}{\partial x} = 0, \tag{3.24b}$$
$$\frac{\partial \rho_2}{\partial t} + u\frac{\partial \rho_2}{\partial x} + \rho_2\frac{\partial u}{\partial x} = 0, \tag{3.24c}$$
$$\frac{\partial u}{\partial t} + u\frac{\partial \rho u}{\partial x} + \frac{1}{\rho}\frac{\partial p}{\partial x} = 0, \tag{3.24d}$$
$$\frac{\partial p_1}{\partial t} + u\frac{\partial p_1}{\partial x} + \rho_1 c_1^2\frac{\partial u}{\partial x} = 0, \tag{3.24e}$$
$$\frac{\partial p_2}{\partial t} + u\frac{\partial p_2}{\partial x} + \rho_2 c_2^2\frac{\partial u}{\partial x} = 0. \tag{3.24f}$$

This can be written on vector form:

$$\frac{\partial W}{\partial t} + A(W)\frac{\partial W}{\partial x} = 0,\ W = \begin{pmatrix} \alpha_1 \\ \rho_1 \\ \rho_2 \\ u \\ p_1 \\ p_2 \end{pmatrix},\ A(W) = \begin{pmatrix} u & 0 & 0 & 0 & 0 & 0 \\ 0 & u & 0 & \rho_1 & 0 & 0 \\ 0 & 0 & u & \rho_2 & 0 & 0 \\ (p_1-p_2)/\rho & 0 & 0 & u & \alpha_1/\rho & \alpha_2/\rho \\ 0 & 0 & 0 & \rho_1 c_1^2 & u & 0 \\ 0 & 0 & 0 & \rho_2 c_2^2 & 0 & u \end{pmatrix} \tag{3.25}$$

The primitive vectors of a computational cell i are defined by These cell gradient is limited by a slope limiter function. We use the function

$$\Delta_i = \begin{cases} \max\left(0, \min(\beta d_i^-, d_i^+), \min(d_i^-, \beta d_i^+)\right) & \text{for } d_i^+ > 0 \\ \min\left(0, \max(\beta d_i^-, d_i^+), \max(d_i^-, \beta d_i^+)\right) & \text{for } d_i^+ > 0 \end{cases} \tag{3.26}$$

where

$$d_i^- = W_i^n - W_{i-1}^n,\ d_i^+ = W_{i+1}^n - W_i^n. \tag{3.27}$$

$\beta = 1$ corresponds to the Minmod limiter, while $\beta = 2$ corresponds to the Superbee limiter. The Minmod limiter is used in the present work unless otherwise is explicitly stated. The limited gradients are used to extrapolate the cell boundaries

$$W_{i-1/2,R}^n = W_i^n - \frac{\Delta x}{2}\Delta_i,\ W_{i+1/2,L}^n = W_i^n + \frac{\Delta x}{2}\Delta_i \tag{3.28}$$

which are then evolved for half a time step by

$$W^{n+1/2}_{i\pm1/2,K} = W^{n}_{i\pm1/2,K} + \frac{\Delta t}{2\Delta x} A(W^n_i)\left[W_{i-1/2,R} - W_{i+1/2,L}\right]. \tag{3.29}$$

The variable group vector U is reconstructed using the evolved primitive variables for the left and right states of each cell interface, and the Riemann problem is solved using the reconstructed values to find the inter-cell fluxes.

3.1.3 Stiff pressure relaxation

The pressure relaxation step solves the equation set

$$\frac{\partial \alpha_1}{\partial t} = \mu(p_1 - p_2), \tag{3.30}$$

$$\frac{\partial \alpha_1\rho_1 e_1}{\partial t} = -p_I\mu(p_1 - p_2), \tag{3.31}$$

$$\frac{\partial \alpha_2\rho_2 e_2}{\partial t} = p_I\mu(p_1 - p_2) \tag{3.32}$$

in the limit $\mu \to \infty$. All other conserved variable groups are held constant during the relaxation step. According to [36], this system of equations can be replaced by

$$e_k(p, v_k) - e^0_k(p^0_k, v^0_k) + \hat{p}_I(v_k - v^0_k) = 0,\ k = 1, 2 \tag{3.33}$$

and the saturation constraint

$$(\alpha\rho)_1 v_1 + (\alpha\rho)_2 v_2 = 1 \tag{3.34}$$

where $(\alpha\rho)_k$ is constant during the relaxation step. The system can be closed by an equation of state $e_k(\rho_k, p_k)$. Equation 3.33 can then be reformulated to $v_k(p)$ by using an estimate of $\hat{p}_I$. In the present work, the estimation $\hat{p}_I = p^0_I$ is used, but other estimates can also be used as shown by [36]. Finally, we insert the expressions for v_k into eq. 3.34 and solve for p.

Since the pressure estimated by this method is not guaranteed to be in agreement with the mixture equation of state $p(\rho, e, \alpha_1)$, this pressure is only used to find the relaxed volume fraction α_1. The relaxed pressure is then determined by the mixture equation of state and the internal energy from the redundant total energy equation. The conserved variables $(\alpha\rho e)_k$ are then re-initialized using the relaxed pressure and volume fraction. This ensures the conservation of mixture energy in the flow field.

Alternate relaxation methods can also be used. Both isentropic and isenthalpic relaxation methods has been tested with the same results as the method described here. This gives reason to assume that the thermodynamic relaxation path is of lesser importance, since it is only used to estimate the relaxed volume fraction. If the numerical method is expanded to a more complex EOS, this means that the pressure relaxation process most likely can be resolved with a less rigorous estimate of the thermodynamic relaxation path.

Solving procedure - SG-EOS

The relaxed pressure can be found analytically with the SG-EOS. Equation 3.33 can be reformulated to

$$v_k(p) = v^0_k \frac{p^0 + \gamma_k p_{\infty k} + (\gamma_k - 1)\hat{p}_I}{p + \gamma_k p_{\infty k} + (\gamma_k - 1)\hat{p}_I} \tag{3.35}$$

The expressions for the relaxed specific volumes are then inserted into Equation 3.34:

$$G_1 v^0_1 \frac{p^0_1 + \gamma_1 p_{\infty 1} + (\gamma_1 - 1)p^0_I}{p + \gamma_1 p_{\infty 1} + (\gamma_1 - 1)p^0_I} + G_2 v^0_2 \frac{p^0_2 + \gamma_2 p_{\infty 2} + (\gamma_2 - 1)p^0_I}{p + \gamma_2 p_{\infty 2} + (\gamma_2 - 1)p^0_I} = 1 \tag{3.36}$$

where $G_k \equiv (\alpha\rho)_k$. This equation can be formulated as

$$c_0 p^2 + c_1 p + c_2 = 0 \tag{3.37}$$

where

$$
\begin{aligned}
c_0 &= -1 \\
c_1 &= A_1 + A_2 - B_1 - B_2 \\
c_2 &= A_1 B_2 + A_2 B_1 - B_1 B_2 \\
A_k &= G_k v_k^0 \left[p_k^0 + \gamma_k p_{\infty k} + (\gamma_k - 1) p_I^0 \right] \\
B_k &= \gamma_k p_{\infty k} + (\gamma_k - 1) p_I^0
\end{aligned}
$$

The physical root of Equation 3.37 is given by

$$
p = \frac{-c_1 - \sqrt{c_1^2 - 4 c_0 c_2}}{2 c_0}. \tag{3.38}
$$

The volume fraction is found using this pressure and the system is re-initialized by the mixture EOS,

$$
p(\rho, e, \alpha_1, \alpha_2) = \frac{\rho e - \dfrac{\alpha_1 \gamma_1 p_{\infty 1}}{\gamma_1 - 1} - \dfrac{\alpha_2 \gamma_2 p_{\infty 2}}{\gamma_2 - 1}}{\dfrac{\alpha_1}{\gamma_1 - 1} + \dfrac{\alpha_2}{\gamma_2 - 1}} \tag{3.39}
$$

An outline of the pressure relaxation algorithm can be found in Appendix B.2.

Solving procedure - vdW-EOS

With the reduced vdW-EOS, eq. 3.33 can be written as

$$
\pi(\delta_k) = \frac{2 C_k \delta_k^2 \hat{\pi}_I - 2 \delta_k^3 \hat{\pi}_I - 3 \delta_k + 3}{\delta_k^2 (3 \delta_k - 1)}, \tag{3.40}
$$

where

$$
C_k = \delta_k^0 + \frac{1}{\hat{\pi}_I} \left[\frac{1}{2} (\pi_k^0 + \frac{3}{(\delta_k^0)^2})(3 \delta_k^0 - 1) - \frac{3}{\delta_k^0} \right]. \tag{3.41}
$$

Since we have no mass transfer, we can write

$$
G_1 \delta_1 + G_2 \delta_2 = 1. \tag{3.42}
$$

where $G_k = (\alpha \rho)_k v_c$. From this, we get

$$
\delta_2(\delta_1) = \frac{1 - G_1 \delta_1}{G_2} \tag{3.43}
$$

The algorithm for stiff pressure relaxation solves the equation $f(\delta_1) = 0$ by the Newton-Raphson method, where

$$
\begin{aligned}
& f(\delta_1) = \pi_1(\delta_1) - \pi_2(\delta_1), \\
& \frac{\mathrm{d}\pi_k}{\mathrm{d}\delta_1} = \left(-\hat{\pi}_I \frac{6 C_k - 2}{(3 \delta_k - 1)^2} + \frac{6(3\delta_k^2 - 5\delta_k + 1)}{\delta_k^3 (3 \delta_k - 1)^2} \right) d_k, \\
& d_1 = 1, \; d_2 = -\frac{G_1}{G_2}
\end{aligned}
$$

3.1.4 Stiff thermodynamic relaxation

The thermodynamic relaxation method used presently differs somewhat from the methods used by [4,17]. It is simpler in formulation and relatively easy to implement for any equation of state. We consider a two phase system with total density $\rho = \alpha_1 \rho_1 + \alpha_2 \rho_2$ and total internal energy $e = Y_1 e_1 + Y_2 e_2$. Since no mass or heat is added to the system during the relaxation step, these mixture properties are constant. We will consider the velocity of the two phases to be equal and constant during the relaxation step. Initially, the system is closed by the known variables ρ_1, ρ_2, e_1, e_2. In the numerical solver used

presently, the two phases will be in mechanical equilibrium at the start of the relaxation step, but this is not a prerequisite of the procedure. The system can be uniquely determined by requiring complete thermodynamic equilibrium between the two phases:

$$p_1 = p_2 = p,\ T_1 = T_2 = T,\ g_1 = g_2 = g. \tag{3.44}$$

Note that this requirement is not possible for all ρ and e. This is indeed the case when there is only a single phase solution, that is when the limit of complete evaporation or condensation is reached. Since the numerical method is only valid for $\alpha_k > \xi$, where ξ is some small number (typically $\xi = 10^{-6}$), the single phase limit of phase 1 will be determined by

$$p_1 = p_2 = p,\ T_1 = T_2 = T,\ \alpha_1 = 1 - \xi \tag{3.45}$$

and equivalent for the single phase limit of phase 2. If a cubic equation of state is used, even this is not possible for all ρ and e. This will be the case when one phase reaches the spinodal state before thermal equilibrium is reached. If phase 2 is at the spinodal state, the system is determined by

$$p_1 = p_2 = p_{\text{spin}}(v_2) = p,\ T_1 = T(v_1, p),\ T_2 = T_{\text{spin}}(v_2),\ \alpha_1 = 1 - \xi. \tag{3.46}$$

v_2 is determined by the mixture equation of state, and v_1 is determined by conservation of mass ($v = Y_1 v_1 + Y_2 v_2$).

In the context of the van der Waals EOS, the three cases (3.44, 3.45 and 3.46) can be identified by the values of ρ and e. A discussion of this can be found in section 2.3.10. A fourth case is theoretically possible, namely $e < e(\rho)_{T=0}$, but this is not likely to occur in numerical calculations and is therefore not further examined.

The stiff thermodynamic relaxation procedure was used when $p_l < p_{\text{sat}}(T_l)$. In some of the calculations, the additional criterion $\xi_I < \alpha_1 < 1 - \xi_I$ was used, where ξ_I represents the interface limit of the volume fraction (typically $\xi_I = 10^2\xi$ to $10^3\xi$). This last criterion is referred to as the interface criterion of the thermodynamic relaxation procedure and was used to allow for the formation of metastable liquid.

Algorithm - SG-EOS

The thermodynamic relaxation algorithm for the SG-EOS solves the equation

$$g_2(p, T) - g_1(p, T) = 0 \tag{3.47}$$

by iteration using the Newton-Rhapson method and the fact that the pressure and temperature can be expressed as functions of the vapor volume fraction α_1:

$$p(\alpha_1) = \frac{-c_1 - \sqrt{c_1^2 + 4c_0c_2}}{2c_0} \tag{3.48}$$

$$p' = \frac{1}{2c_0^2}\left[\frac{c_0(-2c_2c_0' - 2c_0c_2' + c_1c_1')}{2\sqrt{c_1^2 + 4c_0c_2}} - c_0c_1' - c_0'(-c_1 + \sqrt{c_1^2 + 4c_0c_2})\right] \tag{3.49}$$

and

$$T(\alpha_1) = \frac{k_1(p + \pi_1)}{A_1p + B_1} \tag{3.50}$$

$$T' = \frac{k_1p'(A_1p + B_1) - (p + \pi_1)(pA_1' + p'A_1 + B_1')}{(A_1p + B_1)^2} \tag{3.51}$$

where

$$
\begin{aligned}
c_0 &= A_2k_1 - A_1k_2 \\
c_1 &= k_1(B_2 + A_2\pi_1) - k_2(B_1 + A_1\pi_2) \\
c_2 &= k_1B_2\pi_1 - k_2B_1\pi_2 \\
c_0' &= A_2'k_1 - A_1'k_2 \\
c_1' &= k_1(B_2' + A_2'\pi_1) - k_2(B_1' + A_1'\pi_2) \\
c_2' &= k_1B_2'\pi_1 - k_2B_1'\pi_2 \\
k_1 &= \frac{\beta_1}{c_{v1}} \\
k_2 &= \frac{\beta_2}{c_{v2}} \\
A_1 &= -\frac{\alpha_1\beta_1 + \alpha_2\beta_2}{\alpha_1(q_1 - q_2)} \\
A_2 &= \frac{\alpha_1\beta_1 + \alpha_2\beta_2}{\alpha_2(q_1 - q_2)} \\
B_1 &= \frac{\rho e - \alpha_1\eta_1 - \alpha_2\eta_2 - q_2\rho}{\alpha_1(q_1 - q_2)} \\
B_2 &= -\frac{\rho e - \alpha_1\eta_1 - \alpha_2\eta_2 - q_1\rho}{\alpha_2(q_1 - q_2)} \\
A_1' &= \frac{\beta_2}{\alpha_1^2(q_1 - q_2)} \\
A_2' &= \frac{\beta_1}{\alpha_2^2(q_1 - q_2)} \\
B_1' &= \frac{-\rho e + \eta_2 + q_2\rho}{\alpha_1^2(q_1 - q_2)} \\
B_2' &= \frac{-\rho e + \eta_1 + q_1\rho}{\alpha_2^2(q_1 - q_2)}
\end{aligned}
$$

Superscript $'$ denotes vapor volume fraction derivative ($\frac{d}{d\alpha_1}$). Finally, we give the derivatives of the Gibbs free energies:

$$
\frac{d}{d\alpha_1}g_k = \left[Tc_{vk}\gamma_k p' - (p + \pi_k)T'(c_{vk}\log\left(\frac{T^{\gamma_k}}{(p + \pi_k)^{\gamma_k - 1}}\right) + q_k')\right]/(p + \pi_k) \tag{3.52}
$$

Note that q_k' is the energy correction coefficient of the SG-EOS. If the limit of pure phase is reached before thermodynamic equilibrium ($\alpha_1 < \xi$ or $\alpha_1 > 1 - \xi$), the solution $\alpha_1 = \xi$ or $\alpha_1 = 1 - \xi$, $p_1 = p_2 = p(\alpha_1)$, $T_1 = T_2 = T(\alpha_1)$ is chosen.

Algorithm - vdW-EOS

The thermodynamic relaxation algorithm for the vdW-EOS is determined by the energy limits described in section 2.3.10, that is

$$
\delta > 1 : \begin{cases} \epsilon > \epsilon_{\text{max,thermal}} : \text{ Complete evaporation, non} - \text{equal temperature} \\ \epsilon > \epsilon_{\text{max,thermodynamic}} : \text{ Complete evaporation, equal temperature} \\ \epsilon \leq \epsilon_{\text{max,thermodynamic}} : \text{ Equilibrium solution} \end{cases}
$$

$$
\delta \leq 1 : \begin{cases} \epsilon > \epsilon_{\text{max,thermal}} : \text{ Complete condensation, non} - \text{equal temperature} \\ \epsilon > \epsilon_{\text{max,thermodynamic}} : \text{ Complete condensation, equal temperature} \\ \epsilon \leq \epsilon_{\text{max,thermodynamic}} : \text{Equilibrium solution} \end{cases}
$$

Assuming phase 1 is in the spinodal state, the non equal temperature solution is found by setting α_1 to the phase limit and solving

$$
f(\delta_1) = Y(\delta_1)\left(\epsilon_1(\delta_1) - \epsilon_2(\delta_1)\right) + \epsilon_2(\delta_1) - \epsilon = 0 \tag{3.53}
$$

by iteration, where

$$\epsilon_1 = \epsilon_s(\delta_1), \tag{3.54}$$

$$\epsilon_2 = \epsilon(\delta_2, \tau_2), \tag{3.55}$$

$$\delta_2 = \frac{\alpha_1 \delta \delta_1}{(\alpha_1 - 1)\delta + \delta_1}, \tag{3.56}$$

$$\tau_2 = \tau(\delta_2, \pi_s(\delta_1)) \tag{3.57}$$

and

$$Y = \frac{\delta - \delta_2}{\delta_1 - \delta_2}. \tag{3.58}$$

The procedure is completely analogous when phase 2 is in the spinodal state.

Assuming phase 1 is in the spinodal state, the equal temperature non-equilibrium solution is found by setting α_1 to the phase limit and solving

$$f(\delta_1) = \delta_{2,\delta} - \delta_{2,\epsilon} = 0 \tag{3.59}$$

by iteration, where

$$\delta_{2,\delta} = \frac{1 - \alpha_1}{\frac{1}{\delta} - \frac{\alpha_1}{\delta_1}} \tag{3.60}$$

and $\delta_{2,\epsilon}$ is found by solving

$$\epsilon = Y_2(\epsilon_2 - \epsilon_1) + \epsilon_1 = \delta \frac{1 - \alpha_1}{\delta_2}(-\frac{3}{\delta_2} + \frac{3}{\delta_1}) + \epsilon_s(\delta_1) \tag{3.61}$$

for δ_2. Again, the procedure is completely analogous when phase 2 is in the spinodal state.

Lastly, the full equilibrium solution is found by a nested iteration procedure. From a first guess of δ_1, the δ_2 corresponding to thermodynamic equilibrium is found by solving equation 2.59 by iteration. δ_1 is then corrected so that

$$\epsilon = Y_1 \epsilon(\delta_1, \tau) + Y_2 \epsilon(\delta_2, \tau). \tag{3.62}$$

These two steps are repeated until the mixture energy matches that of the computational cell and the reduced volumes fulfils equation 2.59. The first guess of δ_1 is found from a table lookup of pre-calculated values from combinations of δ and ϵ.

When a solution has been found, the system is then re-initialized using the mixture EOS.

The entire algorithm is outlined in Appendix B.3

3.2 Analytical Riemann solver

An exact Riemann solver was used for validation purposes. As shown in [38], the exact solution to the Riemann problem of the single pressure and velocity 5-equation model without heat and mass transfer can be found, assuming that the mixture speed of sound follows the Woods relation

$$\frac{1}{\rho c^2} = \frac{\alpha_1}{\rho_1 c_1^2} + \frac{\alpha_2}{\rho_2 c_2^2}. \tag{3.63}$$

The method used by [38] for the SG-EOS is reproduced for completeness and extended to the vdW-EOS. In addition, a solution to the Riemann problem in the case of stiff thermodynamic relaxation is found.

The five equation system of Kapila et al. [39] reads:

$$\begin{aligned}
&\frac{\partial \alpha_1}{\partial t} + u \frac{\partial \alpha_1}{\partial x} = \frac{\rho_2 c_2^2 - \rho_1 c_1^2}{\frac{\rho_1 c_1^2}{\alpha_1} + \frac{\rho_2 c_2^2}{\alpha_2}} \frac{\partial u}{\partial x}, \\
&\frac{\partial \alpha_1 \rho_1}{\partial t} + \frac{\partial \alpha_1 \rho_1 u}{\partial x} = 0, \\
&\frac{\partial \alpha_2 \rho_2}{\partial t} + \frac{\partial \alpha_2 \rho_2 u}{\partial x} = 0, \\
&\frac{\partial \rho u}{\partial t} + \frac{\partial \rho u^2 + p}{\partial x} = 0, \\
&\frac{\partial \rho E}{\partial t} + \frac{\partial (\rho E + p) u}{\partial x} = 0.
\end{aligned}$$

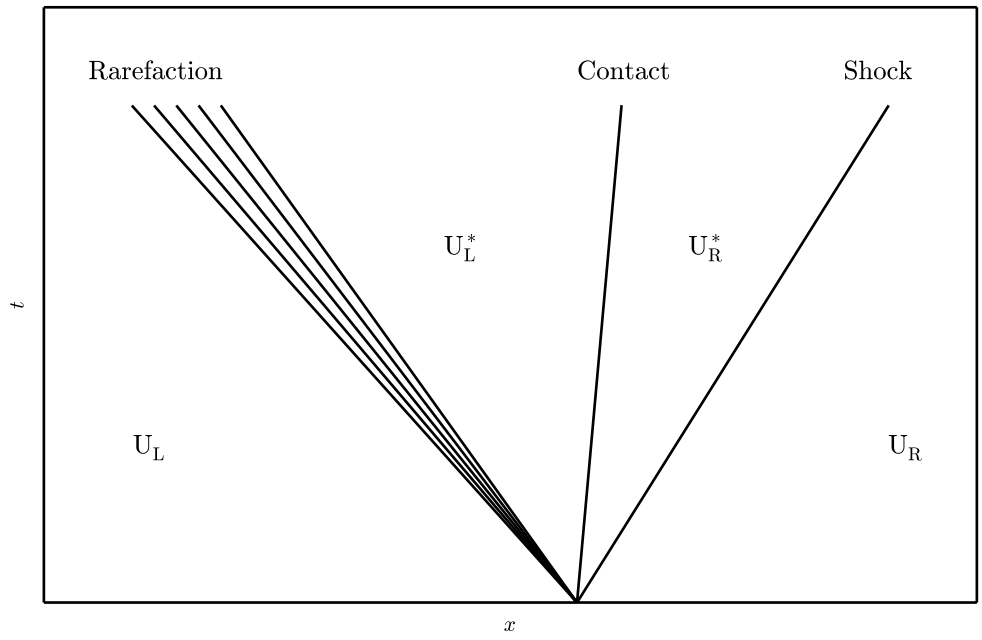

Figure 3.1: x-t plot of the Riemann problem without heat and mass transfer where $p_L > p^* > p_R$.

Without heat and mass transfer, the solution of the Riemann problem consists of two waves, either rarefaction- or shock-waves depending on the initial conditions, as illustrated in Figure 3.1.

3.2.1 Rarefaction waves without heat and mass transfer

Rarefaction waves travelling at velocity $\sigma = u \pm c_w$ have the Riemann invariants

$$\begin{aligned} \mathrm{d}p &= \pm \rho c_w \mathrm{d}u, \\ \mathrm{d}p &= c_w^2 \mathrm{d}\rho, \\ \mathrm{d}Y_1 &= 0, \\ \mathrm{d}s_1 &= 0, \\ \mathrm{d}s_2 &= 0. \end{aligned}$$

Using the last two relations, the phasic densities at any pressure in a rarefaction wave can be found by isentropic expansion,

$$\rho_k = \rho(p, p^0, \rho_k^0)_{\mathrm{d}s=0}. \tag{3.64}$$

The mixture entropy reads $\mathrm{d}s = \sum Y_k \mathrm{d}s_k = 0$, so that the second relation yields a wave speed that corresponds to the definition of the mixture speed of sound,

$$c_w^2 = \left(\frac{\mathrm{d}p}{\mathrm{d}\rho}\right)_s. \tag{3.65}$$

The material velocity of the rarified state is obtained by integrating the inverse mixture acoustic impedance ρc_w. The mixture acoustic impedance is derived from the Woods relation,

$$\rho c_w = \left(\frac{Y_1}{\rho_1^2 c_1^2} + \frac{Y_2}{\rho_2^2 c_2^2}\right)^{-1/2}. \tag{3.66}$$

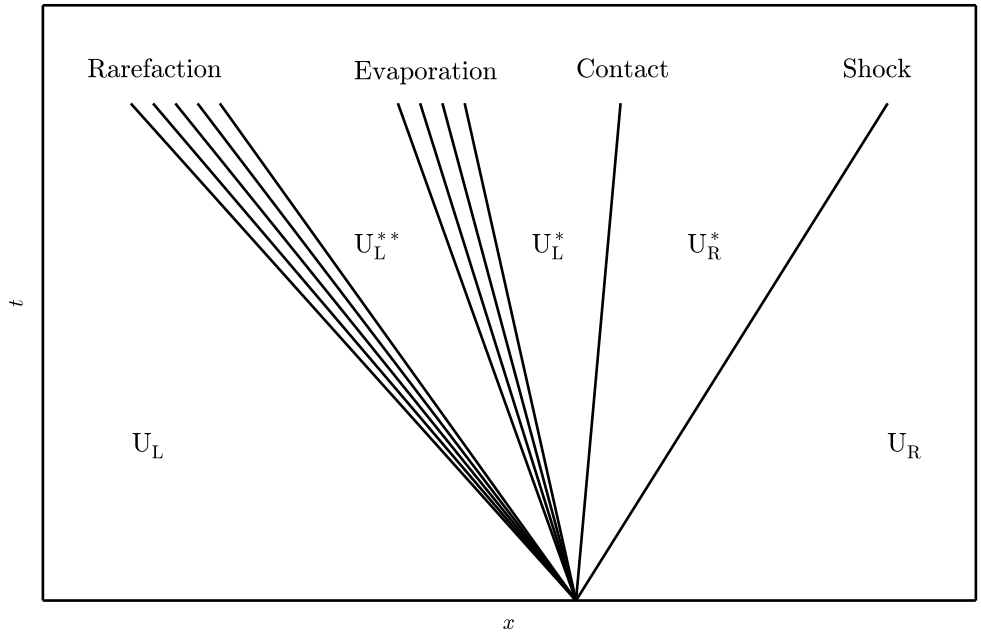

Figure 3.2: x-t plot of the Riemann problem where $p_L > p_R$, $p_L^* < p_{\text{sat}}(\rho_L^*)$ and with stiff thermodynamic relaxation

SG-EOS

The density at the isentrop is found by

$$\rho_k = \rho_k^0 \left(\frac{p + p_\infty}{p^0 + p_\infty} \right)^{\frac{1}{\gamma_k}}. \tag{3.67}$$

The phasic speed of sound is

$$c_k^2 = \frac{\gamma(p + p_\infty)}{\rho_k} \tag{3.68}$$

The square acoustic impedance of phase k at the rarified state can then be written as

$$c_k^2 \rho_k^2 = (c_k^0 \rho_k^0)^2 \left(\frac{p + p_\infty}{p^0 + p_\infty} \right)^{\frac{\gamma_k + 1}{\gamma_k}} \tag{3.69}$$

vdW-EOS

With the vdW-EOS, assuming a solution exists, we have the isentropic relation

$$(\delta_k^0 - \frac{1}{3})(\tau_k^0)^{3/2} - (\delta_k - \frac{1}{3})\tau_k^{3/2} = 0. \tag{3.70}$$

This is solved for $\delta_k(p)$ by iteration and the square acoustic impedance is found by

$$\rho_k^2 c_k^2 = p_c v_c^3 \left(\frac{40\tau_k}{(1 - 3\delta_k)^2} - \frac{6}{\delta_k^3} \right) \tag{3.71}$$

Rarefaction fan

The rarefaction fan is enclosed by the head and tail with the characteristic speeds

$$S_H = u^0 \pm c^0, S_T = u^* \pm c^* \tag{3.72}$$

Any general point $(x,\, t)$ inside the fan has the characteristic slope

$$\frac{x}{t} = u(p) \pm c(p),\ p^* < p < p^0 \tag{3.73}$$

3.2.2 Shock

Jump conditions for the system are

$$\begin{aligned}
&(\alpha\rho)_k^*(u^* - \sigma) = (\alpha\rho)_k^0(u^0 - \sigma)\\
&\rho^* u^*(u^* - \sigma) + p^* = \rho^0 u^0(u^0 - \sigma) + p^0\\
&\rho^* E^*(u^* - \sigma) + p^* u^* = \rho^0 E^0(u^0 - \sigma) + p^0 u^0
\end{aligned}$$

which can also be written as

$$\begin{aligned}
&Y^* = Y^0\\
&\rho^*(u^* - \sigma) = \rho^0(u^0 - \sigma) = m\\
&p^* - p^0 + m^2(v^* - v^0) = 0\\
&e^* - e^0 + \frac{p^* + p^0}{2}(v^* - v^0) = 0
\end{aligned}$$

The system is closed with the phasic Hugoniot-relations,

$$\rho_k^* = \rho_k^H(\rho_k^0, p^0, p^*) \tag{3.74}$$

The speed of the shock wave is found by conservation of mass:

$$\sigma = \frac{(\rho u)^* - (\rho u)^0}{\rho^* - \rho^0} \tag{3.75}$$

Shock relations with stiff thermodynamic relaxation are not used in the present work, and are therefore not provided. However, it can be done by treating the mixture as a single eulerian fluid (as in section 3.2.3), substituting $Y^* = Y^0$ above with the thermodynamic equilibrium condition and using the mixture saturation Hugoniot.

3.2.3 Rarefaction waves with stiff thermodynamic relaxation

In the case of stiff thermodynamic relaxation, the five equation system reduces to the classical single phase Euler equations:

$$\begin{aligned}
&\frac{\partial \rho}{\partial t} + \frac{\partial \rho u}{\partial x} = 0,\\
&\frac{\partial \rho u}{\partial t} + \frac{\partial \rho u^2 + p}{\partial x} = 0,\\
&\frac{\partial \rho E}{\partial t} + \frac{\partial (\rho E + p)u}{\partial x} = 0.
\end{aligned}$$

If the internal energy of the system lies in the coexistence region, ρ and E are properties of a mixture in thermodynamic equilibrium. Otherwise, the system describes a single phase. The Riemann invariants of the system are

$$\begin{aligned}
&\mathrm{d}p = \pm\rho S_W \mathrm{d}u,\\
&\mathrm{d}p = (S_W)^2 \mathrm{d}\rho,\\
&\mathrm{d}s = 0
\end{aligned}$$

The wave speed S_W can then be defined by the second and third equation

$$(S_W)^2 = \left(\frac{\mathrm{d}p}{\mathrm{d}\rho}\right)_s, \tag{3.76}$$

which by definition is the speed of sound. Note that the speed of sound in the coexistence region is defined by

$$(c_{\mathrm{sat}})^2 \equiv \left(\frac{\partial p_{\mathrm{sat}}}{\partial \rho}\right)_s, \tag{3.77}$$

which creates a discontinuity in the speed of sound at the binodal, since the saturation speed of sound in general is much lower than the single phase speed of sound. This leads to a wave splitting when a rarefaction wave in the single phase region enters the coexistence region as illustrated in Figure 3.2. The region between the two waves, denoted by the superscript $**$, is defined by the intersection point between the isentrop from the initial conditions and the binodal curve. A rarefaction wave in a mixture in thermodynamic equilibrium is an evaporation wave, since part of the liquid evaporates to maintain the equilibrium. The density at any point in the evaporation wave is given by the mixture isentrop,

$$\rho_W = \rho(s_0, p). \tag{3.78}$$

From this, the speed of sound is determined:

$$c = \begin{cases} c_{\mathrm{sat}} & \text{for } p < p_{\mathrm{sat}}(\rho) \\ c_{\mathrm{sp}} & \text{for } p \geq p_{\mathrm{sat}}(\rho) \end{cases} \tag{3.79}$$

where the subscript sp denotes single phase. In the split waves case, the two rarefaction fans are enclosed by the heads and tails with the characteristic speeds

$$\begin{aligned} S_{H,\mathrm{sp}} &= u^0 \pm c_{\mathrm{sp}}(p^0, \rho^0) \\ S_{T,\mathrm{sp}} &= u^{**} \pm c_{\mathrm{sp}}(p^{**}, \rho^{**}) \\ S_{H,\mathrm{sat}} &= u^{**} \pm c_{\mathrm{sat}}(p^{**}, \rho^{**}) \\ S_{T,\mathrm{sat}} &= u^{*} \pm c_{\mathrm{sat}}(p^{*}, \rho^{*}) \end{aligned}$$

Sub-spinodal rarefaction waves

The wave splitting procedure can be used for a sub-spinodal fluid ($e < e_{\mathrm{spin}}(\rho)$). In this case, the binodal curve is replaced by the spinodal-equilibrium curve for the spinodal phase, so that

$$(S_W)^2 = (c_{\mathrm{spin}})^2 \equiv \left(\frac{\partial p_{\mathrm{spin}}}{\partial \rho}\right)_s \tag{3.80}$$

Note that this is only valid when the two phases remain in thermal equilibrium throughout the evaporation wave.

3.2.4 Algorithm

The Riemann problem is solved by expressing the material velocity on the form

$$u_L^* = u_L - \Phi_L(p^*), u_R^* = u_R + \Phi_R(p^*) \tag{3.81}$$

and requiring $u_L^* = u_R^* = u^*$. The correct pressure p^* is found by iteration. The function $\Phi_K(p^*)$ is given by

$$\Phi_K(p) = \begin{cases} \frac{p-p^0}{m} & \text{for } p > p^0 \text{ (Shock)} \\ \int_p^{p^0} \frac{\mathrm{d}p}{\rho c_w} & \text{for } p \leq p^0 \text{ (Rarefaction)} \end{cases} \tag{3.82}$$

The integral $\int_p^{p^0} \frac{\mathrm{d}p}{\rho c_w}$ is computed numerically using the Gauss-Legendre method:

$$\int_p^{p^0} \frac{\mathrm{d}p}{\rho c_w} = \frac{p-p^0}{2} \sum_{k=1}^{n} \omega_k \frac{1}{(\rho c_w)_{p_k}}, \tag{3.83}$$

$$p_k = \frac{p+p^0}{2} + \frac{p-p^0}{2}\xi_k. \tag{3.84}$$

Six points are used. The numerical values of ω_k and ξ_k are provided in Appendix A.3

Chapter 4

Numerical solver validation

4.1 Validation of the SG-EOS solver

Since both the mechanic and the thermodynamic relaxation procedures that are used in the present work are different from those used by Saurel et al. and Zein et al., validation test cases using the SG-EOS are included. The numerical tests are performed both with and without thermodynamic relaxation. The test cases are compared to the analytical solution when this is available.

4.1.1 Advection of a volume fraction discontinuity

A volume fraction discontinuity advection test was performed. The purpose of this test is to show that a flow in mechanical equilibrium stays stays in equilibrium in throughout the numerical process. The test setup that was used is equal to the test setup found in [36]. Air-water EOS were used, along with the following initial conditions:

	p	u	α_{air}	ρ_{air}	ρ_{water}
$x < 0.5\,\text{m}$	$10^5\,\text{Pa}$	$100\,\text{m/s}$	10^{-8}	$10\,\text{kg/m}^3$	$10^3\,\text{kg/m}^3$
$x \geq 0.5\,\text{m}$	$10^5\,\text{Pa}$	$100\,\text{m/s}$	$1{-}10^{-8}$	$10\,\text{kg/m}^3$	$10^3\,\text{kg/m}^3$

200 numerical cells were used with a computational domain spanning 1 m. The Superbee limiter was used. A comparison between the analytical and the numerical solution at $t = 2.79\,\text{ms}$ is shown in Figure 4.1. Excellent agreement is observed and the solution is oscillation free.

4.1.2 Liquid-vapor shock tube

A shock tube with almost pure liquid on the high pressure side and almost pure vapor at the low pressure side was set up with the following initial conditions:

	p	u	α	ρ_1	ρ_2
$x < 0.5\,\text{m}$	$10^8\,\text{Pa}$	$0\,\text{m/s}$	10^{-6}	$2\,\text{kg/m}^3$	$500\,\text{kg/m}^3$
$x \geq 0.5\,\text{m}$	$10^5\,\text{Pa}$	$0\,\text{m/s}$	$1{-}10^{-6}$	$2\,\text{kg/m}^3$	$500\,\text{kg/m}^3$

Dodecane vapor and liquid SG-EOS were used. 1250 numerical cells were used with a computational domain spanning 1 m. This test setup is the same as the one used in [36]. The test were run with no thermodynamic relaxation, relaxation at the interface only and relaxation when $T_2 > T_{\text{sat}}(p)$. The first two tests were run with CFL = 0.5 and the last test with CFL = 0.1. A comparison between the single phase analytical solution and the numerical solution without thermodynamic relaxation at $t = 4.73 \times 10^{-4}\,\text{s}$ is shown in Figure 4.2. There is excellent agreement between the single phase analytical and the numerical solution. The numerical solution with thermodynamic relaxation at the interface only, using an interface limit of 10^{-4} is shown in Figure 4.3. No analytical solution exists for this test case, but the results are in perfect agreement with [36]. A third test configuration was used, with

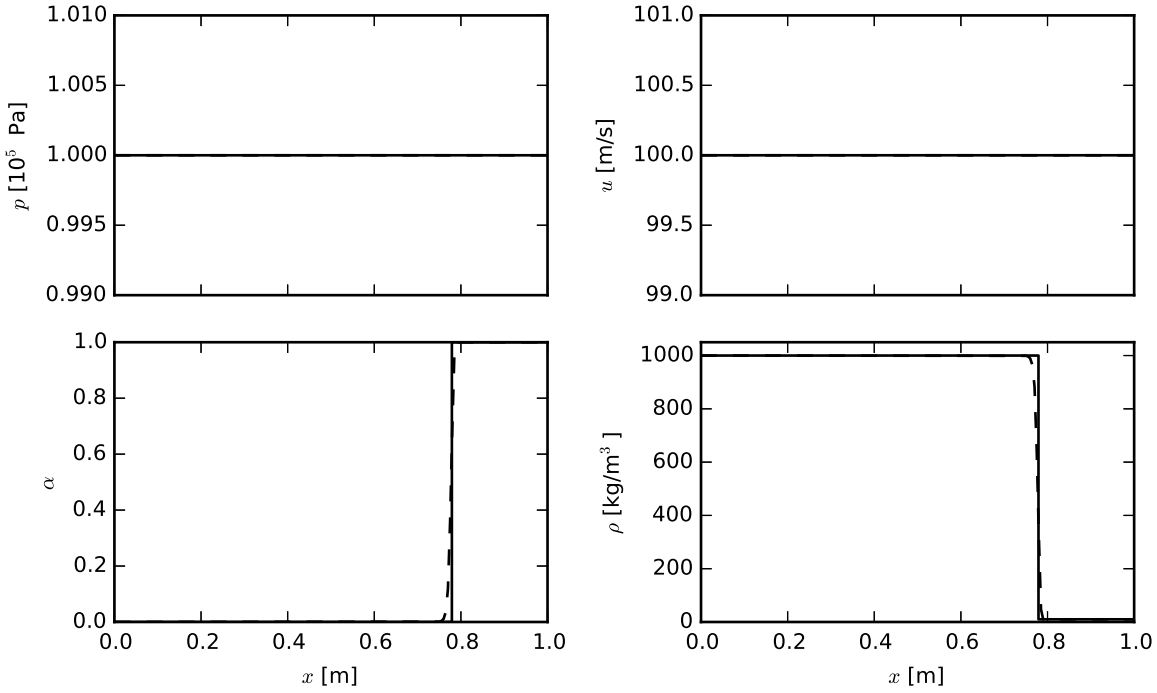

Figure 4.1: Comparison between the analytical (solid line) and the numerical (dashed line) solution to the advection of a volume fraction discontinuity in a water-air mixture in mechanical equilibrium. $t = 2.79\,\mathrm{ms}$

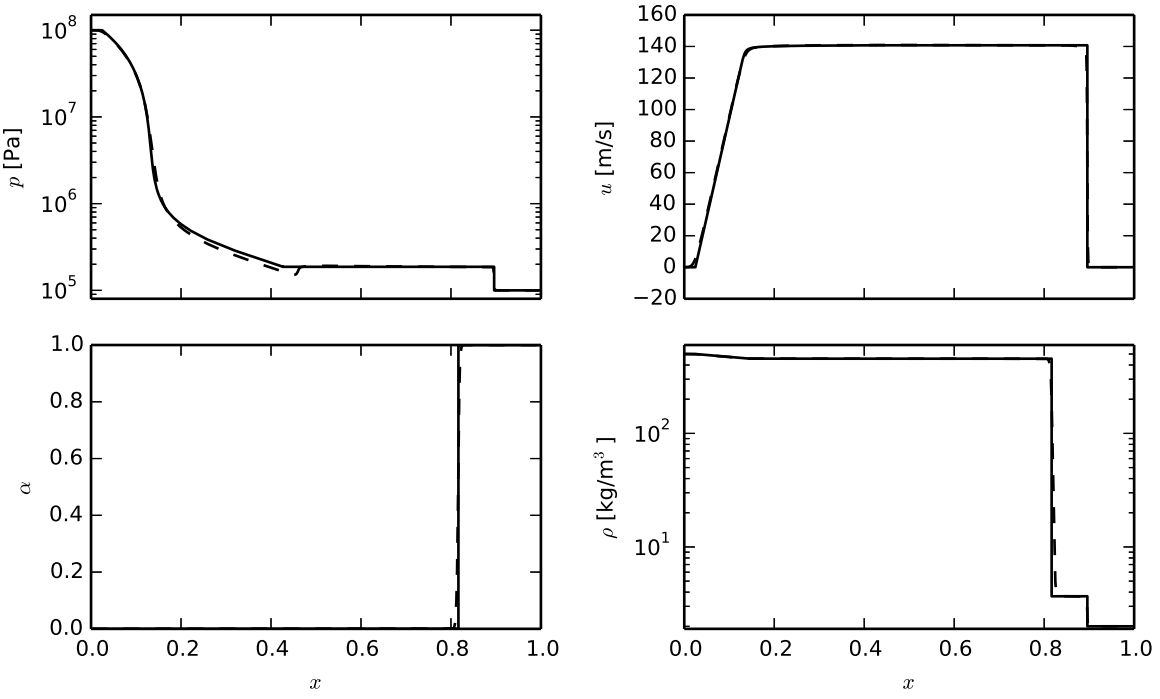

Figure 4.2: Comparison between the analytical single phase solution (solid line) and the numerical solution (dashed line) to the liquid-vapor shock tube, without thermodynamic relaxation. $t = 4.73 \times 10^{-4}$ s

thermodynamic relaxation for all metastable liquid. Note that an upper limit of pressure was applied so that no thermodynamic relaxation was used for $p > 2.0 \times 10^7$ Pa. This is necessary because the saturation temperature for the two-phase SG-EOS system is non-monotonic with regard to pressure. The numerical solution was compared to the analytical one as shown in Figure 4.4. There is excellent agreement between the two solutions.

4.1.3 Cavity test

A cavity test with liquid water was conducted. This test is equivalent to the one done by Zein et al [17]. Water vapor and liquid SG-EOS were used with the following initial conditions:

	p	u	α	ρ_1	ρ_2
$x < 0.5\,\mathrm{m}$	10^5 Pa	-2 m/s	10^{-2}	$10\,\mathrm{kg/m^3}$	$10^3\,\mathrm{kg/m^3}$
$x \geq 0.5\,\mathrm{m}$	10^5 Pa	2 m/s	$1-10^{-2}$	$10\,\mathrm{kg/m^3}$	$10^3\,\mathrm{kg/m^3}$

5000 numerical cells were used with a computational domain spanning 1 m. The test was run both with and without thermodynamic relaxation. Both tests were run with CFL = 0.5. A comparison between the analytical and the numerical solution without thermodynamic relaxation can be found in Figure 4.5. Good agreement is observed. The results for the test with thermodynamic relaxation for $T_2 > T_{\mathrm{sat}}(p)$ can be found in Figure 4.6. There is relatively good agreement between the analytical and the numerical solution, but due to numerical diffusion, the evaporation wave is a bit "smeared out". The numerical diffusion was the same with both minmod and superbee slope limiter.

To demonstrate the evaporation wave in the cavity test more clearly, the velocity was increased to $|u| = 100\,\mathrm{m/s}$. A comparison between the numerical and the analytical solution at $t = 1.5\,\mathrm{ms}$ can be found in Figure 4.7. The results are in agreement with the analytical solution, but some numerical diffusion of the evaporation front is observed.

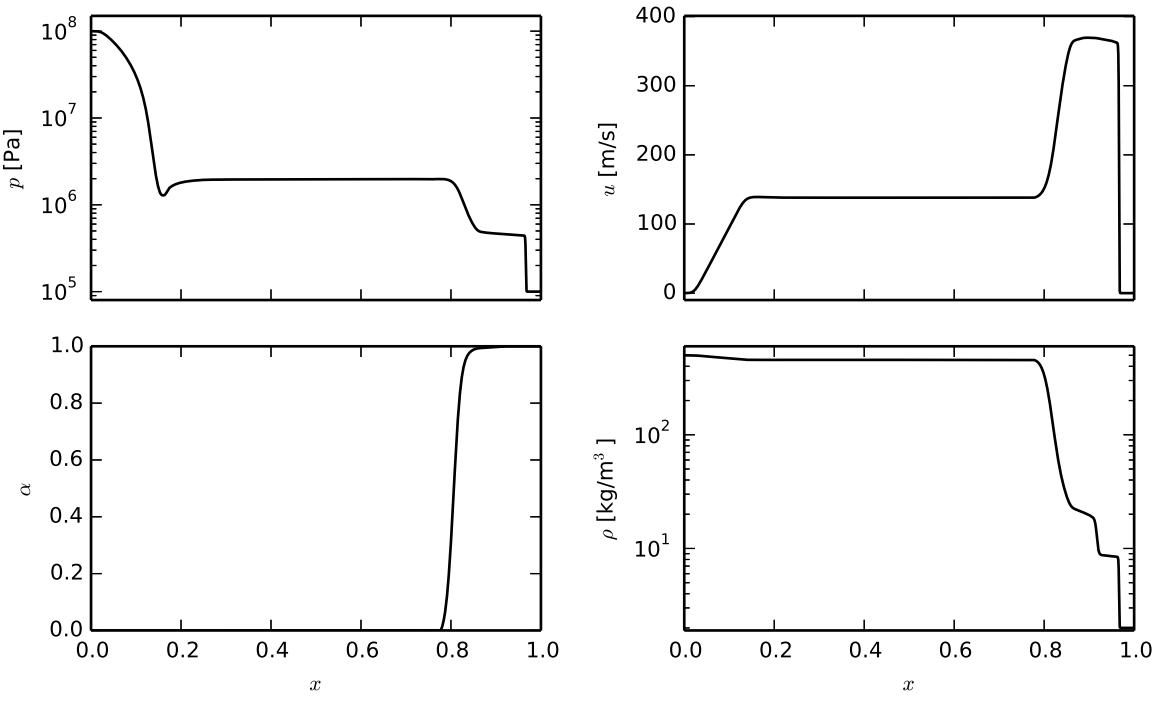

Figure 4.3: Numerical solution to the liquid-vapor shock tube test, with thermodynamic relaxation at the interface only. No analytical solution exists. $t = 4.73 \times 10^{-4}\,\mathrm{s}$

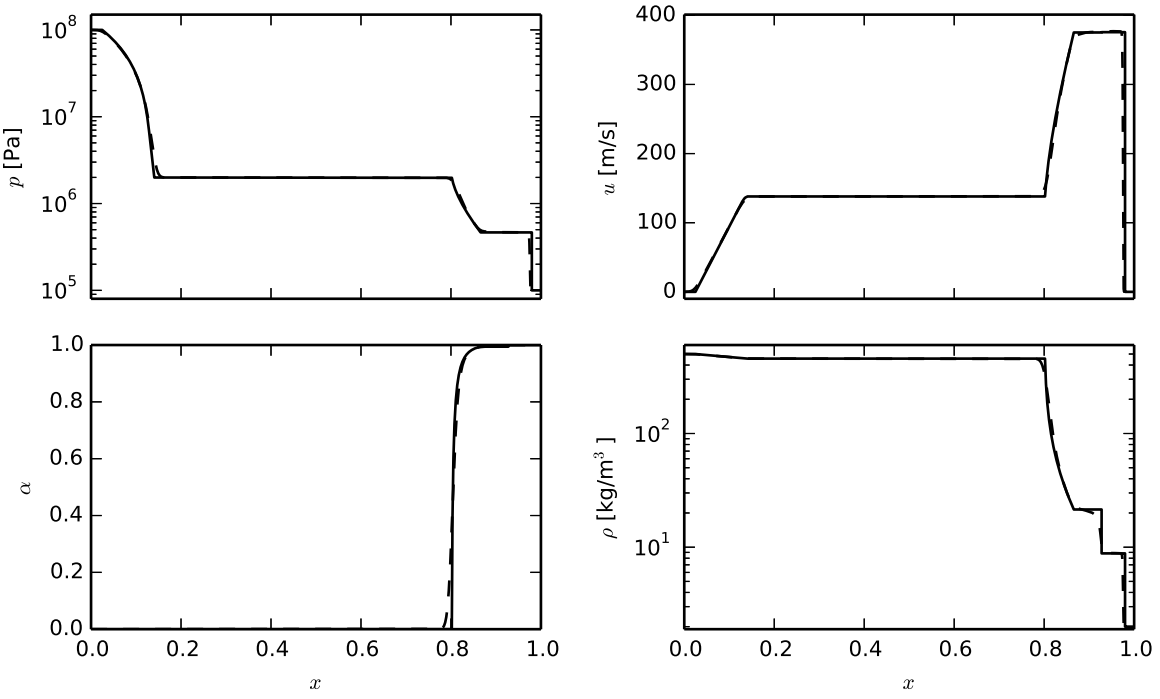

Figure 4.4: Comparison between the analytical solution (solid line) and the numerical solution (dashed line)to the liquid-vapor shock tube test, with thermodynamic relaxation when $T_2 > T_{\mathrm{sat}}(p)$. $t = 4.73 \times 10^{-4}\,\mathrm{s}$

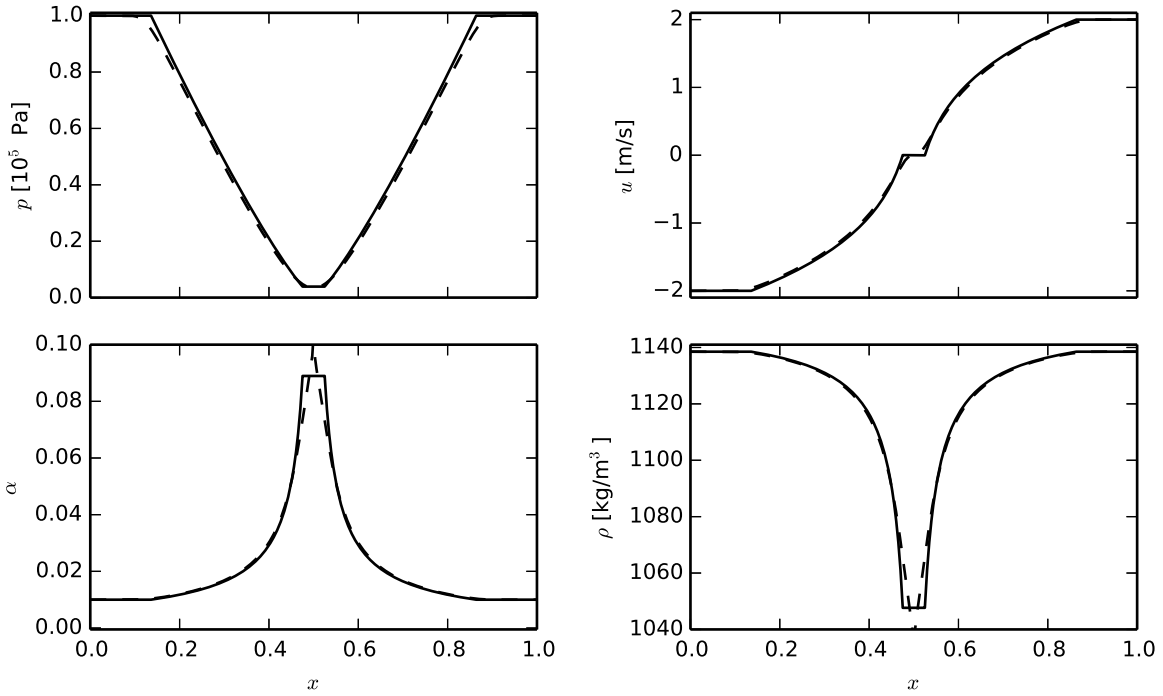

Figure 4.5: Comparison between the analytical solution (solid line) and the numerical solution (dashed line) to the liquid-vapor expansion tube, without thermodynamic relaxation. $t = 3.2 \times 10^{-3}\,\mathrm{s}$

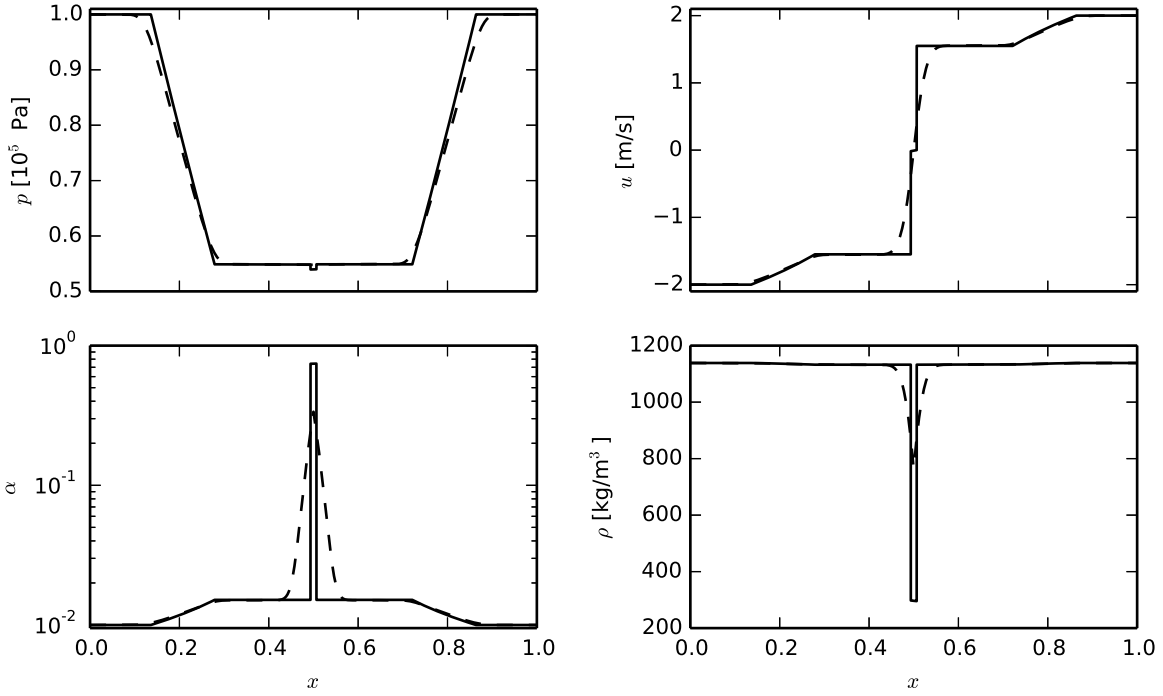

Figure 4.6: Comparison between the analytical solution (solid line) and the numerical solution (dashed line) to the liquid-vapor expansion tube, with thermodynamic relaxation. $t = 3.2 \times 10^{-3}\,\mathrm{s}$

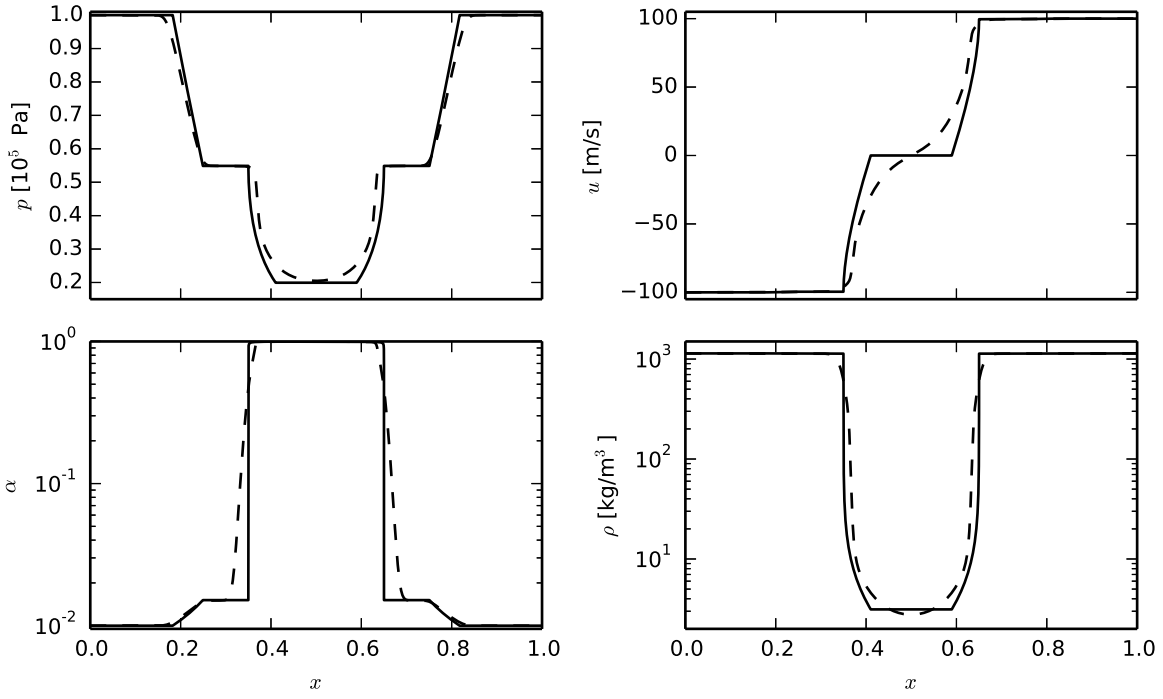

Figure 4.7: Comparison between the analytical solution (solid line) and the numerical solution (dashed line) to the high-velocity liquid-vapor expansion tube, with thermodynamic relaxation. $t = 1.5\,\text{ms}$

4.2 Validation of the vdW-EOS solver

All simulations in this section was run with the van der Waals representation of dodecane. Numerical values for the coefficients used can be found in Appendix A.2.

4.2.1 Contact discontinuity advection

An important requirement of the numerical model is that a flow in mechanical equilibrium stays stays in equilibrium in throughout the numerical process. As shown by Saurel and Abgrall, an equation of state on Mie Gruneisen form is locally reduced to a SG-EOS when the phasic densities are constant on both sides of a volume fraction discontinuity ($\rho_{k,L} = \rho_{k,R}$). Since the van der Waals EOS can be written on Mie Gruneisen form, this approximation holds. The results of a numerical test where a volume fraction discontinuity is propagated by a constant velocity can be found in Figure 4.8. The results are oscillation free. The calculations were done with CFL = 0.5 and 200 cells spanning a computational area of 1 m. The initial conditions were:

	p	u	α	ρ_1	ρ_2
$x < 0.4\,\text{m}$	$10^6\,\text{Pa}$	$100\,\text{m/s}$	10^{-8}	$50\,\text{kg/m}^3$	$243\,\text{kg/m}^3$
$x \geq 0.4\,\text{m}$	$10^6\,\text{Pa}$	$100\,\text{m/s}$	$1{-}10^{-8}$	$50\,\text{kg/m}^3$	$243\,\text{kg/m}^3$

4.2.2 Liquid-vapor single phase limit shock tube

A shock tube with almost pure liquid on the high pressure side and almost pure vapor at the low pressure side was set up with the following initial conditions:

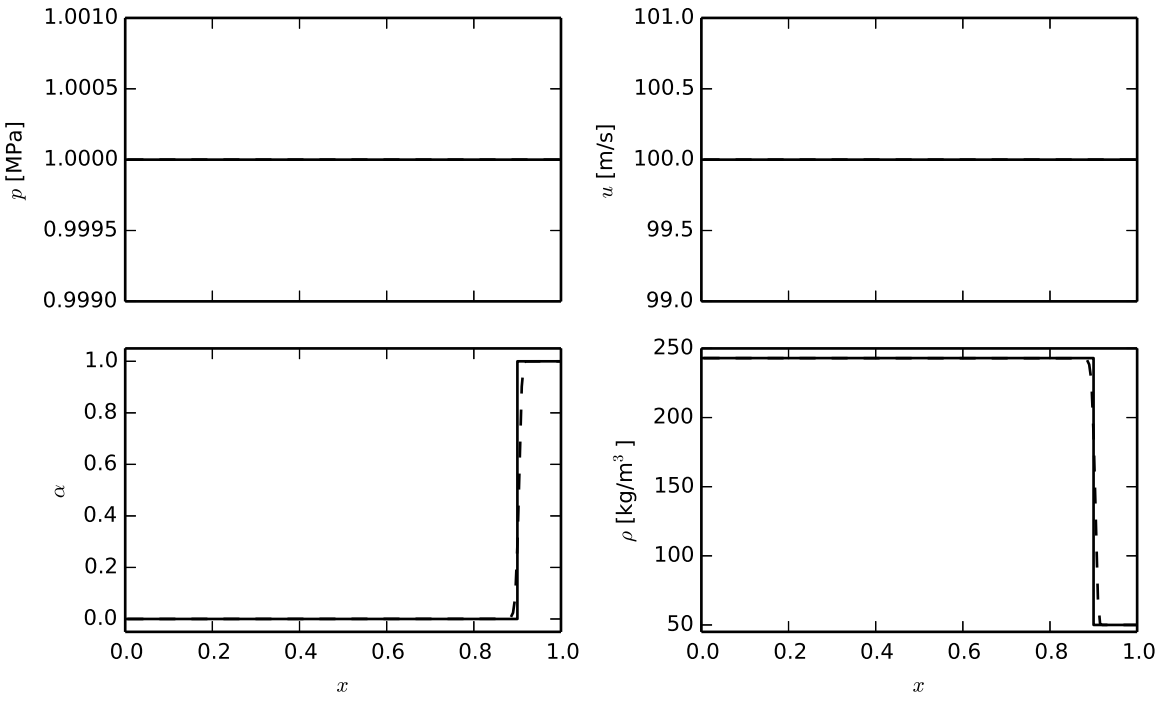

Figure 4.8: Comparison between the analytical single phase solution (solid line) and the numerical solution (dashed line) to the advection of a volume fraction discontinuity. Solution time = 5 ms.

	p	u	α	ρ_1	ρ_2
$x < 0.7\,\mathrm{m}$	$10^8\,\mathrm{Pa}$	$0\,\mathrm{m/s}$	10^{-6}	$50\,\mathrm{kg/m^3}$	$390\,\mathrm{kg/m^3}$
$x \geq 0.7\,\mathrm{m}$	$10^5\,\mathrm{Pa}$	$0\,\mathrm{m/s}$	$1{-}10^{-6}$	$0.75\,\mathrm{kg/m^3}$	$300\,\mathrm{kg/m^3}$

1000 numerical cells were used with a computational domain spanning 1 m. The test were run with no thermodynamic relaxation, relaxation at the interface only and relaxation when $T_2 > T_{\mathrm{sat}}(p)$. A CFL number 0.5 was used in all three calculations. A comparison between the single phase analytical solution and the numerical solution without thermodynamic relaxation at $t = 320\,\mu\mathrm{s}$ is shown in Figure 4.9. There is excellent agreement between the single phase analytical and the numerical solution. The numerical solution with thermodynamic relaxation at the interface only, using an interface limit of 10^{-4} is shown in Figure 4.10. No analytical solution exists for this test case. A third test configuration was used, with thermodynamic relaxation for all metastable liquid. The numerical solution was compared to the analytical one as shown in Figure 4.11. There is excellent agreement between the two solutions, except for some minor oscillations in the vapor shock region.

4.2.3 Expansion tube

An expansion tube test was performed to show the dynamic creation of cavitation and interfaces. The test results at t =1.8 ms are shown without thermodynamic relaxation in Figure 4.12 and with thermodynamic relaxation in Figure 4.13. The interface criterion was not used. A CFL number 0.5 was used in both calculations. The calculations were done with 5000 cells spanning a computational area of 1 m. The initial conditions were:

	p	u	α	ρ_1	ρ_2
$x < 0.5\,\mathrm{m}$	$10^5\,\mathrm{Pa}$	$-2\,\mathrm{m/s}$	10^{-2}	$6.82\,\mathrm{kg/m^3}$	$374.45\,\mathrm{kg/m^3}$
$x \geq 0.5\,\mathrm{m}$	$10^5\,\mathrm{Pa}$	$2\,\mathrm{m/s}$	10^{-2}	$6.82\,\mathrm{kg/m^3}$	$374.45\,\mathrm{kg/m^3}$

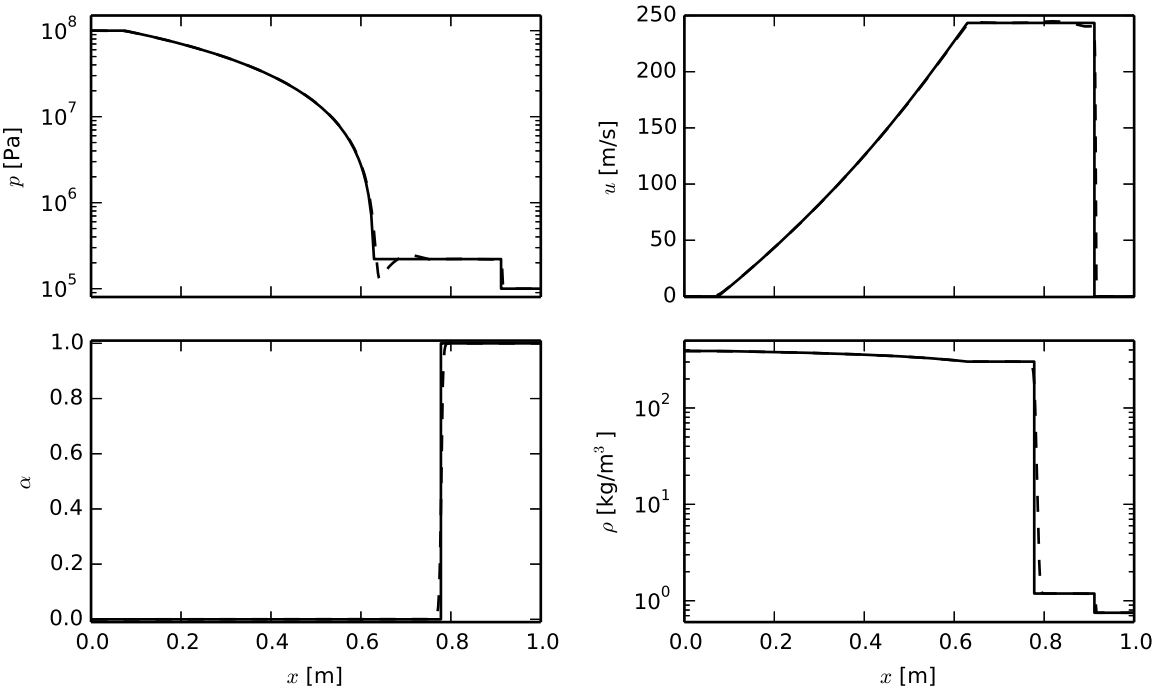

Figure 4.9: Comparison between the analytical single phase solution (solid line) and the numerical solution (dashed line) to the liquid-vapor shock tube, without thermodynamic relaxation. $t = 320\,\mu s$

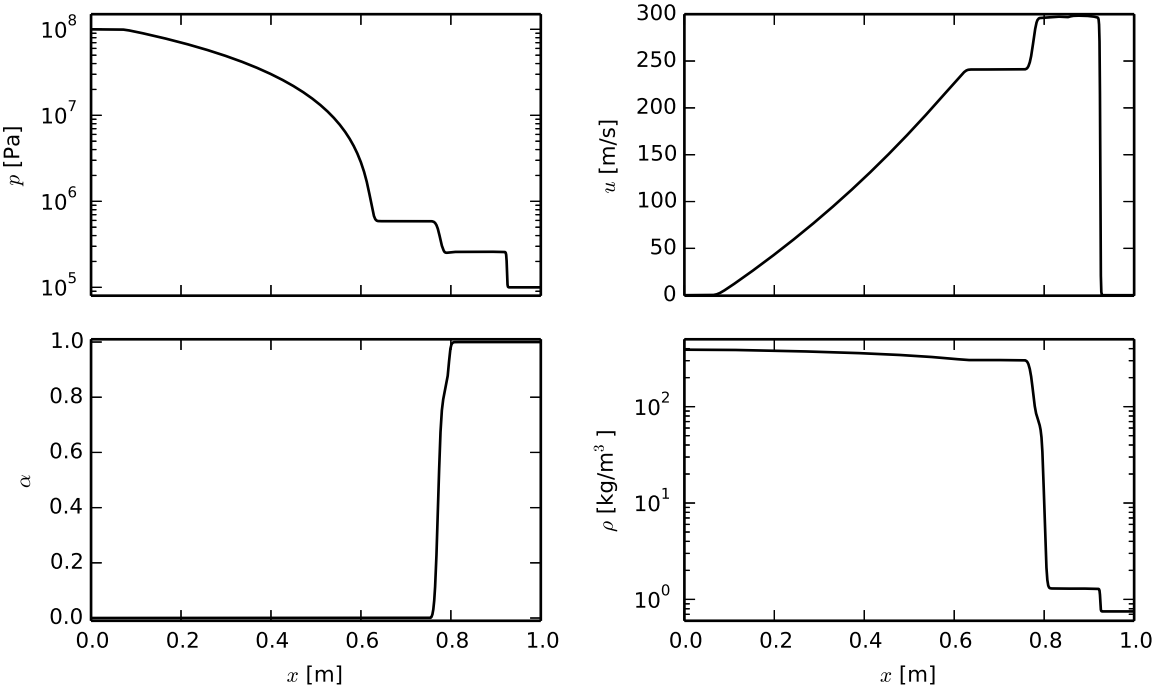

Figure 4.10: Numerical solution to the liquid-vapor shock tube test, with thermodynamic relaxation at the interface only. No analytical solution exists. $t = 320\,\mu s$

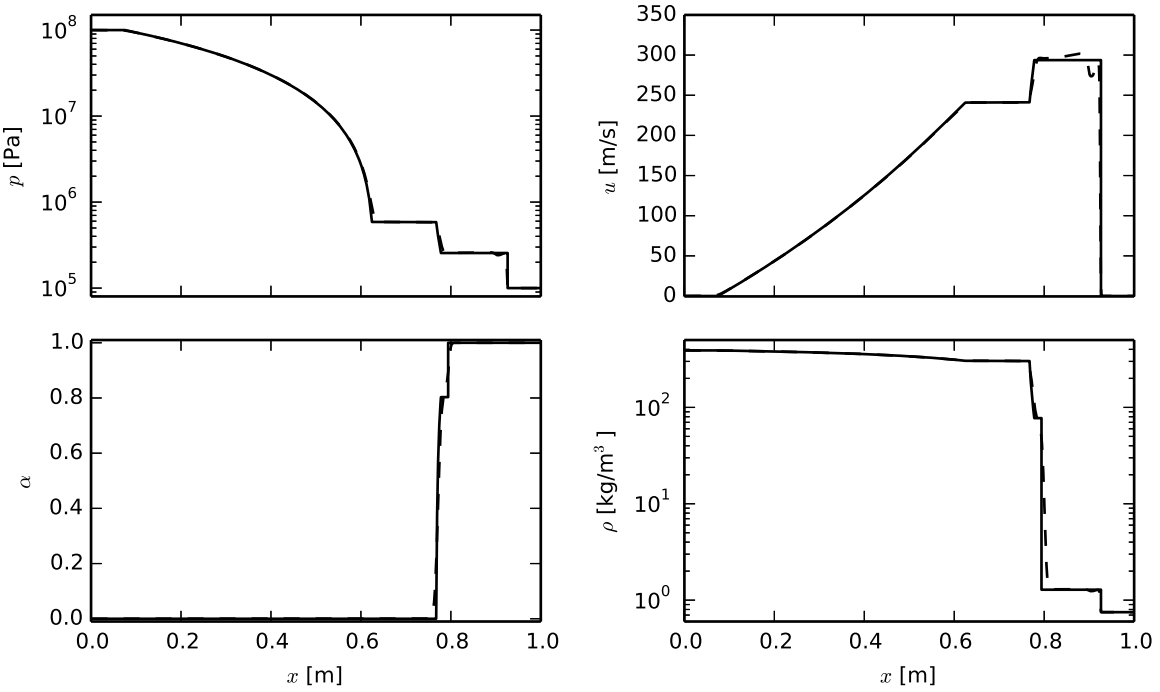

Figure 4.11: Comparison between the analytical solution (solid line) and the numerical solution (dashed line) to the liquid-vapor shock tube test with thermodynamic relaxation when $T_2 > T_{\text{sat}}(p)$. $t = 320\,\mu\text{s}$

A high velocity test case was used, where the velocity was increased to $|u| = 100\,\text{m/s}$. A comparison between the numerical and the analytical solution at $t = 1.4\,\text{ms}$ can be found in Figure 4.14.

4.2.4 Sub-spinodal rarefaction waves

In order to illustrate the capability of the numerical code in the presence of sub-spinodal rarefaction waves, a liquid-vapor shock tube type numerical test was run. The initial conditions were chosen to ensure that the rarefaction wave propagating into the high pressure liquid would bring the liquid to the spinodal state. No thermodynamic relaxation was used, but a minimal amount of phase transition was allowed to ensure that the liquid did not enter the (non-physical) sub-spinodal region. Note that this test case is not meant to represent a physical situation, but rather to illustrate the behaviour of the algorithm in the presence of sub-spinodal states. In a physical situation, the liquid at the spinodal state would undergo a rapid phase-transition, even in the absence of nucleation sites. There is no analytical solution to the two-phase non-equilibrium spinodal rarefaction wave, but for low vapor volume-fractions, the equilibrium spinodal rarefaction wave can be used as an estimate. The numerical solution as well as the analytical estimate at t =1.2 ms are shown in Figure 4.15. There is good agreement between the two solutions, apart from a small discrepancy in the state downstream of the spinodal rarefaction wave, especially in the volume fraction and velocity curves. This is assumed to be caused by the fact that the spinodal-equilibrium rarefaction wave is a good estimate only for α close to zero. The test was also run with thermodynamic relaxation when $T_2 > T_{\text{sat}}(p)$ for reference purposes. The results of the reference case, also at t =1.2 ms, are shown in Figure 4.16.

The CFL number was set to 0.1 in both calculations. The calculations were done with 1000 cells spanning a computational area of 1 m and the following initial conditions

	p	u	α	ρ_1	ρ_2
$x < 0.5\,\text{m}$	$1.835 \times 10^6\,\text{Pa}$	$0\,\text{m/s}$	10^{-6}	$15.2\,\text{kg/m}^3$	$242.5\,\text{kg/m}^3$
$x \geq 0.5\,\text{m}$	$9.2 \times 10^4\,\text{Pa}$	$0\,\text{m/s}$	$1{-}10^{-6}$	$3.04\,\text{kg/m}^3$	$304.24\,\text{kg/m}^3$

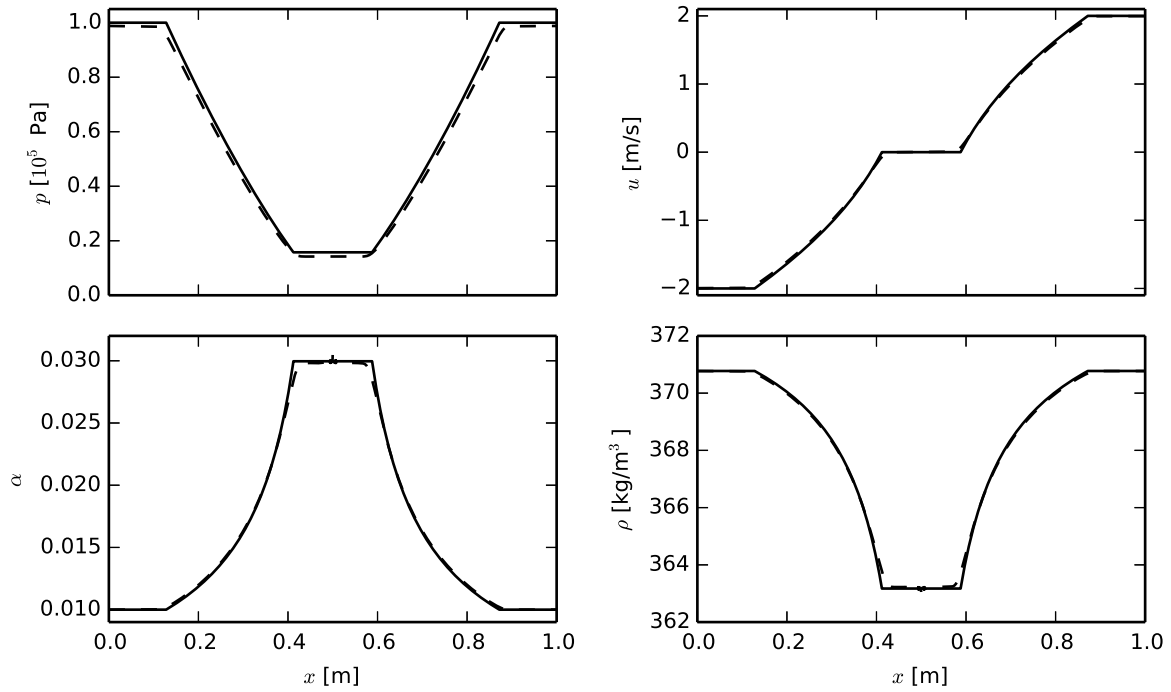

Figure 4.12: Comparison between the analytical two phase solution (solid line) and the numerical solution (dashed line) to the expansion tube, without thermodynamic relaxation. t =1.8 ms

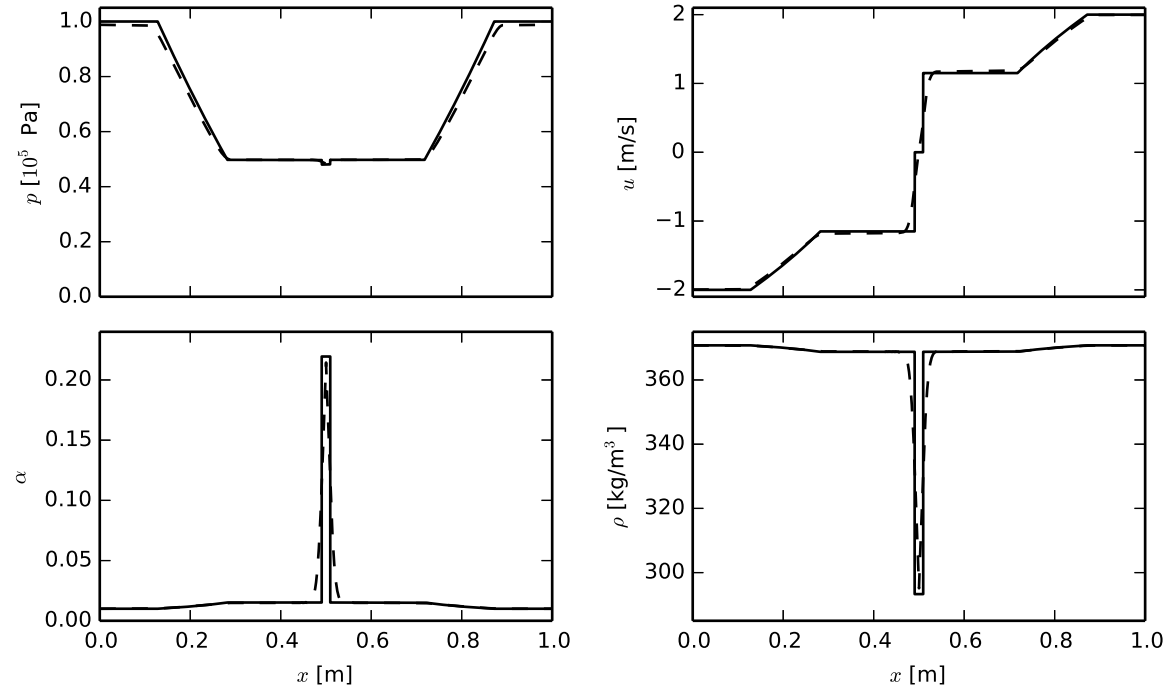

Figure 4.13: Comparison between the analytical two phase solution (solid line) and the numerical solution (dashed line) to the expansion tube, with thermodynamic relaxation when $T_2 > T_{\text{sat}}(p)$. t =1.8 ms

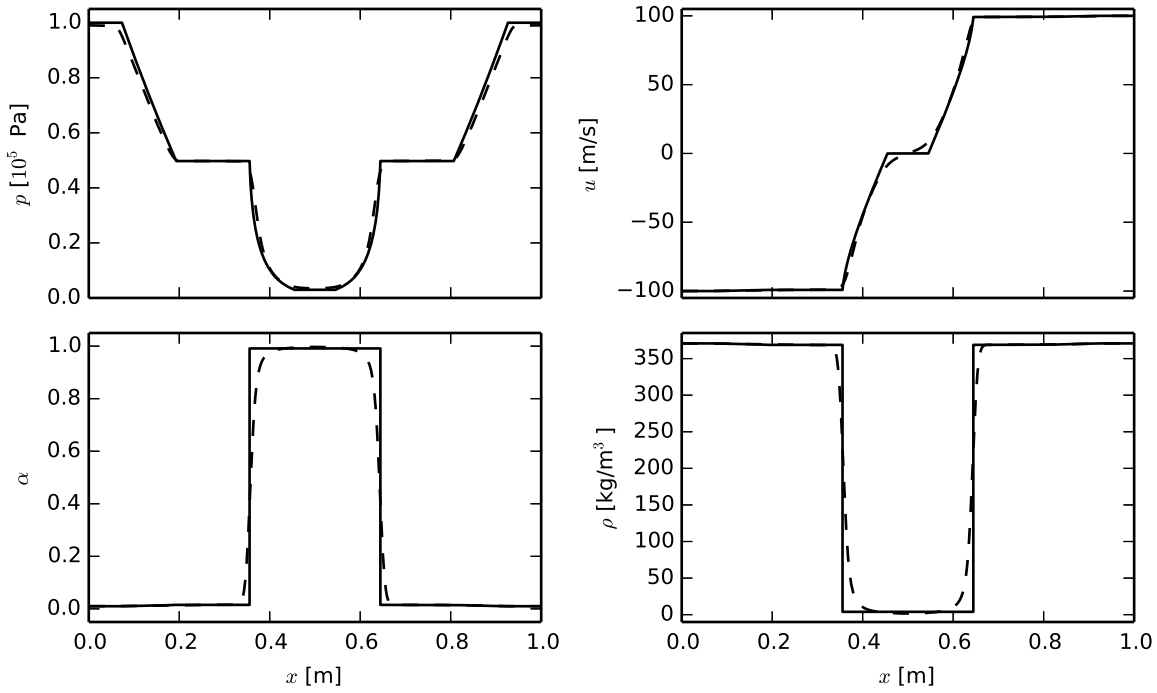

Figure 4.14: Comparison between the analytical two phase solution (solid line) and the numerical solution (dashed line) to the high velocity expansion tube, with thermodynamic relaxation when $T_2 > T_{\text{sat}}(p)$. $t = 1.4\,\text{ms}$

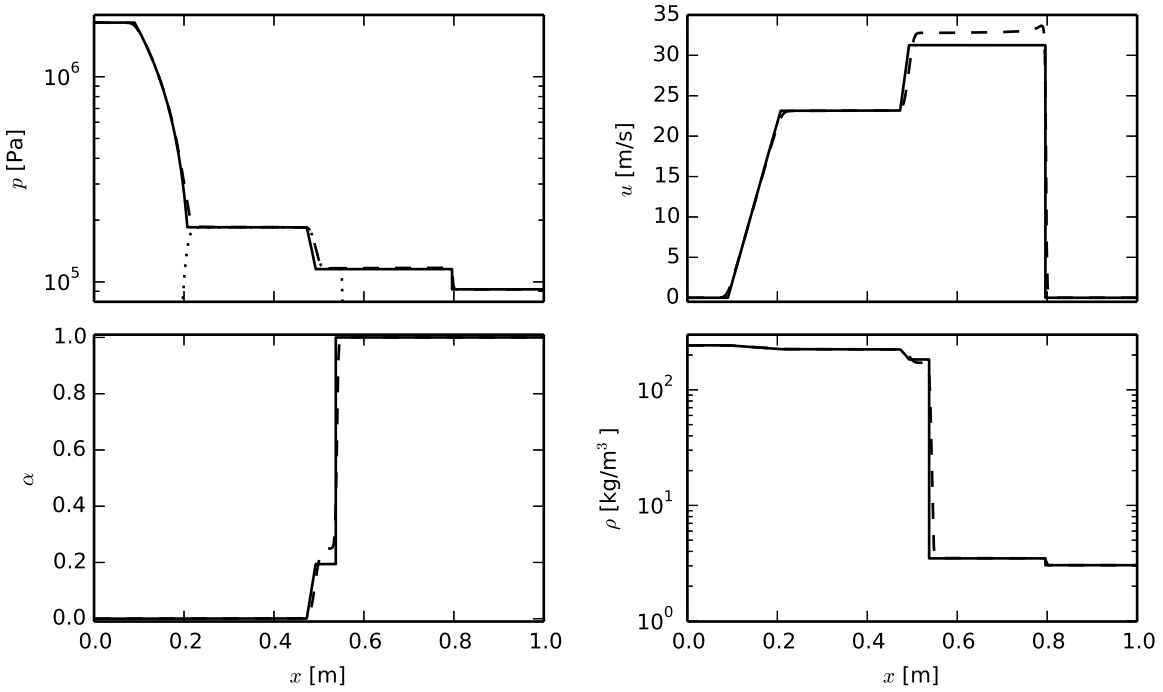

Figure 4.15: Comparison between the semi-analytical solution (solid line) and the numerical solution (dashed line) to the sub-spinodal liquid-vapor shock tube test with only the phase transition required have a valid solution. The dotted line in the pressure plot is the liquid spinodal pressure $p_s(v_2)$. t =1.2 ms

4.3 Grid dependency analysis: The interface criterion

The interface criterion of the stiff thermodynamic relaxation method leads to a grid dependency in the evaporation wave. This is shown using the SG-EOS, but the grid dependency is also present when using the vdW-EOS. Two different cases are shown. In the first, the evaporation wave is stationary in lab-frame, independent of the initial velocity in the flow field. In the second case, the evaporation wave is propagating through the computational grid at a rate of one computational cell per computational time step.

4.3.1 Stationary evaporation wave

A liquid-vapor shock tube was set up. A computational grid of 100 cells spanning 0.1 m ($\Delta x = 1$ mm) were used, with a constant CFL-number set to 0.5. The boundary conditions were set to free flow conditions. The interface volume fraction limit was set to $\xi_I = 10^{-3}$. The following initial conditions were used:

	p	u	α	ρ_1	ρ_2
$x < 0.05$ m	2.0×10^7 Pa	u_0	10^{-6}	3.15 kg/m^3	390.0 kg/m^3
$x \geq 0.05$ m	1.0×10^5 Pa	u_0	$1-10^{-6}$	3.15 kg/m^3	390.0 kg/m^3

Figure 4.17 shows a comparison between tree different calculations at t =10 ms, with u_0 set to 0 m/s, -25 m/s and 25 m/s. The evaporation wave is stagnant with regards to the grid in all three cases. In fact, the evaporation wave front is located at the exact same computational cell through the entire calculation time of 3.2×10^4 time steps. This results in an evaporation wave velocity of 27.2 m/s for $u_0 = 0$ m/s, 6.5 m/s for $u_0 = -25$ m/s and 48.5 m/s for $u_0 = -25$ m/s. The grid dependency shown presently gives reason to question the validity of the recreation of experimental evaporation wave velocities presented

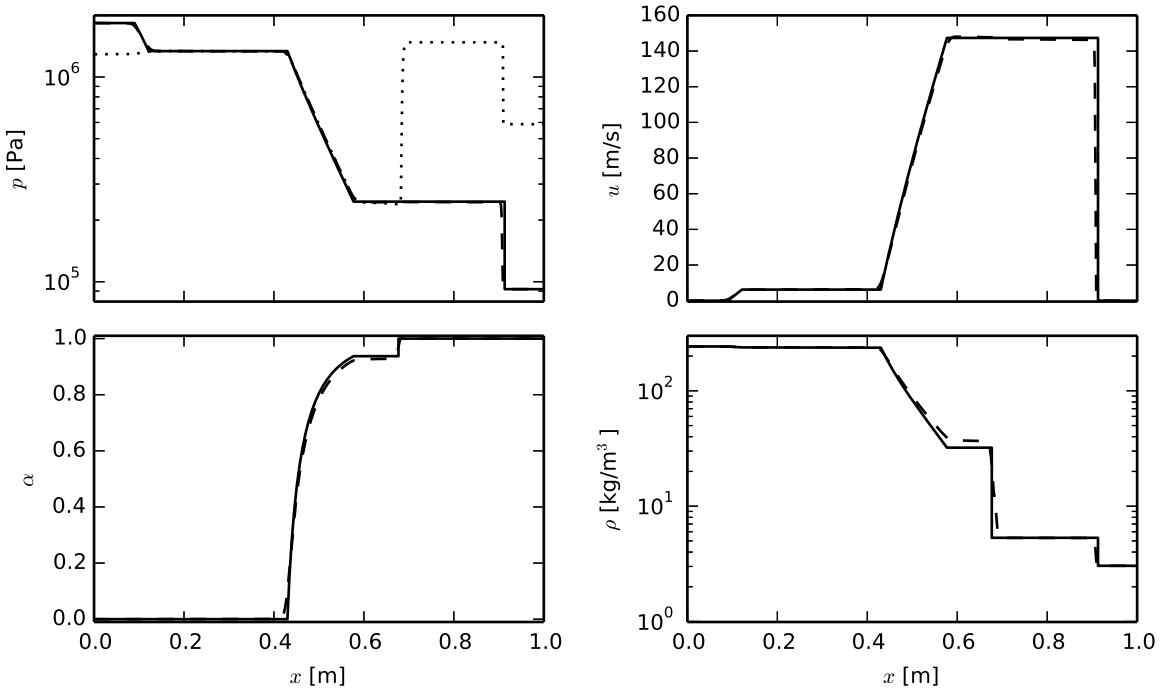

Figure 4.16: Comparison between the analytical solution (solid line) and the numerical solution (dashed line) to the sub-spinodal liquid-vapor shock tube test with thermodynamic relaxation when $T_2 > T_{\text{sat}}(p)$. The dotted line in the pressure plot is the liquid saturation pressure $p_{\text{sat}}(v_2)$. t =1.2 ms

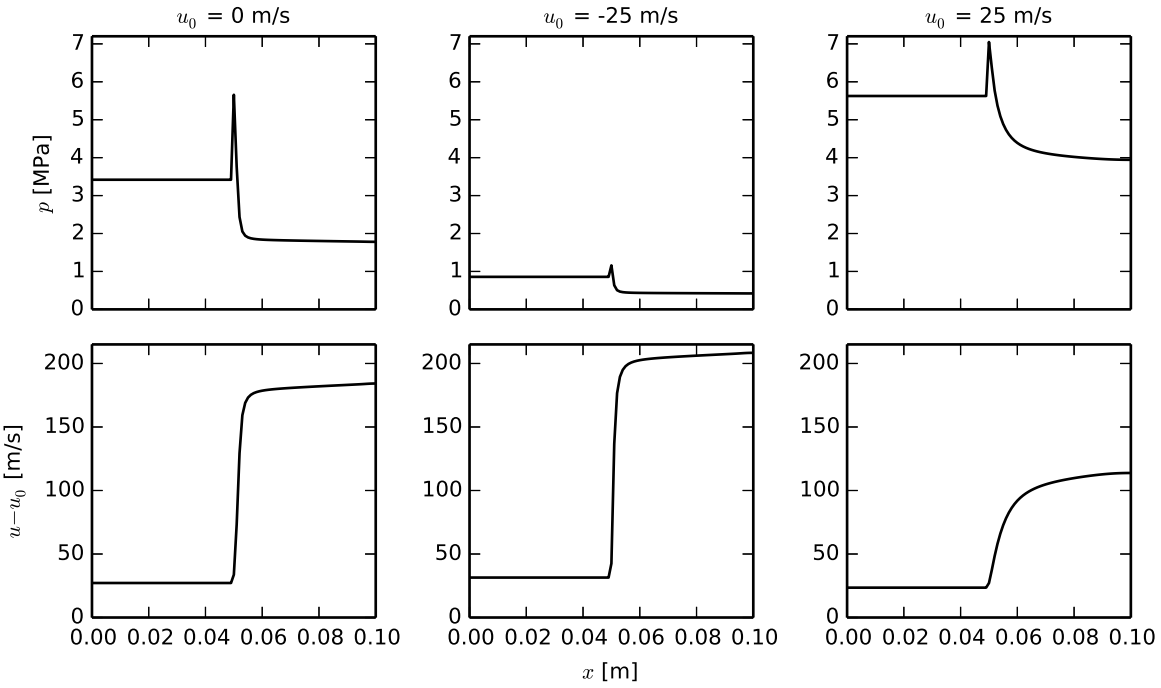

Figure 4.17: Liquid-vapor shock tube with identical initial conditions except from a uniform initial velocity u_0. Solution time t =10 ms.

by both Saurel et al. [4] and Zein et al. [17]. This grid dependency in evaporation wave velocity implies that the interface criterion for stiff thermodynamic relaxation should only be used as a first guess and is useless with regard to any experimental comparison.

4.3.2 Artificial evaporation wave speed

A test case with almost pure liquid with very high level of superheat was set up. A small region was set with vapor volume fraction higher than the interface volume fraction to initiate an evaporation wave. A computational grid of 250 cells spanning 0.25 m ($\Delta x = 1$ mm) were used. The boundary conditions were set to free flow conditions. The interface volume fraction limit was set to $\xi_I = 1.0 \times 10^{-4}$. The following initial conditions were used:

	p	u	α	ρ_1	ρ_2
$x < 0.005$ m	10^5 Pa	0 m/s	10^{-3}	3.07 kg/m^3	374.7 kg/m^3
$x \geq 0.005$ m	10^5 Pa	0 m/s	10^{-6}	3.07 kg/m^3	374.7 kg/m^3

The results of calculations with CFL = 0.5 and CFL = 0.25 are shown in Figure 4.18. In both cases, the evaporation front propagated at a rate of one computational cell per time step. This is clearly an artefact of the evaporation rate model.

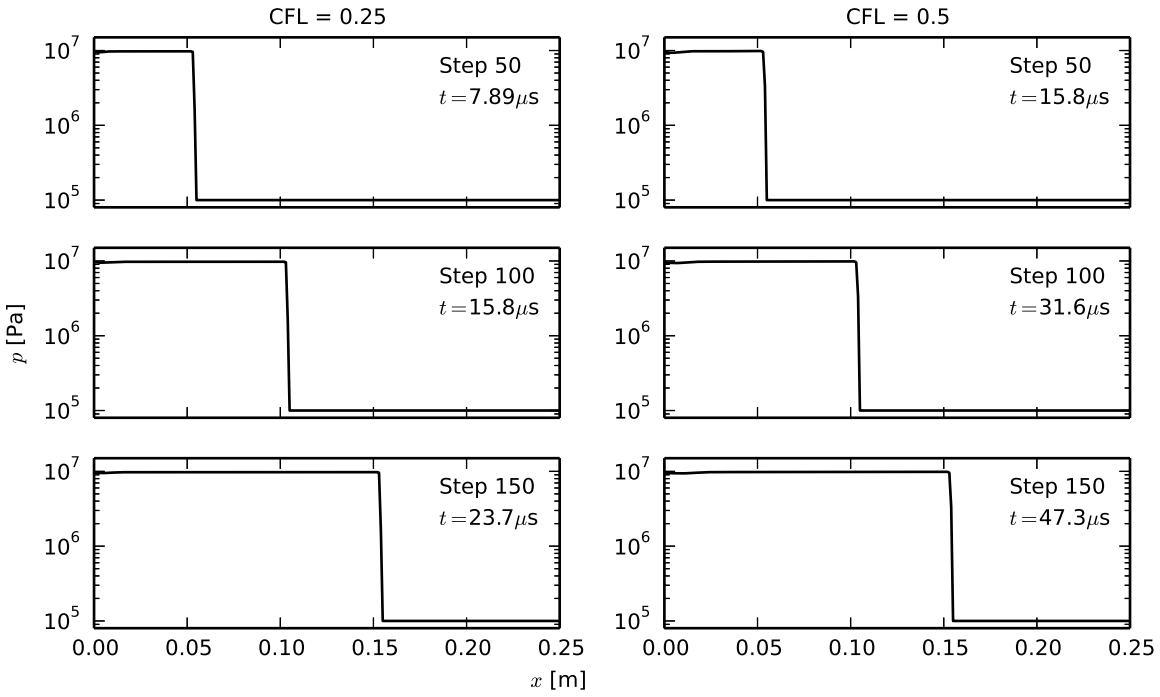

Figure 4.18: Evaporation wave propagating at a rate of one computational cell per time step regardless of the numerical value of the time step.

Chapter 5

Experimental work

Note: The text in this chapter is a direct copy from Tosse et al. [40], provided here for completeness.

In order to understand the thermodynamic and kinetic process of rapid depressurization and evaporation of a liquefied gas, experiments with liquid CO_2 were carried out. The scope of the experimental work was to provide insight into the overall thermodynamics and kinetics that govern the evaporation process in superheated CO_2. Velocities of evaporation waves and contact surfaces as well as pressure readings are important in providing such insight. The results also function as a basic reference for the numerical model, as discussed in Chapter 6.

It is common to use term boiling for the phase transition that takes place when vapor bubbles form within a liquid body or at an interface with a solid body. In the present experimental work, there is often no clear liquid surface or body but rather a mixture of vapor and liquid. The term evaporation waves is described by Simoes-Moreira [41] as *"processes that may occur under certain conditions in which a metastable or superheated liquid undergoes a sudden phase transition in a narrow and observable region [...]."* We use this term when such phenomena are observed and the term boiling for other liquid-gas phase transitions.

5.1 Experimental setup

The experiment was carried out in a vertically oriented clear Lexan tube partly filled with liquid CO_2. A schematic illustration of the tube is provided in Figure 5.1. The visible portion of the tube was 32 cm in length. The inner-diameter of the tube was 9 mm and the outer-diameter was 12 mm. One end of the tube was a membrane which was punctured by a needle. Two layers of Mylar sheet were used as the membrane material. The experiment was photographed using a high-speed camera (Photron APX-RS) at 16,000 frames per second (64 x 1024 pixels), which allowed visual tracking of the various fronts and bulk boiling. The tube was illuminated from the front by white light. Some experiments were done using back lighting, but the light was not able to penetrate the two-phase region. In addition to the high speed camera, two Kulite XT-190 pressure transducers (P_1 and P_2 in Figure 5.1) were used to record the pressure inside the tube. The distance between the two pressure transducers was 43.5 cm. The first series of experiments were conducted with the membrane placed at the top of the tube. The vertical orientation of the tube was reversed in the second series, so that the membrane was at the bottom.

The tube was filled through an inlet valve at the bottom of the tube using liquid CO_2 from a gas bottle with a riser tube. Careful pressure relief at the top of the tube allowed the liquid CO_2 to fill the tube to the desired level. When the fill (1) and relief (2) valves shown in Figure 5.1 were closed, the thermodynamic state inside the tube was assumed to be equilibrium between the liquid an vapor.

5.2 Experimental results and discussion

The experimental results are provided for two cases. In the first case, the membrane was placed at the top of the tube so that the vapor head space was directly below the membrane. In the second case, the vertical orientation of the tube was reversed so that liquid was located directly above the membrane. The high-speed images are displayed as a series of isochronously spaced images, which allows the fronts to

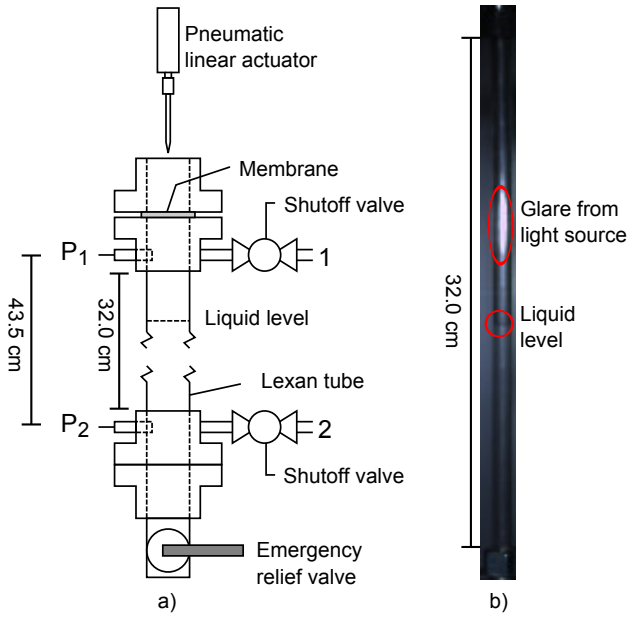

Figure 5.1: (a) Schematic illustration of the shock tube with vapor side penetration (not to scale). The tube was filled at the inlet (2), while (1) was used for controlled pressure relief to allow liquid CO_2 to fill the tube. P_1 and P_2 are pressure transducers. The distance from P_1 to P_2 was 43.5 cm, and the transparent part of the tube was 32.0 cm in length. (b) Example high speed shot of the tube filled with liquid CO_2. This is the total field of view of the camera. Note that the length of 32.0 cm indicated in both (a) and (b) is the part of the tube that is shown in the photographs in the result section.

be easily tracked. The front velocities are found by polynomial curve fitting of the front position versus time. All images are cropped to show only the visible portion of the tube, with a height of 32.0 cm. The pixel width was 0.35 mm/px. Visual tracking of fronts is possible, but as the front position is not always clear, some uncertainty in the calculated velocities should be expected. The uncertainties were estimated by varying the gradient of the velocity to fit within the front region. Due to the curvature of the tube and the lack of magnification, it was not possible to observe the evaporation front structure.

5.2.1 Vapor side membrane placement

Figure 5.2 shows the experimental results when the shock tube is filled with liquid CO_2 up to 45% of the height between P_1 and P_2. The pressure time histories in Figure 5.2 show a 1.83 ± 0.09 ms delay between the first pressure drop i the upper and the lower pressure transducer. This corresponds to a mean speed of sound of 238 ± 12 m/s. As a reference, at 5.5 MPa saturated conditions and a liquid fill level of 45%, the Span-Wagner equation of state [2] gives a mean speed of sound of 248 m/s (198.0 m/s in the vapor and 356.8 m/s in the liquid phase). The Span-Wagner speed of sound of each phase has been plotted as the dashed red line in Figure 5.2 to illustrate the predicted path of the first rarefaction wave.

From the pressure drop at P_1, there is a time delay of 0.8 ms until any visual changes occur in the tube. Some of this delay can be explained by the 5.75 cm gap between the pressure transducer and the upper end of the visible portion of the tube, but it is likely that the pressure in the tube drops prior to the appearance of the changes. This implies that the vapor becomes sub-cooled prior to the visual changes. As a reference, isentropic expansion of vapor from the known initial conditions to 3.5 MPa using the Span-Wagner equation of state yields a sub-cooled vapor temperature of 262 K. Since this is well above the triple point temperature of CO_2 (216.6 K), it is safe to assume that the white front that propagates downwards into the vapor from t = 72 ms (line A in Figure 5.2) consists of condensed droplets and not solid particles.

At 1.4 ms after the initial pressure drop at P_1, the liquid starts to boil at the interface. The boiling

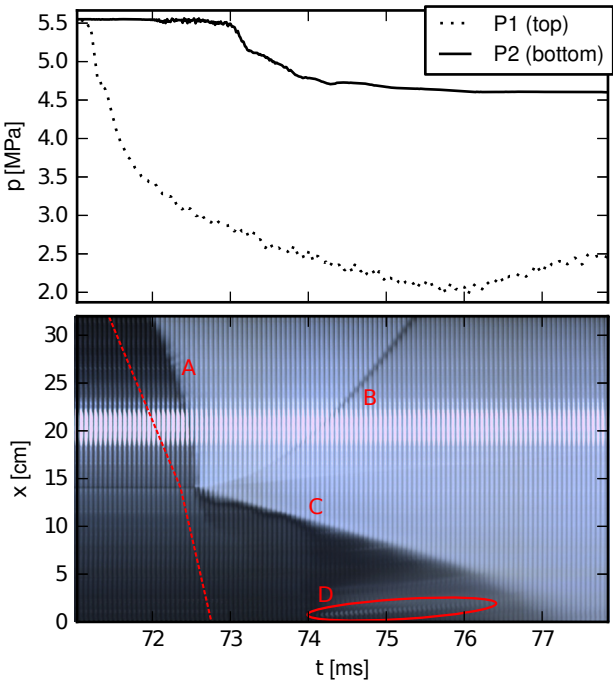

Figure 5.2: Experimental results with vapor side membrane penetration. P_1 and P_2 refers to Figure 5.1 (a). The time-scale is relative to the trigger mechanism of the membrane penetration device. The red dotted line is the trajectory of the first rarefaction wave travelling at the speed of sound as given by the Span-Wagner equation of state. (A) Condensation wave. (B) Vapor-mixture interface. (C) Evaporation wave. (D) Bubbles in liquid

propagates as a front into the liquid (line C in Figure 5.2). At the same time, a front is seen accelerating upward into the vapor phase (line B in Figure 5.2). This is most likely the contact surface between the the vapor and the liquid-vapor mixture that is produced by the boiling liquid. The evaporation front and the contact surface are plotted in Figure 5.4. The evaporation front is fitted with a constant velocity of 25 ± 1 m/s and the contact surface is fitted with a constant acceleration of 40.8 ± 0.5 km/s^2. These fronts are well known phenomena in the context of evaporation waves, and are described among others by Pinhasi et al. [23]. The pressure at the top of the tube increases slightly after the contact surface passes, up to a level of 2.6 MPa. Using the Span-Wagner equation of state, the isentrop from the initial 5.5 MPa at saturated conditions intersects the spinodal curve at 3.0 MPa as shown in Figure 5.3. While it is impossible to determine the exact pressure in the liquid-vapor mixture zone with the current experimental setup, it is possible that it is on the same order as the top pressure after the contact surface passes. If this is the case, the evaporation front could be close to a spinodal decomposition wave. It should also be noted that the increase in pressure following the exit of the contact surface could be the result of changed choking conditions at the tube exit. When the two phase mixture is subject to the sudden pressure drop at the tube exit, some of the liquid will evaporate.

After t = 74 ms, the liquid appears to be boiling at the bottom of the tube (region D in Figure 5.2). At this point, P_2 is stabilized at roughly 4.6 MPa. The pressure is most likely stabilized because of the boiling process in the liquid. The boiling appears to be non-homogeneous so it is most likely caused by impurities at the wall or at the tube end. Some structures are observed moving upwards. In Figure 5.4, these structures are fitted to a constant velocity of 6.0 ± 0.5 m/s. This may be an indication of bulk fluid velocity.

5.2.2 Liquid side membrane placement

In these experiments, the membrane was placed at the bottom of the tube. Figure 5.5 shows the experimental results with the tube filled with liquid CO_2 up to the top of the visible portion. The

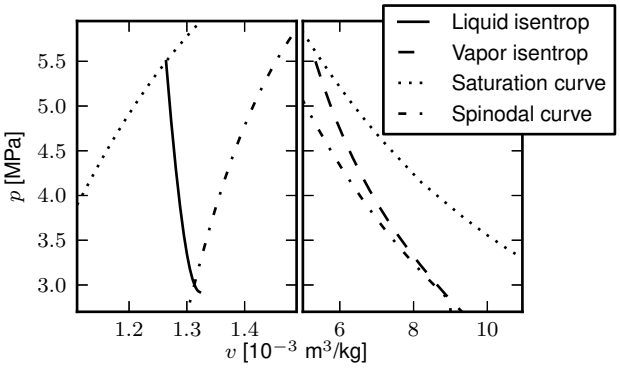

Figure 5.3: Isentropic expansion from the initial conditions of saturation at 5.5 MPa in p-v space (Span-Wagner equation of state). The liquid isentrop intersects the spinodal curve at 3.0 MPa. The spinodal curve is defined by $\left(\frac{\partial p}{\partial v}\right)_T = 0$

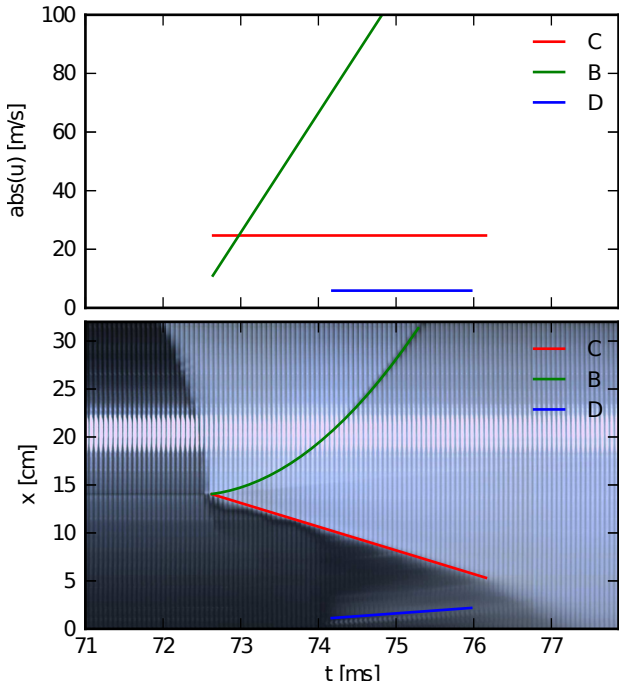

Figure 5.4: Curve fittings of front positions and velocities from Figure 5.2 plotted with time. (C) Evaporation wave. (B) Vapor-mixture interface. (D) Bubbles in liquid.

dashed red line in the figure is the predicted path of the first rarefaction wave based on the Span-Wagner speed of sound. At 2.0 ms after the first drop in P_1, the first sign of boiling appears. It is interesting to note that the boiling appears to be initiated at the liquid-vapor interface at the top even though the membrane is located at the bottom of the tube. The liquid also boils at the membrane side, but the velocity of liquid flowing out of the tube is greater than that of the boiling, so the lower evaporation wave is never visible. The liquid-vapor interface is accelerating downward (line A in Figure 5.5). The white area at the interface is expanding from barely visible at t = 68 ms to 1 cm in height at t = 72 ms. The white area could be liquid boiling at a low rate. At t = 75.5 ms the vapor phase becomes opaque (line B in Figure 5.5). This is assumed to be caused by a condensation process in the sub-cooled vapor like in the previous setup. The condensation appears to be initiated at the liquid-vapor interface and propagate upward into the vapor for some time before the rest of the vapor condensates simultaneously. The liquid-vapor interface continues downward, but appears to decelerate (region C in Figure 5.5). Around t = 72 ms, a new front appears (region D in Figure 5.5) and accelerates downward into the liquid.

The accelerating front is most likely an evaporation wave similar to the one observed in the first series of experiments. Region C is then possibly a mixture-vapor contact surface. The difference is that in the first series, the liquid flow velocity was in the opposite direction of the evaporation wave. Here, the liquid phase is flowing out of the tube at an unknown, possibly increasing flow velocity. Figure 5.6 shows curve fittings of the liquid-vapor interface and the evaporation wave.

With careful consideration of Figure 5.5, one can observe some white streaks in the liquid phase (region E in Figure 5.5), corresponding to a velocity on the order of 20 m/s (line E in Figure 5.6). Note that these streaks are barely visible. They are most likely small structures (bubbles) in the liquid that act as tracers from which the liquid velocity can be inferred, but the nature of the observations makes further investigations necessary to confirm this.

Between t = 68 ms and t = 70 ms, there is an increase in the bottom pressure as well as a distinct change in brightness in the liquid (region F in Figure 5.5). The change appear to be homogeneous. This may be an indication of homogeneous nucleation.

Due to various reasons, only one complete data set exists for the setup with the membrane placed at the bottom of the tube. This implies that the repeatability of the results presented in this section is unknown and that these results may be unique.

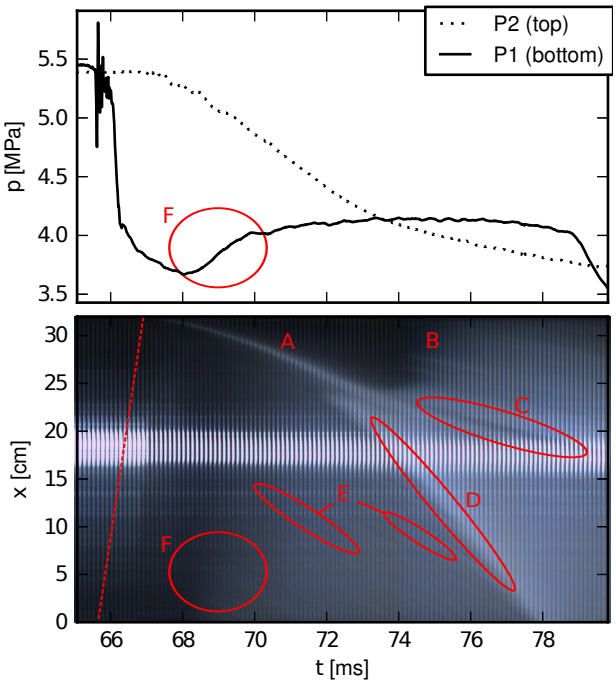

Figure 5.5: Experimental results with liquid side membrane penetration. P_1 and P_2 refers to Figure 5.1 (a). The time-scale is relative to the trigger mechanism of the membrane penetration device. The red dotted line is the trajectory of the first rarefaction wave travelling at the speed of sound as given by the Span-Wagner equation of state. (A) Liquid-vapor interface. (B) Condensation wave. (C) Vapor-mixture interface. (D) Evaporation wave. (E) Bubbles in liquid. (F) Homogeneous boiling

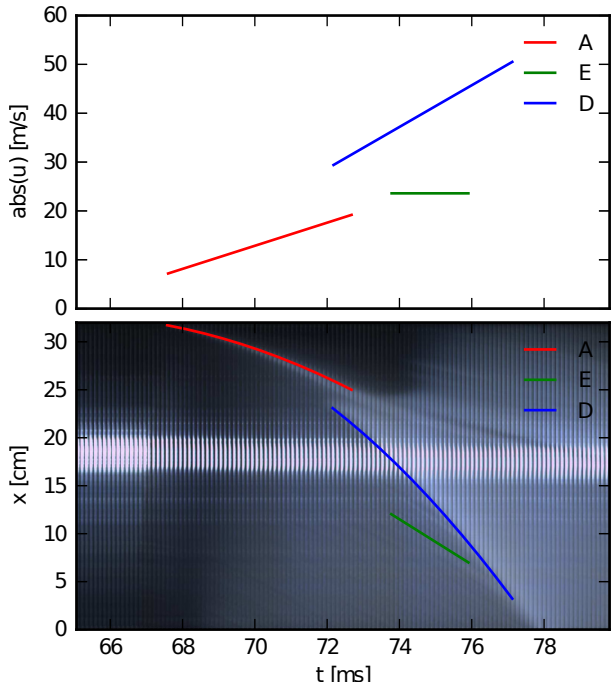

Figure 5.6: Curve fittings of front positions and velocities from Figure 5.5 plotted with time. (A) Liquid vapor interface. (E) Bubbles in liquid. (D) Evaporation wave.

Chapter 6

Numerical experiment comparison

Two numerical tests were carried out to compare with the experimental results in sections 5.2.1 and 5.2.2. A high pressure section spanning 0.5 m and a low pressure section spanning 0.2 m was used, so that the total computational domain spanned 0.7 m. A total of 7000 cells were used with a uniform cell width of 10^{-4} m. Stiff thermodynamic relaxation was used at the interface, with an interface limit of $\xi = 10^{-4}$. The vdW representation of CO_2 was used. At the high pressure boundary ($x = 0$ m), wall boundary conditions were used. At the low pressure boundary ($x = 0.7$ m), free flow boundary conditions were used. The free flow boundary conditions at the low pressure outlet were chosen to minimize the effect of the boundary on the flow in the computational area. The effect of different boundary conditions should be investigated, as a boundary condition with relaxation to atmospheric conditions would be more accurate. However, this is outside the scope of the present work.

6.1 Vapor side membrane placement

The calculation was run with an initial CFL number set to 0.2 for the first 200 time steps. The CFL number was then linearly increased to 0.5 over 50 time steps and was set to 0.5 for the rest of the calculation. The following initial conditions were used:

	p [Pa]	u [m/s]	α	ρ_1 [kg/m^3]	ρ_2 [kg/m^3]
$x < 0.25$ m	5.5×10^6	0	10^{-6}	175.00	530.45
0.25 m $\geq x < 0.5$ m	5.5×10^6	0	1-10^{-6}	175.00	565.46
$x \geq 0.5$ m	1.0×10^5	0	1-10^{-6}	1.8794	565.46

Figure 6.1 shows the initial rarefaction wave propagating into the vapor. Since the volume fraction is above the interphase limit, no thermodynamic relaxation takes place, and the vapor becomes sub-cooled. When the rarefaction wave crosses the vapor-liquid contact surface, a condensation wave is initiated (Figure 6.2), propagating away from the contact surface at a lab-frame velocity of 1050 m/s. However, the condensation wave is propagating at exactly one computational cell per time-step, so this velocity is a numerical artefact and should be regarded as arbitrary, caused by the ill-posedness of the interface-criterion for thermodynamic relaxation. In the experiments, the condensation wave was initiated at the membrane, propagating towards the contact surface.

The initial rarefaction wave continues to propagate into the liquid, and the liquid becomes highly superheated, as shown in Figure 6.3. An evaporation wave is created at the vapor-liquid interface, creating a vapor-liquid mixture and a mixture-vapor contact surface. The evaporation wave is stationary in lab-frame which translates to a propagation velocity on the order of 12 m/s relative to the superheated liquid. The mixture-vapor contact surface follows the bulk fluid flow, and is accelerating at a rate on the order of 30 to 50 km/s^2.

The bulk liquid flow away from the wall causes a pressure drop at the wall. When the pressure reaches the spinodal, the spinodal evaporation causes the vapor volume fraction to cross the interface treshold, and a right-propagating evaporation wave is initiated (Figure 6.4). In the experiments, evaporation in the liquid body prevents the liquid from becoming highly superheated. The evaporation wave initiated

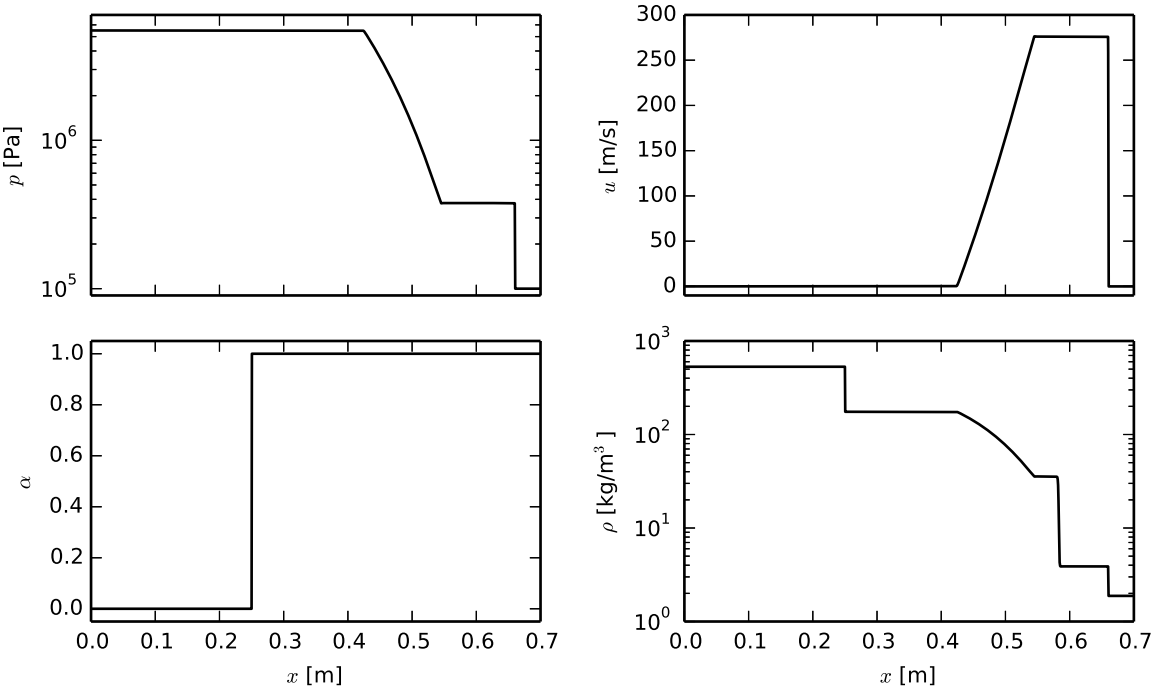

Figure 6.1: The first rarefaction wave propagating into the high pressure vapor. t =0.30 ms

at the wall can therefore be regarded as a numerical artefact. The evaporation wave is propagating at a lab-frame velocity of ∼1360 m/s, but just as the initial condensation wave, it propagates at exactly one computational cell per time-step, so this velocity should also be regarded as arbitrary. When the right-propagating evaporation wave reaches the left-propagating evaporation wave, a shock wave is created, propagating into the vapor-liquid mixture (Figure 6.5). The left-propagating evaporation wave is then propagating into the liquid dominant mixture at lab-frame velocity on the order of 70 m/s (80 m/s relative to the upstream liquid-dominant mixture). This evaporation wave expands spatially as it propagates.

A pressure-time plot can be found in Figure 6.6. When compared to the experimental pressure-readings in Figure 5.2, there are two distinct differences. The jump in pressure at $x = 0.45$ m at $t \approx 1.2$ s in the calculations is caused by the condensation wave being initiated at the interface, and is not present in the experiments. The large drop and sharp rise in the liquid pressure at $t \approx 1.5$ s to $t \approx 2.3$ s is also not present in the experiments. This makes it clear that there is some evaporation in the liquid body in the experiment, contributing to maintaining a high pressure. This is in fact observed (region D in Figure 5.2).

6.2 Liquid side membrane placement

A constant CFL number of 0.5 was used in the calculation. The following initial conditions were used:

	p [Pa]	u [m/s]	α	ρ_1 [kg/m^3]	ρ_2 [kg/m^3]
$x < 0.15$ m	5.5×10^6	0	1-10^{-6}	175.00	565.46
0.15 m $\geq x < 0.5$ m	5.5×10^6	0	10^{-6}	175.00	530.45
$x \geq 0.5$ m	1.0×10^5	0	1-10^{-6}	1.8794	565.46

Figure 6.7 shows the first rarefaction wave propagating into the high pressure liquid, the evaporation wave at the liquid-vapor interface and the shock propagating into the low pressure vapor. Like in the previous setup, the evaporation wave is stationary in lab-frame. This translates to a velocity of 17.6 m/s

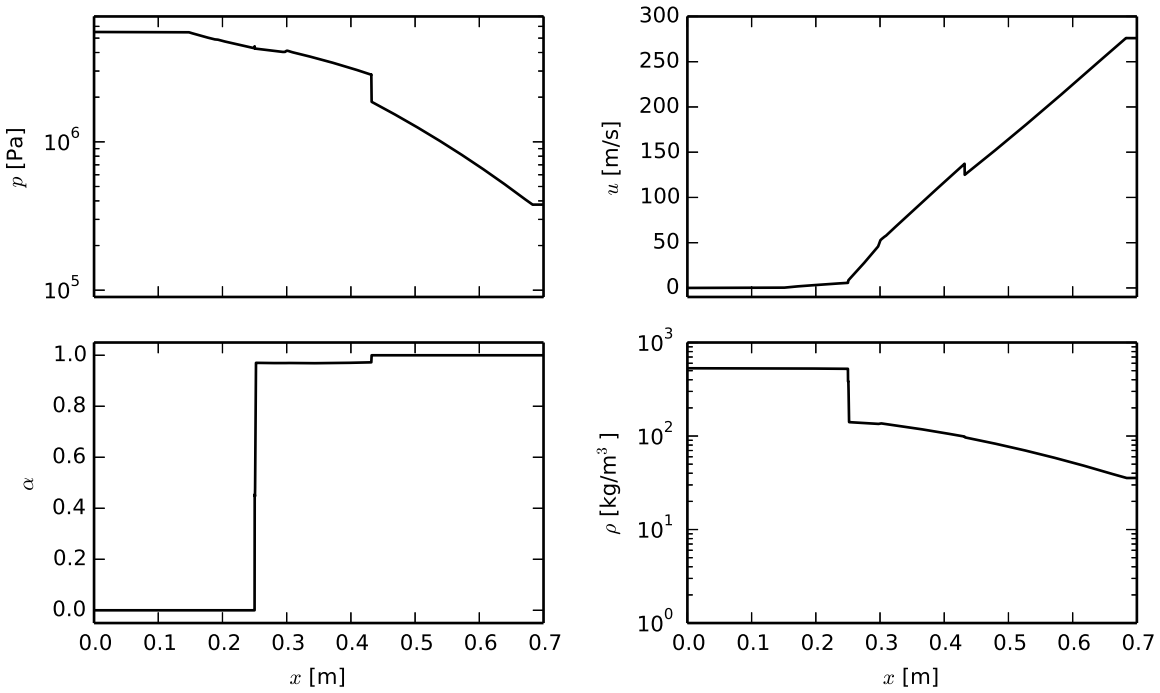

Figure 6.2: Condensation wave initiated at the liquid-vapor contact surface. t =1.23 ms

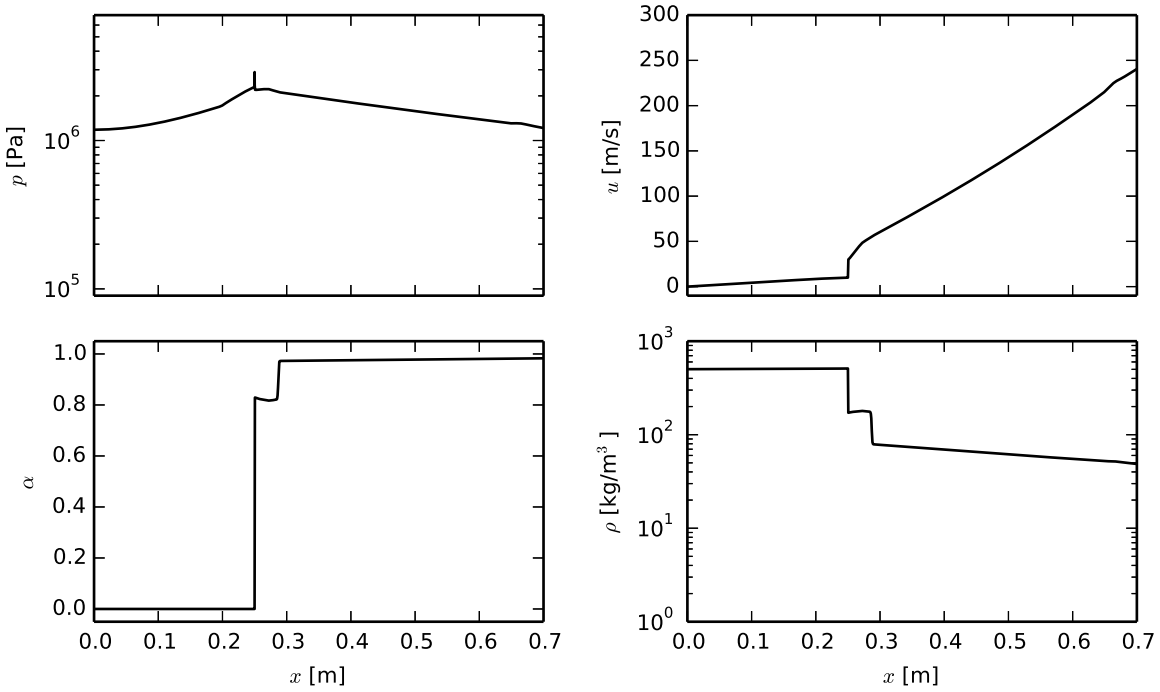

Figure 6.3: Evaporation wave and contact surface. t =2.34 ms

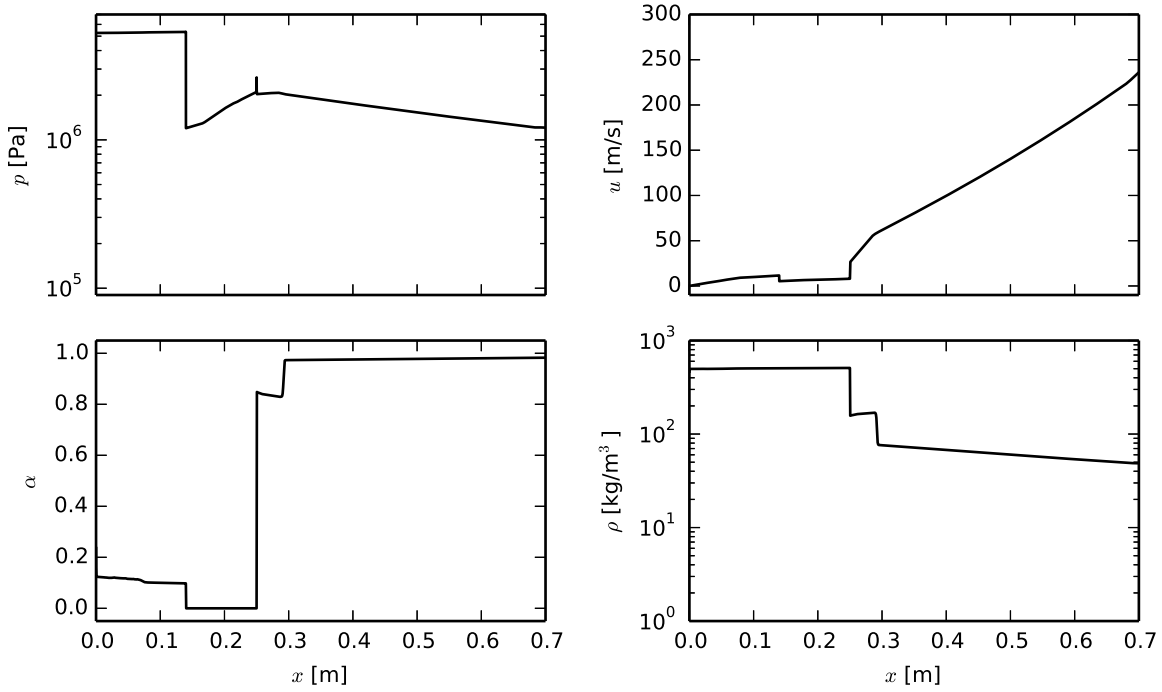

Figure 6.4: Evaporation wave initiated by spinodal evaporation at the wall. t =2.42 ms

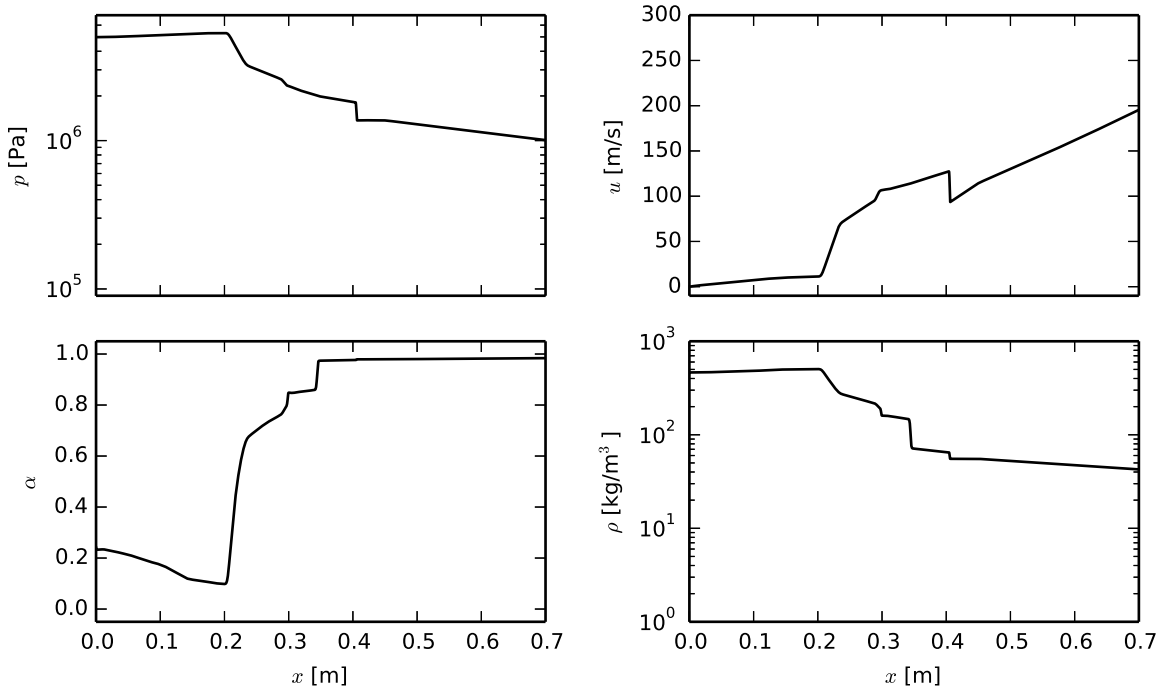

Figure 6.5: Evaporation wave travelling into the liquid dominant mixture, contact surface, shock wave travelling into the vapor. t =3.06 ms

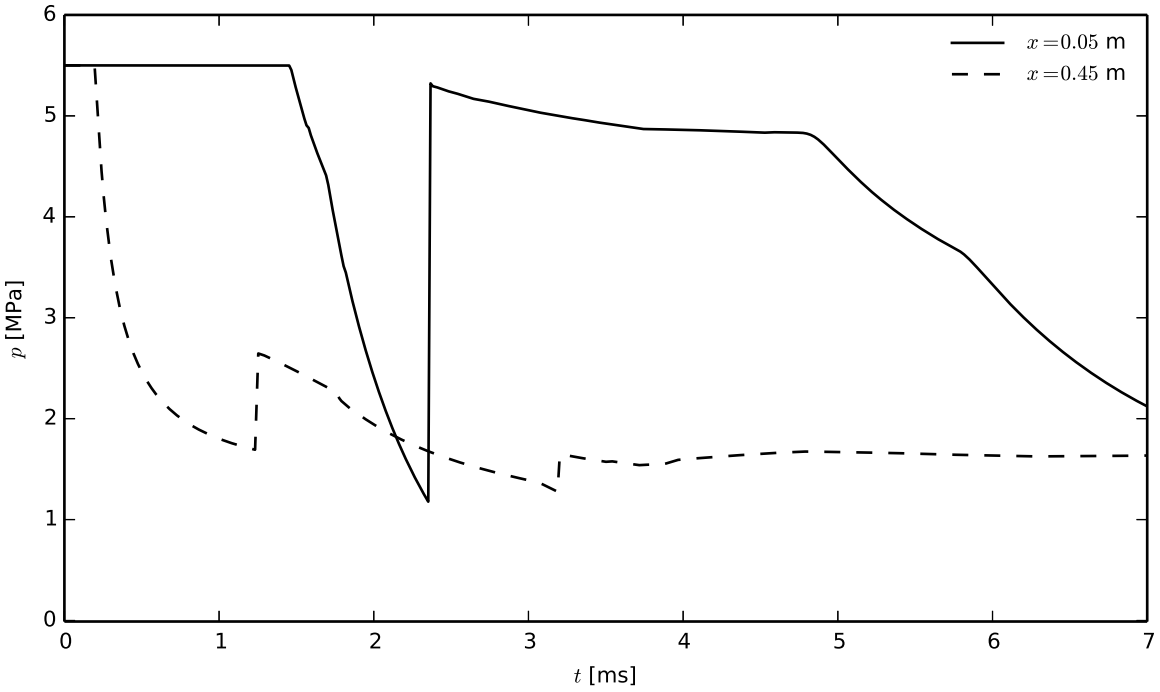

Figure 6.6: Pressure-time plot for $x = 0.05\,\mathrm{m}$ and $x = 0.45\,\mathrm{m}$ (vapor side membrane placement)

relative to the upstream liquid. Again, this velocity is a result of the interface-criterion and should be regarded as arbitrary.

When the initial rarefaction wave reaches the high pressure liquid/vapor interface at $x = 0.15\,\mathrm{m}$, a shock wave is reflected as shown in Figure 6.8. The shock wave is propagating at a lab-frame velocity on the order of 420 m/s. An evaporation wave is also initiated at the liquid-vapor interface. It is propagating into the high-pressure liquid at a lab-frame velocity of 120 m/s, which corresponds to a velocity of 85 m/s relative to the liquid in front of the evaporation wave.

Figure 6.9 shows the shock wave propagating into the accelerating vapor dominated mixture at $x > 0.5\,\mathrm{m}$. The shock wave is accelerating in lab-frame, but has a near constant velocity on the order of 165 m/s relative to the mixture in front of the wave. The shock wave is reflected at the interface at $x = 0.5\,\mathrm{m}$, and a rarefaction wave is propagating left into the liquid at a lab frame velocity on the order of 380 m/s. This corresponds to a velocity of 415 m/s relative to the liquid in front of the rarefaction wave. A shock is reflected as the left-propagating rarefaction wave crosses the right-propagating evaporation wave. This is not shown in a figure.

In Figure 6.10, a left-propagating condensation wave and a right propagating evaporation wave is present at $x \approx 0.3\,\mathrm{m}$. The left-propagating condensation wave has a lab-frame velocity of 75 m/s. This corresponds to a velocity of 93 m/s relative to the mixture in front of the condensation wave. The right propagating evaporation wave has an unchanged velocity of 85 m/s relative to the liquid in front of the evaporation wave, which corresponds to a lab-frame velocity of 130 m/s.

A pressure-time plot of the calculation can be found in Figure 6.11. When compared to Figure 5.5, it becomes clear that the pressure at $x = 0.45\,\mathrm{m}$ is not a good representation of the experimental results. This can be attributed to the poor modelling of the liquid evaporation rate in the calculation, in addition to the fact that more realistic boundary conditions should be used at the outlet.

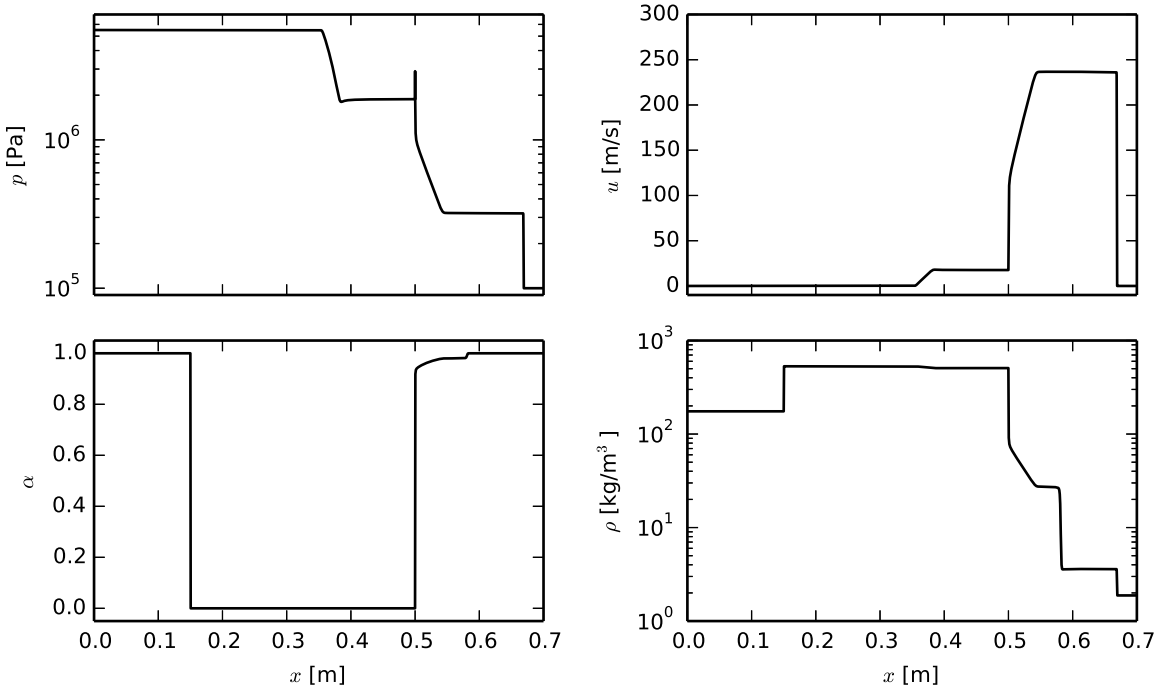

Figure 6.7: Rarefaction wave propagating into the liquid, evaporation wave at interface and shock wave in vapor. t =0.34 ms

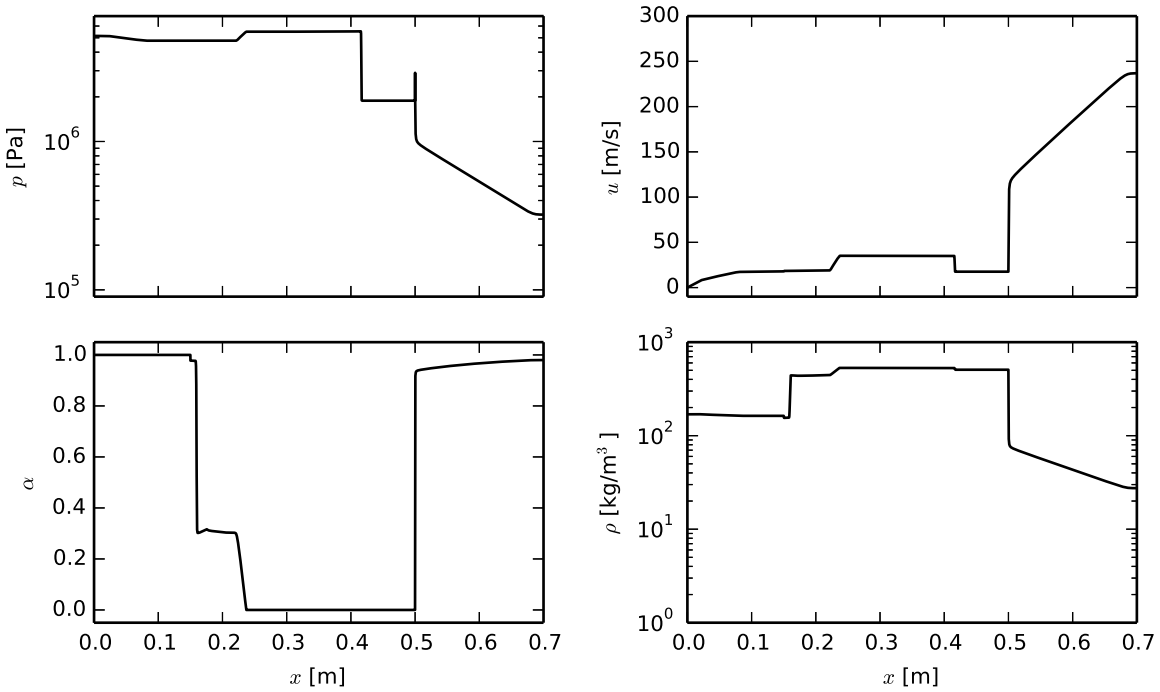

Figure 6.8: Right-propagating evaporation wave and left-propagating shock wave. t =1.50 ms

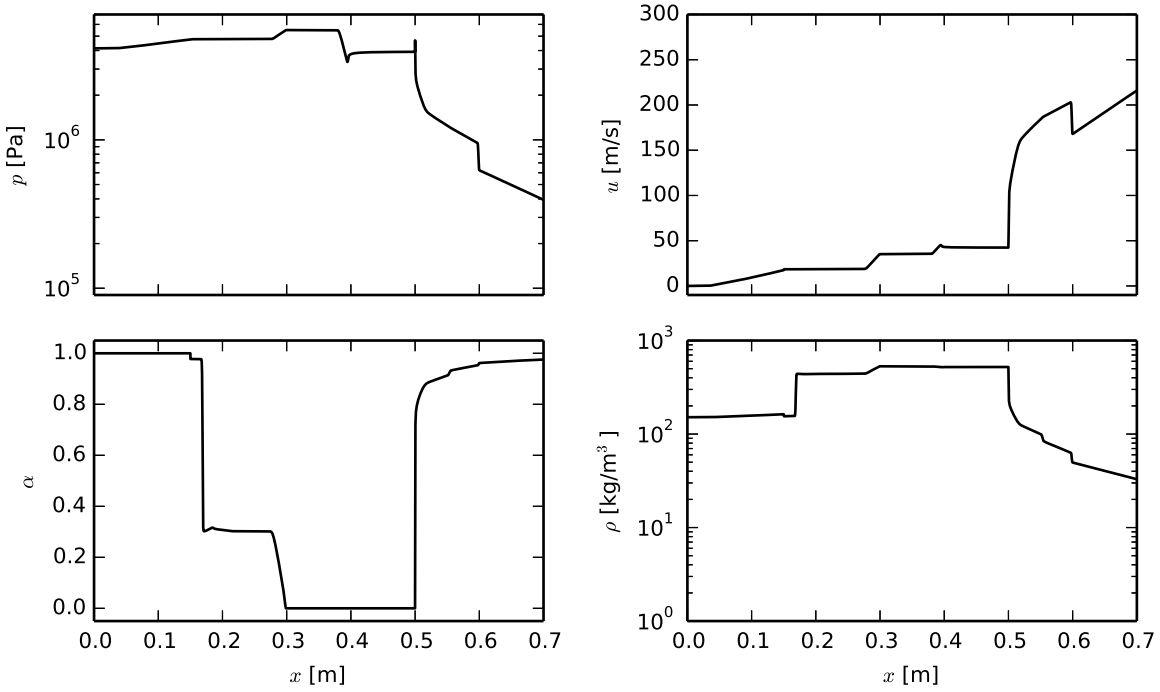

Figure 6.9: Transmitted shock in vapor-dominant and left-propagating reflected rarefaction wave. t =2.00 ms

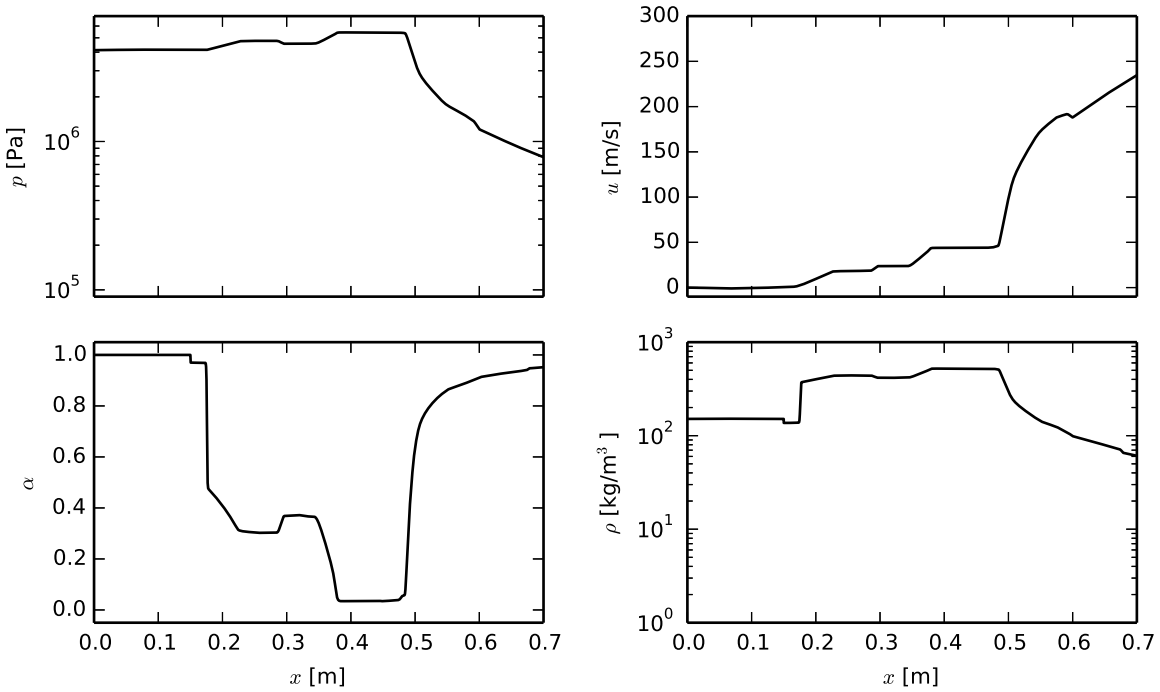

Figure 6.10: Left-propagating condensation and right-propagating evaporation. t =2.60 ms

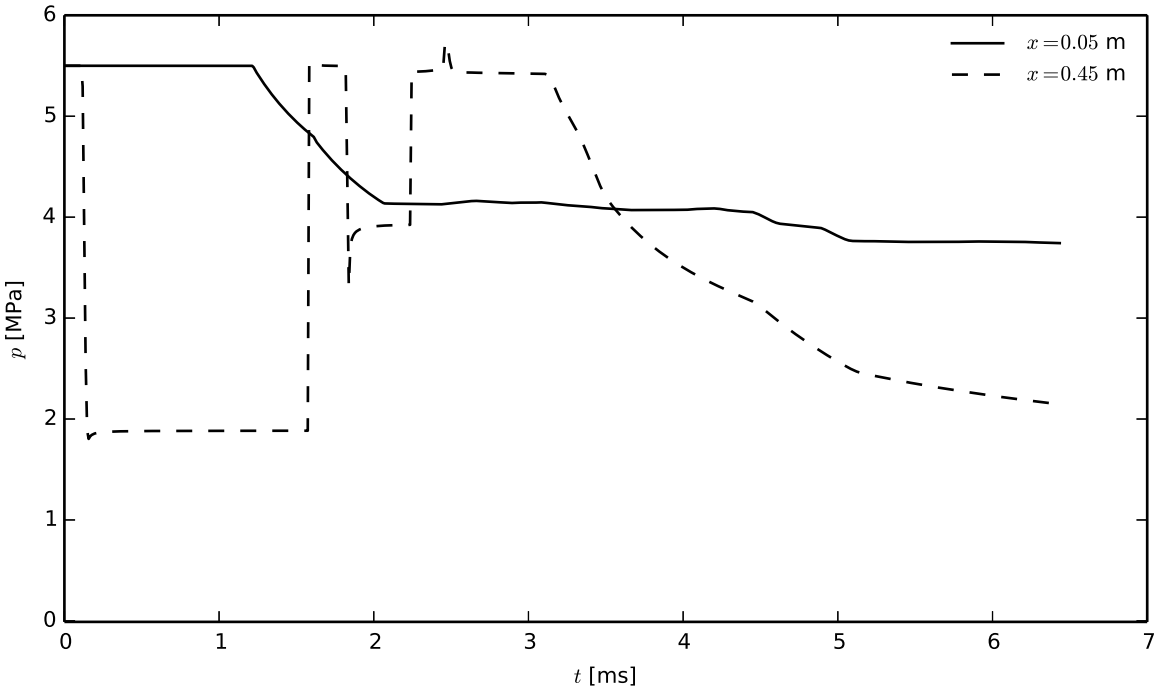

Figure 6.11: Pressure-time plot for $x = 0.05\,\mathrm{m}$ and $x = 0.45\,\mathrm{m}$ (liquid side membrane placement)

Chapter 7

Conclusion

A 1-d numerical solver for two-phase metastable flow governed by a the van der Waals equation of state was developed. Existing algorithms for the stiffened gas equation of state were modified and adapted to be used with a cubic equation of state. The procedures for thermodynamic relaxation were modified to account for sub-spinodal states, while ensuring the conservation of total mass and energy.

The present version of the numerical solver shows methods to deal with the numerical difficulties that arise when dealing with cubic equations of state. It should be regarded as a proof of concept, as there is significant potential for optimization of the solving algorithm. The development has illustrated the complexity of dealing with a cubic equation of state in numerical solvers. Even an equation of state as simple in formulation as the van der Waals EOS makes it impractical or impossible to use analytical expressions in most thermodynamic calculations. Iterative solvers are therefore a vital part of the solving algorithm. Such solvers are not only computationally expensive, they are also sources of instability and inaccuracy in the calculations. With more realistic equations of state, the need for robust and effective iterative solvers are obvious.

The modelling of evaporation rate in the present work is not optimal. The assumption of zero thermodynamic relaxation in pure phases and infinite relaxation at the interface leads to a strong grid dependency and a number of non-physical effects. Further work is needed to develop a finite evaporation rate model capable of handling metastability. Extensive experimental work is needed to validate such a model. Due to the present numerical model, the evaporation rate can be calculated independently of the flow.

It is clear that an extension of the present numerical model to a more realistic equation of state will require a significant amount of work. Such an extension will yield a very computationally expensive solving algorithm. A natural next step would be to implement an EOS agnostic relaxation algorithm based on multivariate gradient descent. It would possibly be beneficial to use a less computationally expensive predictor algorithm to ensure reasonable initial conditions for the relaxation procedure. Such a predictor algorithm can be found by using supervised machine learning procedures. The current algorithm can serve as a benchmark for validation purposes.

Appendix A

Constants

The following constants were used in all calculations if not otherwise is explicitly expressed:

- $R_M = 8.3145$ J/mol K

A.1 Stiffened gas parameters

The following constants was used in the stiffened gas EOS:
Water liquid and vapor:

	p_∞ [Pa]	c_v [J/(kg K)]	γ	q [J/kg]	q' [J/(kg K)]
Water liquid	10^9	1.816×10^3	2.35	-1167.0×10^3	0
Water vapor	0	1.04×10^3	1.43	2030.0×10^3	$-23\,368$

Dodecane liquid and vapor:

	p_∞ [Pa]	c_v [J/(kg K)]	γ	q [J/kg]	q' [J/(kg K)]
Dodecane liquid	4.0×10^8	1077.7	2.35	-755.269×10^3	0
Dodecane vapor	0	1956.45	1.025	-237.547×10^3	-2.441×10^4

Water and air:

	p_∞ [Pa]	c_v [J/(kg K)]	γ	q [J/kg]	q' [J/(kg K)]
Water	6.0×10^8	969.77	4.4	0	0
Air	0	722.86	1.4	0	0

A.2 Van der Waals parameters

The following constants was used in the van der Waals EOS:

	p_c [Pa]	T_c [K]	R [J/(kg K)]
Dodecane	1.835×10^6	659	48.812
Carbon dioxide	7.39×10^6	304.12	188.965

A.3 Gauss-Legendre coefficients

k	ξ_k	ω_k
1	-0.93246951420315202781230160	0.17132449237917034504029610
2	-0.66120938646626451366139960	0.36076157304813860756983350
3	-0.23861918608319690863050170	0.46791393457269104738987030
4	0.23861918608319690863050170	0.46791393457269104738987030
5	0.66120938646626451366139960	0.36076157304813860756983350
6	0.93246951420315202781230160	0.17132449237917034504029610

Appendix B

Algorithms

B.1 Main algorithm

The solving algorithm consists of several procedures for each time-step. The hyperbolic part of the system is solved using a HLLC-MUSCL scheme which is described in detail in sections 3.1.1 and 3.1.2. A pressure relaxation algorithm is then utilized to obtain mechanical equilibrium in the whole computational domain. The structure of the main algorithm is as follows:

Main solver algorithm

```
// --- Initialisation ---
construct computational grid (1D arrays)
read computation parameters from setup-file
set initial conditions

// --- Main loop ---
for each time-step {
    calculate dt using the CFL-condition
    calculate left and right side of cell interfaces (MUSCL-scheme)
    calculate the HLLC-flux at each cell interface
    calculate boundary fluxes
    evolve conservative variables
    evolve non-conservative variables

    if EOS is cubic {
        relax sub-spinodal states to spinodal-equilibrium
    }

    pressure relaxation (all cells)
    thermodynamic relaxation (according to relaxation criterion)
}
end of algorithm
```

The conservative variables are evolved according to eq. 3.21, and the non-conservative according to eq. 3.22 and 3.23.

B.2 Pressure relaxation - SG-EOS

Pressure relaxation algorithm with SG-EOS

```
for all cells {
    find phasic density and internal energy from the evolved variable groups
    calculate initial pressure of each phase, p(rho, e)
    calculate acoustic impedance of each phase, Z(rho, p)
    calculate initial interface pressure pI(p, Z)
```

```
6
7           estimate relaxed pressure
8           calculate the relaxed volume fraction using the relaxed pressure estimate
9           calculate the mixture pressure using the conserved mixture internal energy
10          re-initialize the phasic energy variable groups using the mixture pressure
11      }
```

B.3 Thermodynamic relaxation - vdW-EOS

The full thermodynamic relaxation algorithm is very computationally expensive. It makes use of a nested iteration procedure, with a sub iteration process of typically 3-4 iterations for each main iteration step. With a reasonable first guess, it takes 3-5 main iterations to converge. The algorithm is not optimized, as the current numerical code is intended for proof of concept purposes only. Note that the single phase limit parts of the algorithm is shown only for the limit of single phase 2. The real algorithm contains these parts for both phases.

Thermodynamic relaxation with vdW-EOS

```
1   for each cell {
2       // --- Input variables ---
3       // de: mixture reduced volume
4       // eps: mixture reduced internal energy
5       // de1: first guess of reduced volume, phase 1
6       // de2: first guess of reduced volume, phase 2
7       // d_de1: first guess of difference in reduced volume, phase 1
8
9       // --- Other variables ---
10      // tau: mixture reduced temperature
11      // Y1: mass fraction of phase 1
12
13      if ( eps > eps_max_equal_temperature(de) ) {
14          // --- Non-equal temperature single phase limit solution ---
15          while (abs(error) > ERROR_LIMIT_NON_EQUAL_TEMPERATURE) {
16              de2 = de2(de1, de, alpha_limit)
17              pi = pi_spinodal(de1)
18              tau2 = tau(de2, pi)
19              eps2 = epsilon(de2, tau2)
20              Y1 = (de - de2)/(de1 - de2)
21              error = Y1 * ( eps_spinodal(de1) - eps2 ) + eps2 - eps
22              d_error = d_error_d_de1_non_eq_T(de1) // Derivative of error function
23              de1 = de1 - error/d_error
24          }
25      } else if ( eps > eps_max_equilibrium(de) ) {
26          // --- Equal temperature single phase limit solution ---
27          while (abs(error) > ERROR_LIMIT_EQUAL_TEMPERATURE) {
28              de2_de = de2(de1, de, alpha_limit)
29              de2_eps = de2_epsilon(de, eps, de1)
30              error = de2_de - de2_eps
31              d_error = d_error_d_de1_eq_T(de1) // Derivative of error function
32              de1 = de1 - error/d_error
33          }
34      } else {
35          // --- Full thermodynamic equilibrium solution ---
36          de2 = de2_sat(de1, de2)
37          tau = tau_equal_pressure(de1, de2)
38          Y1 = (de - de2)/(de1 - de2)
39          error0 = Y1 * epsilon(de1, tau) + (1 - Y1) * epsilon(de2, tau) - eps
```

```
        while (abs(error0) > ERROR_LIMIT_FULL_EQUILIBRIUM) {
            de1 = de1 + d_de1
            de2 = de2_sat(de1, de2)
            tau = tau_equal_pressure(de1, de2)
            Y1 = (de - de2)/(de1 - de2)
            error1 = Y1 * epsilon(de1, tau) + (1 - Y1) * epsilon(de2, tau) - eps
            d_error_d_de1 = (error1 - error0) / d_de1
            d_de1 = - error1 / d_error_d_de1
            error0 = error1
        }
    }
}
```

Bibliography

[1] J.D. Anderson. *Computational Fluid Dynamics*. McGraw-Hill Science/Engineering/Math, 1995.

[2] R. Span and W. Wagner. A new equation of state for carbon dioxide covering the fluid region from the triple-point temperature to 1100 K at pressures up to 800 MPa. *Journal of Physical and Chemical Reference Data*, 25(6):1509–1596, 1996.

[3] R. Menikoff and B.J. Plohr. The Riemann Problem for Fluid-Flow of Real Materials. *Reviews of Modern Physics*, 61(1):75–130, 1989.

[4] R. Saurel, F. Petitpas, and R. Abgrall. Modelling phase transition in metastable liquids: application to cavitating and flashing flows. *Journal of Fluid Mechanics*, 607:313–350, 2008.

[5] T. Abbasi and S.A. Abbasi. The boiling liquid expanding vapour explosion (BLEVE): Mechanism, consequence assessment, management. *Journal Of Hazardous Materials*, 141(3):489–519, 2007.

[6] A.M. Birk, C. Davison, and M. Cunningham. Blast overpressures from medium scale BLEVE tests. *Journal of Loss Prevention in the Process Industries*, 20(3):194 – 206, 2007.

[7] R.C. Reid. Possible mechanism for pressurized-liquid tank explosions or BLEVE's. *Science*, 203(4386):1263–1265, 1979.

[8] P.B. Debenedetti. *Metastable Liquids: Concepts and Principles*. Princeton University Press, 1996.

[9] M.A. Grolmes and H.K. Fauske. Axial propagation of free surface boiling into superheated liquids in vertical tubes. In *Heat transfer 1974; Proceedings of the Fifth International Conference, Tokyo*, volume 4, pages 30–34, 1974.

[10] V.H. Arakeri P.K. Das, G.S. Bhat. Investigations on the propagation of free surface boiling in a vertical superheated liquid column. *International Journal of Heat and Mass Transfer*, 30(4):631–638, 1987.

[11] P. Reinke and G. Yadigaroglu. Explosive vaporization of superheated liquids by boiling fronts. *International Journal of Multiphase Flow*, 27(9):1487 – 1516, 2001.

[12] D. Bjerketvedt, K. Egeberg, W. Ke, A. Gaathaug, K. Vaagsaether, and S.H. Nilsen. Boiling liquid expanding vapour explosion in CO2 small scale experiments. *Energy Procedia*, 4(0):2285 – 2292, 2011. 10th International Conference on Greenhouse Gas Control Technologies.

[13] P.A. Thompson, H. Craves, G.E.A. Meier, Yoon-Gon Kim, and H.D. Speckmann. Wave splitting in a fluid of large heat capacity. *Journal of Fluid Mechanics*, 185:385–414, 1987.

[14] L.G. Hill. *An experimental study of evaporation waves in a superheated liquid*. PhD thesis, California Institute of Technology, 1990.

[15] J.R. Simões-Moreira and J.E. Shepherd. Evaporation waves in superheated dodecane. *Journal Of Fluid Mechanics*, 382:63–86, 1999.

[16] R. Saurel and R. Abgrall. A multiphase Godunov method for compressible multifluid and multiphase flows. *Journal of Computational Physics*, 150(2):425–467, 1999.

[17] A. Zein, M. Hantke, and G. Warnecke. Modeling phase transition for compressible two-phase flows applied to metastable liquids. *Journal of Computational Physics*, 229(8):2964–2998, 2010.

[18] Geum-Su Yeom and Keun-Shik Chang. A modified HLLC-type riemann solver for the compressible six-equation two-fluid model. *Computers & Fluids*, 76:86 – 104, 2013.

[19] E. Romenski, D. Drikakis, and E. Toro. Conservative models and numerical methods for compressible two-phase flow. *Journal of Scientific Computing*, 42(1):68–95, 2009.

[20] J. B. R. Rose, S. Dhanalakshmi, and G. R. Jinu. Experimental and numerical analysis of compressible two-phase flows in a shock tube. *International Journal of Modeling, Simulation, and Scientific Computing*, 06(03):1550025, 2015.

[21] S. Diot, M.M. Franois, and E.D. Dendy. A higher-order unsplit 2d direct eulerian finite volume method for two-material compressible flows based on the mood paradigms. *International Journal for Numerical Methods in Fluids*, 76(12):1064–1087, 2014.

[22] Y.-Y. Niu, Y.-C. Lin, and C.-H. Chang. A further work on multi-phase two-fluid approach for compressible multi-phase flows. *International Journal for Numerical Methods in Fluids*, 58(8):879–896, 2008.

[23] G.A. Pinhasi, A. Ullmann, and A. Dayan. 1D plane numerical model for boiling liquid expanding vapor explosion (BLEVE). *International Journal of Heat and Mass Transfer*, 50(23-24):4780–4795, 2007.

[24] M.M. Voort, A.C. Berg, D.J.E.M. Roekaerts, M. Xie, and P.C.J. Bruijn. Blast from explosive evaporation of carbon dioxide: experiment, modeling and physics. *Shock Waves*, 22(2):129–140, 2012.

[25] M. Xie. *Thermodynamic and Gasdynamic Aspects of a Boiling Liquid Expanding Vapour Explosion.* PhD thesis, Delft University of Technology, 2013.

[26] R.F. Kunz, D.A. Boger, D.R. Stinebring, T.S. Chyczewski, J.W. Lindau, H.J. Gibeling, S. Venkateswaran, and T.R. Govindan. A preconditioned Navier Stokes method for two-phase flows with application to cavitation prediction. *Computers & Fluids*, 29(8):849 – 875, 2000.

[27] G. La Spina, M. de' Michieli Vitturi, and E. Romenski. A compressible single-temperature conservative two-phase model with phase transitions. *International Journal for Numerical Methods in Fluids*, 76(5):282–311, 2014.

[28] M.-H. Lallemand, A. Chinnayya, and O. Le Metayer. Pressure relaxation procedures for multiphase compressible flows. *International Journal for Numerical Methods in Fluids*, 49(1):1–56, 2005.

[29] M. Slemrod. Dynamic phase transitions in a van der waals fluid. *Journal of Differential Equations*, 52(1):1 – 23, 1984.

[30] H.W. Zheng, C. Shu, Y.T. Chew, and N. Qin. A solution adaptive simulation of compressible multi-fluid flows with general equation of state. *International Journal for Numerical Methods in Fluids*, 67(5):616–637, 2011.

[31] O. Le Metayer, J. Massoni, and R. Saurel. Elaborating equations of state of a liquid and its vapor for two-phase flow models. *International Journal of Thermal Sciences*, 43(3):265–276, 2004.

[32] D.L. Morgan and R. Kobayashi. Direct vapor pressure measurements of ten n-alkanes m the 10-c28 range. *Fluid Phase Equilibria*, 97:211 – 242, 1994.

[33] R. H. Swendsen. *An Introduction to Statistical Mechanics and Thermodynamics.* Oxford University Press, 2012.

[34] D. S. Lemons and C. M. Lund. Thermodynamics of high temperature, Mie - Gruneisen solids. *American Journal of Physics*, 67(12):1105–1108, 1999.

[35] Cubic formula. `http://mathworld.wolfram.com/CubicFormula.html`. Accessed: 2016-11-19.

[36] R. Saurel, F. Petitpas, and R.A. Berry. Simple and efficient relaxation methods for interfaces separating compressible fluids, cavitating flows and shocks in multiphase mixtures. *Journal of Computational Physics*, 228(5):1678–1712, 2009.

[37] E.F. Toro. *Riemann solvers and numerical methods for fluid dynamics*. Springer-Verlag, second edition, 1999.

[38] F. Petitpas, E. Franquet, R. Saurel, and O. Le Metayer. A relaxation-projection method for compressible flows. Part II: Artificial heat exchanges for multiphase shocks. *Journal of Computational Physics*, 225(2):2214–2248, 2007.

[39] A.K. Kapila, R. Menikoff, J.B. Bdzil, S.F. Son, and D.S. Stewart. Two-phase modeling of deflagration-to-detonation transition in granular materials: Reduced equations. *Physics of Fluids*, 13(10):3002–3024, 2001.

[40] S. Tosse, K. Vaagsaether, and D. Bjerketvedt. An experimental investigation of rapid boiling of CO_2. *Shock Waves*, 25(3):277–282, 2015.

[41] J.R. Simões-Moreira. Oblique evaporation waves. *Shock Waves*, 10(4):229–234, 2000.

Publications

The following articles has been published as part of the PhD. They are provided for completeness.

Available online at www.sciencedirect.com

SciVerse ScienceDirect

Energy Procedia 37 (2013) 4818 – 4824

Energy Procedia

GHGT-11

Experimental study of CO_2 releases from a saturated liquid reservoir

S. Toesse[1*], K. Vaagsaether[1], J. Lundberg[1], A. V. Gaathaug[1], D. Bjerketvedt[1,3], S. Nilsen[2], C. K. Jayarathna[3].

Telemark University College, Faculty of Technology, Kjolnes Ring 56, 3918, Porsgrunn, Norway
[2]Statoil ASA, Hydrovegen 67, 3936, Porsgrunn, Norway, [3]Tel-Tek, Kjolnes Ring 30, 3918, Porsgrunn, Norway

Abstract

To improve the tools used in safety assessments for handling transport and storage of CO2 experimental results are used as a reference. The present study measures mass flux, temperature of the jet and particle sizes of a release from a liquid CO_2 reservoir. In a release to the atmosphere from a liquid reservoir with a pressure of 6 MPa and 293 K, the jet formed consists of gas and solid particles. In the experiments the CO_2 is released through nozzles of 0.25 mm, 0.5 mm, 1 mm and 2.5 mm diameters. Both high speed imaging and laser diffraction is used for particle characterization. The results show that the jet core temperature is 205 K close to the release and increases after 100 diameters. The measured mass flux decreases with increasing nozzle diameter. The average mass flux is 38 g/s· mm^2. The high speed imaging shows particle sizes of 20-80 μm with velocities up to 100 m/s at the edges of the jet. It was not possible to measure particles in the jet core with high speed imaging. The laser diffraction experiments show a clear particle size concentration of about 1 μm.

Selection and/or peer-review under responsibility of GHGT

Keywords: Safety; Carbon Capture and Storage; CO_2 Jet; Particle dispersion;

1. Introduction

CO_2 Capture and Storage (CCS) involve processing and transport of large amounts of CO_2 in dense liquid phase. Current tools for safety assessment have contributed to the successful design and operation

* Corresponding author. Tel.: +47 35575119; fax: +47 35 57 54 01.
E-mail address: sindre.tosse@hit.no.

1876-6102
Selection and/or peer-review under responsibility of GHGT
doi:10.1016/j.egypro.2013.06.391

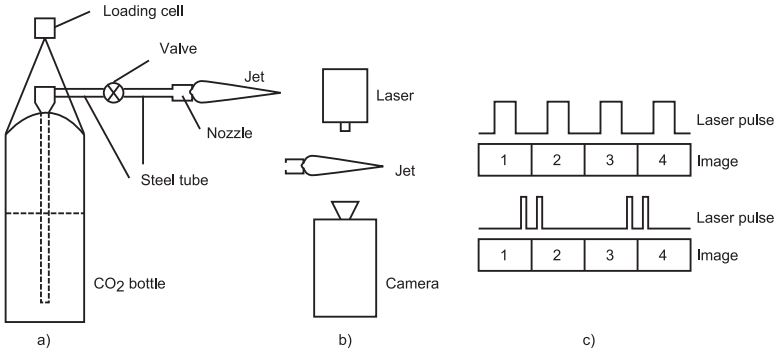

Fig. 1. (a) Schematic overview of the experimental setup; (b) High speed imaging setup; (c) Traditional imaging with high frame rate (top), image pairing with lower frame rate (bottom)

of CO_2 compression and transport systems worldwide. To achieve even safer operation of such installations and to increase authority and public confidence it is important to reduce the uncertainty even more in the predictions of what happens if CO_2 is accidentally released.

Several experimental projects are going on to establish experimental data related to safety distances. However, the thermodynamics and fluid dynamics involved in a sudden release of CO_2 is complex, both to measure and to model numerically. Even if validated models for heavy gas dispersion exist in general, the distance downwind to the point where all the CO_2 dry ice is sublimated might be significant for a large release. The phase transition in the expansion zone might have a significant impact on the dispersion further downstream. Local geometry and wind conditions will also have a very important impact. Therefore experimental results are necessary to validate and further improve the numerical models. Statoil has put a significant effort in financing research activities to obtain such data. Pressurized liquid CO_2 is also a safety hazard in terms of accidental vessel ruptures which can result in a BLEVE (Boiling Liquid Expanding Vapor Explosion) [1], but also in cases where a vessel is partially ruptured leading to a CO_2 jet. It is important to understand the mechanics of such jet, both to be able to calculate realistic leak rates and to assess the risk factor to the immediate surroundings. When liquid CO_2 is released through a nozzle, the rapid expansion quickly cools the liquid. Depending on the initial conditions, equilibrium between gas and liquid droplets or solid particles will occur inside the jet. During the release of CO_2 in the present research, solid particles (dry ice) were formed inside the jet.

Liu et al. [2] used a high speed camera and microscopic lens to examine the agglomeration process of dry ice in a jet. The dry ice was formed by expanding liquid carbon dioxide through an expansion nozzle. They used a glass tube to keep the temperature inside the jet low. They found particles with a size distribution of 40 to 400 µm. The velocity of the particles was relatively low (in the order of 1-20 m/s) compared to the experiments presented in this article.

Liu et al. [3] also used laser diffraction analysis to measure the size distribution of the particles. Using this method, they found particles with a diameter around 1µm. They found some variations with the size of the particles with the distance from the nozzle opening.

2. Experimental setup

The experimental rig used in the present research consisted of a nozzle connected to a bottle of CO_2 with a riser tube. A pneumatically controlled valve was used to control the flow of CO_2 from the nozzle. The gas bottle was hanging in a loading cell, so that continuous measurements of the total weight of the

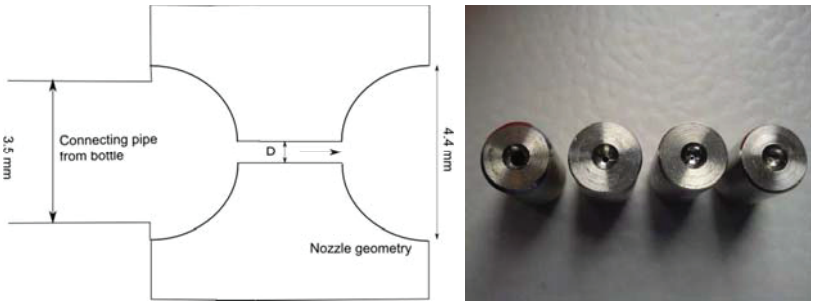

Fig. 2. (a) Schematic view of the nozzle geometry; (b) Photograph of the four nozzles used in the experiments. Throat sizes (D) from left are: 2.5mm, 1mm, 0.5mm, 0.25mm

bottle were obtained. These measurements were used to calculate mass flow. A temperature element with a diameter of 1 mm was used to measure the temperature inside the jet. A schematic overview of the experimental setup is shown in fig. 1. Two different measurements techniques were used to analyze the composition of the jet. High speed imaging was used to measure particle size and velocity of particles inside the jet. A laser diffraction analyzer was used to measure the size distribution of the same particles.

A schematic view of the nozzle geometry can be found in fig 2 a) and a photograph of the different nozzles is found in fig 2 b).

2.1. High speed imaging

A high speed camera of type Photron APX-RS was used to take photographs of the jet. Close-up images of the jet were taken using a Navitar 12X zoom lens to measure the size and velocity of particles inside the jet. These images were taken using laser pulses from a LED Laser of type Oxford Laser Firefly-300 as lighting source. A 70 mm lens and white light was used to take photographs of the shape of the jet.

2.2. Particle image velocimetry

When measuring particle velocities in the order of 100 m/s on a length scale of 5 mm, the frame rate has to be at least in the order of 50 kfps if no special techniques are used. By firing laser pulses in pairs, and pairing images, a much lower frame rate can be used (see fig 1 c)). The laser used in these experiments can fire pulses only microseconds apart. This is sufficient to determine the position of a particle in two subsequent pictures and, since the time difference is known, the velocity of the particle can be determined.

2.3. Laser diffraction analysis

A series of experiments was conducted using laser diffraction analysis (HELOS, Sympatec GmbH). This is a method that is based on the light scattering properties of particles. The sample (in this case the CO_2 jet) is fed through a laser beam, and the scattering of light is measured. Based on some assumptions, the size distribution of the particles is found by the scattering measurement.

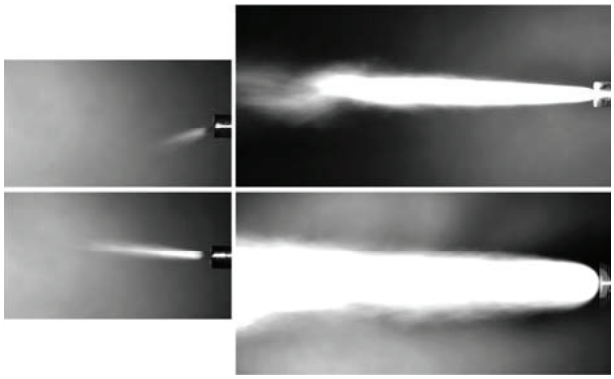

Fig. 3. Overview of the jet shape for the different nozzle throat diameters; 0.25 mm (upper left), 0.5 mm (lower left), 1 mm (upper right), 2.5 mm (lower right)

3. Results and discussion

3.1. Overview and shape of jet

Fig. 3 shows an overview of the jet shapes for four different nozzles. The jet from the 0.25 mm nozzle is asymmetric. This is probably caused by some foreign object inside the nozzle throat, or structural damage to the nozzle.

3.2. Mass flow

The experimental results for mass flow were used to calculate a mass flux (kg/m^2s). The mass flux for each nozzle and the average mass flux is shown in fig. 4 a). The mass flux decreases with increasing nozzle diameter.

3.3. Temperature measurements

All temperature measurements were done with the 1 mm nozzle. In the temperature measurements, the temperature reached a stable level after some seconds. This stable level was used as the jet temperature. Fig. 4 b) shows the temperature in the jet plotted with distance from the nozzle opening. The plot shows that the temperature varies little in the zone 0 - 100 mm from the nozzle opening.

High speed images of the temperature element shows a cone of solid CO_2 growing on the temperature element. The cone evaporated quickly after the experiment, leaving no moisture. This shows that it was in fact dry ice and not water from the surrounding air. The boiling temperature of CO2 at atmospheric pressure is 195 K while the lowest temperature measured in the jet is 205 K. This corresponds to the boiling point of CO2 at approximately 2.3 times atmospheric pressure (0.23 MPa).

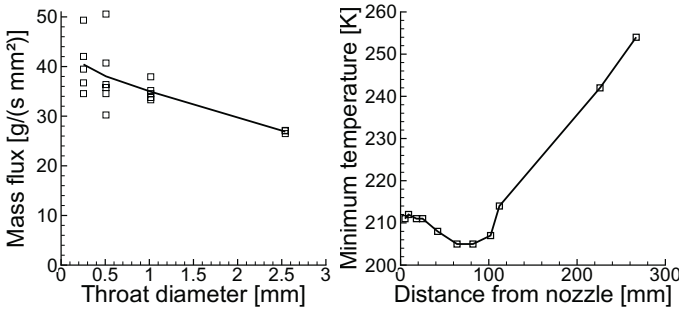

Fig. 4. (a) Mass flux for the four nozzle throat diameters. The solid line is the average mass flux. (b) Temperature variations with distance from the nozzle opening with the 1 mm nozzle.

It is possible that the presence of the temperature element causes a stagnation of the flow and a locally high pressure. This can also account for the small rise in temperature close to the nozzle opening, as the higher local velocity will lead to a higher stagnation pressure. After 100 mm the temperature increases due to entrainment of the surrounding air.

3.4. Close-up images of jet

The 1 mm nozzle was used in the investigation of particle sizes and velocities. A selection of photographs is shown in fig. 5. In close-up images of the jet, the center of the jet was totally opaque. It is possible that the density of particles is much higher in the center of the jet than in the outer region. However, large density fluctuations in the jet may also cause total dispersion of the laser beam.

Table 1. Particle size distribution in the jet from the 1 mm nozzle. Image position refers to fig. 5.

Particle	Image position	Diameter [μm]	Velocity [m/s]
1	a)	35	96
2	a)	20	28
3	a)	26	53
4	a)	32	53
5	a)	30	31
6	b)	78	67
7	b)	26	29
8	b)	37	50
9	b)	35	54
10	b)	20	53
11	c)	39	48
12	c)	32	65
13	c)	65	98
14	c)	21	56
15	c)	23	46

In the outer region of the jet, small particles with a diameter of roughly 20-80 microns were observed. Table 1 shows the diameter and velocity of some of these particles. It is possible that the large particles observed in the outer region of the jet are dry ice that has been formed on the nozzle wall and not by sublimation of liquid carbon dioxide.

3.5. Laser diffraction analysis

In the laser diffraction analysis, the 0.25 mm and 0.5 mm nozzles were used. In the measurements with the 0.5 mm nozzle, some beam steering was encountered. This is a phenomenon that occurs when the jet has a significantly different refraction index than the air around it. It shows up as coarse particles in the upper channels on the laser diffraction analyzer [3]. The particle distribution is therefore limited at 20 µm, since high speed images of the jet shows small concentrations of larger particles in the jet. What is clear in fig. 6 is that there is a peak of particles with a characteristic size around 1 µm. From these

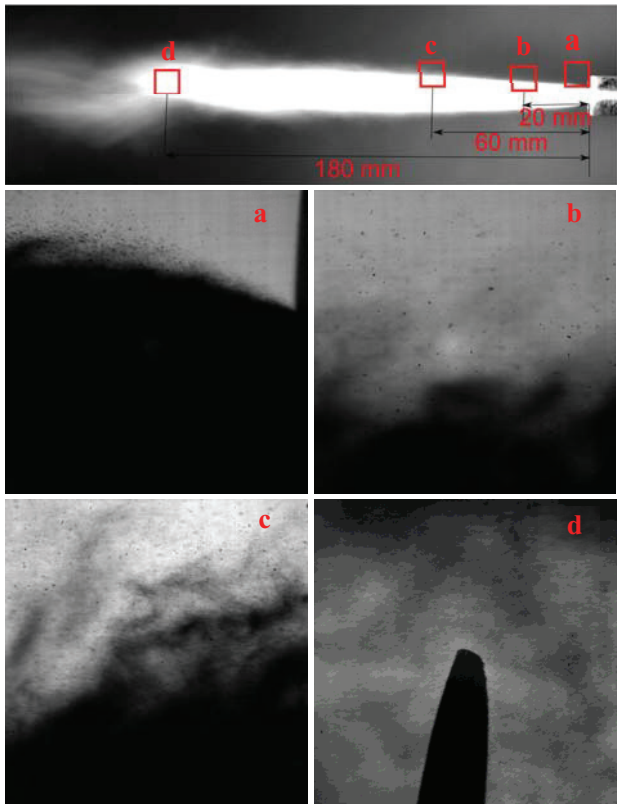

Fig. 5. Close-up images of the jet from the 1 mm nozzle; (a) Nozzle opening; (b) 20 mm from nozzle opening; (c) 60 mm from nozzle opening; (d) 180 mm from nozzle opening. The large object in d) is a needle used for positioning and camera focus. All four images are 5.3 x 5.3 mm in the focus plane. This corresponds to a pixel size of 5.22 µm.

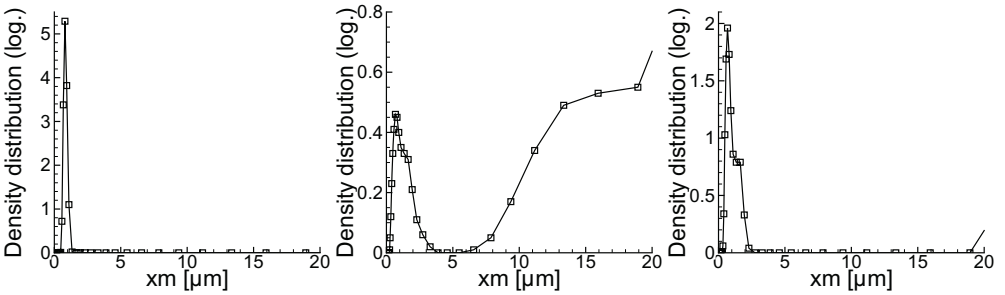

Fig. 6. a) Density distribution for the 0.25 mm nozzle; b) and c) Density distributions for two different positions in the jet from the 0.5 mm nozzle

measurements, it is likely that the opaque center of the jet seen in fig. 5 consists mainly of particles with a diameter in the order of 1 µm. This is consistent with earlier research by Liu et al. [3].

4. Conclusions

- The temperature in the core of a CO_2 jet seems to be constant out to a certain point.
- The core of the jet is opaque, leaving high speed imaging ineffective to determine its composition.
- Some larger particles (20 – 80 µm) were observed in the outer part of the jet.
- Laser diffraction analysis shows a clear peak of particles with a size around 1µm in the jet.

Further experiments are planned in order to obtain better measurements of the composition of a CO_2 jet. It seems clear that high speed photography with back lighting is not sufficient to determine the composition of the jet core, both because of the high dispersion of light through the core and because of the small length scales of particles. Laser diffraction measurements with exact positioning in the jet are needed to determine how the particle distribution develops downstream from the nozzle. Further work will enable the development of numerical models for CO_2 jets to be used in risk assessment.

Acknowledgements

The work presented here is funded by Statoil ASA.

References

[1] Bjerketvedt D, Egeberg K., Ke W, Gaathaug A, Vaagsaether K, Nilsen SH, Boiling liquid expanding vapour explosion in CO_2 Small scale experiments, *Energy Procedia 2011*;**4**:2285-2292

[2] Liu YH, Maruyama H, Matsusaka S, Agglomeration process of dry ice particles produced by expanding liquid carbon dioxide, *Advanced Powder Technology 2010*;**21**:652-657

[3] Liu YH, Calvert G, Hare C, Ghadiri M, Matsusaka S, Size measurement of dry ice particles produced from liquid carbon dioxide, *Journal of Aerosol Science 2012*;**48**:1-9

Shock Waves (2015) 25:277–282
DOI 10.1007/s00193-014-0523-6

ORIGINAL ARTICLE

An experimental investigation of rapid boiling of CO_2

S. Tosse · K. Vaagsaether · D. Bjerketvedt

Received: 30 October 2013 / Revised: 21 August 2014 / Accepted: 26 August 2014 / Published online: 27 September 2014

Abstract Storage of pressurized liquified gases is a growing safety concern in many industries. Knowledge of the thermodynamics and kinetics involved in the rapid depressurization and evaporation of such substances is key to the design and implementation of effective safety measures in storage and transportation situations. In the present study, experiments on the rapid depressurization of liquid CO_2 are conducted in a vertical transparent shock tube which enables the observation of evaporation waves and other structures. The depressurization was initiated by puncturing a membrane in one end of the tube. The thermodynamic mechanisms that govern the evaporation process are not unique to CO_2, and the same principles can be applied to any liquified gas. The experiments were photographed by a high-speed camera. Evaporation waves propagating into the liquid were observed, traveling at a near constant velocity on the order of 20–30 m/s. A contact surface between the vapor and the liquid–vapor mixture was also observed, accelerating out of the tube. Pressure readings in the tube suggest that the evaporation wave could be similar to a spinodal decomposition wave, but further experiments are needed to confirm this. When the membrane was in direct contact with the liquified CO_2, some indications of homogeneous nucleation were observed.

Communicated by G. Ciccarelli.

This paper is based on work that was presented at the 24th International Colloquium on the Dynamics of Explosions and Reactive Systems, Taipei, Taiwan, July 28–August 2, 2013.

S. Tosse (✉) · K. Vaagsaether · D. Bjerketvedt
Faculty of Technology, Telemark University College,
Kjolnes Ring 56, 3918 Porsgrunn, Norway
e-mail: sindre.tosse@hit.no

Keywords CO_2 · Phase transition · Evaporation waves · Two-phase flow

1 Introduction

Accidental explosions involving the rapid boiling of liquified gases are of great concern in process safety. Such events are sometimes referred to as Boiling Liquid Expanding Vapor Explosions (BLEVEs). A BLEVE can occur in the storage and transportation of high pressure liquified gases such as LPG or CO_2. To prevent and mitigate BLEVE accidents, detailed knowledge about the thermodynamic process is needed. There are several definitions of the term BLEVE, an overview of which is provided by Abbasi and Abbasi [1]. Some of the definitions involve complete failure of the vessel. Based on such a definition, the present experiments do not qualify as a BLEVE. However, the research is still relevant for BLEVE-type scenarios as the governing kinetics and thermodynamics is the same.

Evaporation waves in a superheated liquid (Refrigerant 12 and 114) were observed by Hill [2]. Simoes-Moreira and Shepherd [3] also performed a series of experiments with superheated dodecane. Reinke and Yadigaroglu [4] did a series of experiments with explosive vaporization in propane, butane and refrigerant R-134a. Bjerketvedt et al. [5] conducted a series of small-scale experiments with CO_2 BLEVEs. Some work has been done to develop numerical models that are capable of describing evaporation waves. Saurel et al. [6] developed a Godunov method for compressible multiphase flow that was later applied to the subject of phase transition in metastable liquids [7]. They were able to qualitatively reproduce the evaporation front velocities measured by Simoes-Moreira and Shepherd. Zein et al. [8] used the same numerical model to reproduce the results of Simoes-

Moreira and Shepherd with better accuracy. In recent years, there have also been several attempts to model BLEVE-type scenarios [9–11]. The knowledge of detailed thermodynamics and kinetics is important in the validation of such models.

The scope of the experimental work is to provide insight into the overall thermodynamics and kinetics that govern the evaporation process in superheated CO_2. Velocities of evaporation waves and contact surfaces as well as pressure readings are important in providing such insight. The results will also function as a basic reference for a numerical model capable of describing the boiling mechanisms in superheated CO_2. Validation of such a model will require more detailed experimental work, particularly with pressure readings at several points in the tube (only two pressure transducers were used in the present setup). Lastly, the present study will serve as a reference if a new experimental rig is constructed.

It is common to use term boiling for the phase transition that takes place when vapor bubbles form within a liquid body or at an interface with a solid body. In the present experimental work, there is often no clear liquid surface or body but rather a mixture of vapor and liquid. The term evaporation waves is described by Simoes-Moreira [12] as 'processes that may occur under certain conditions in which a metastable or superheated liquid undergoes a sudden phase transition in a narrow and observable region [...].' We use this term when such phenomena are observed and the term boiling for other liquid–gas phase transitions.

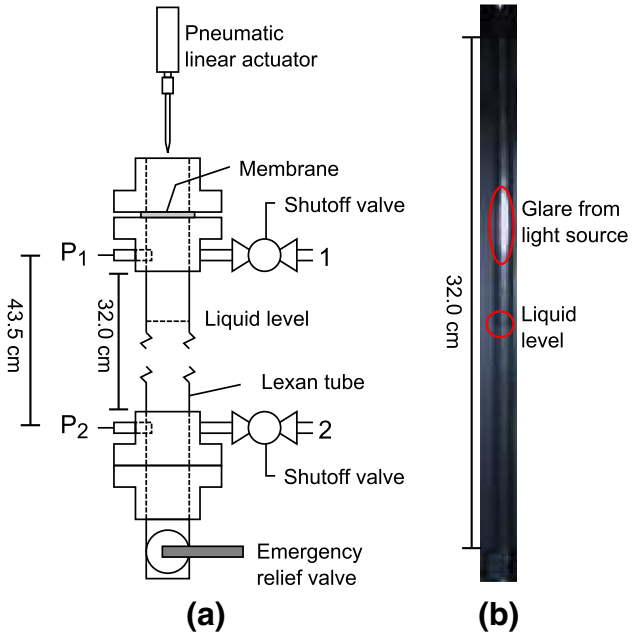

Fig. 1 **a** Schematic illustration of the shock tube with vapor side penetration (not to scale). The tube was filled at the inlet (2), while (1) was used for controlled pressure relief to allow liquid CO_2 to fill the tube. P_1 and P_2 are pressure transducers. The distance from P_1 to P_2 was 43.5 cm, and the transparent part of the tube was 32.0 cm in length. **b** Example high-speed shot of the tube filled with liquid CO_2. This is the total field of view of the camera. Note that the length of 32.0 cm indicated in both **a** and **b** is the part of the tube that is shown in the photographs in the result section

2 Experimental setup

The experiment was carried out in a vertically oriented clear Lexan tube partly filled with liquid CO_2. A schematic illustration of the tube is provided in Fig. 1. The visible portion of the tube was 32 cm in length. The inner-diameter of the tube was 9 mm and the outer-diameter was 12 mm. One end of the tube was a membrane which was punctured by a needle. Two layers of Mylar sheet were used as the membrane material. The experiment was photographed using a high-speed camera (Photron APX-RS) at 16,000 frames per second ($64 \times 1{,}024$ pixels), which allowed visual tracking of the various fronts and bulk boiling. The tube was illuminated from the front by white light. Some experiments were done using back lighting, but the light was not able to penetrate the two-phase region. In addition to the high-speed camera, two Kulite XT-190 pressure transducers (P_1 and P_2 in Fig. 1) were used to record the pressure inside the tube. The distance between the two pressure transducers was 43.5 cm. The first series of experiments were conducted with the membrane placed at the top of the tube. The vertical orientation of the tube was reversed in the second series, so that the membrane was at the bottom.

The tube was filled through an inlet valve at the bottom of the tube using liquid CO_2 from a gas bottle with a riser tube. Careful pressure relief at the top of the tube allowed the liquid CO_2 to fill the tube to the desired level. When the fill (1) and relief (2) valves shown in Fig. 1 were closed, the thermodynamic state inside the tube was assumed to be in equilibrium between the liquid and vapor.

3 Experimental results and discussion

The experimental results are provided for two cases. In the first case, the membrane was placed at the top of the tube so that the vapor head space was directly below the membrane. In the second case, the vertical orientation of the tube was reversed so that liquid was located directly above the membrane. The high-speed images are displayed as a series of isochronously spaced images, which allow the fronts to be easily tracked. The front velocities are found by polynomial curve fitting of the front position versus time. All images are cropped to show only the visible portion of the tube, with a height of 32.0 cm. The pixel width was 0.35 mm/px. Visual tracking of fronts is possible, but as the front position is not always clear, some uncertainty in the calculated

velocities should be expected. The uncertainties were estimated by varying the gradient of the velocity to fit within the front region. Due to the curvature of the tube and the lack of magnification, it was not possible to observe the evaporation front structure.

3.1 Vapor side membrane placement

Figure 2 shows the experimental results when the shock tube is filled with liquid CO_2 up to 45 % of the height between P_1 and P_2. The pressure time histories in Fig. 2 show a 1.83 ± 0.09 ms delay between the first pressure drop in the upper and the lower pressure transducer. This corresponds to a mean speed of sound of 238 ± 12 m/s. As a reference, at 5.5 MPa saturated conditions and a liquid fill level of 45 %, the Span–Wagner equation of state [13] gives a mean speed of sound of 248 m/s (198.0 m/s in the vapor and 356.8 m/s in the liquid phase). The Span–Wagner speed of sound of each phase has been plotted as the dashed red line in Fig. 2 to illustrate the predicted path of the first rarefaction wave.

From the pressure drop at P_1, there is a time delay of 0.8 ms until any visual changes occur in the tube. Some of this delay can be explained by the 5.75 cm gap between the pressure transducer and the upper end of the visible portion of the tube, but it is likely that the pressure in the tube drops prior to the appearance of the changes. This implies that the vapor becomes sub-cooled prior to the visual changes. As a reference, isentropic expansion of vapor from the known initial conditions to 3.5 MPa using the Span–Wagner equation of state yields a sub-cooled vapor temperature of 262 K. Since this is well above the triple-point temperature of CO_2 (216.6 K), it is safe to assume that the white front that propagates downwards into the vapor from t = 72 ms (line A in Fig. 2) consists of condensed droplets and not solid particles.

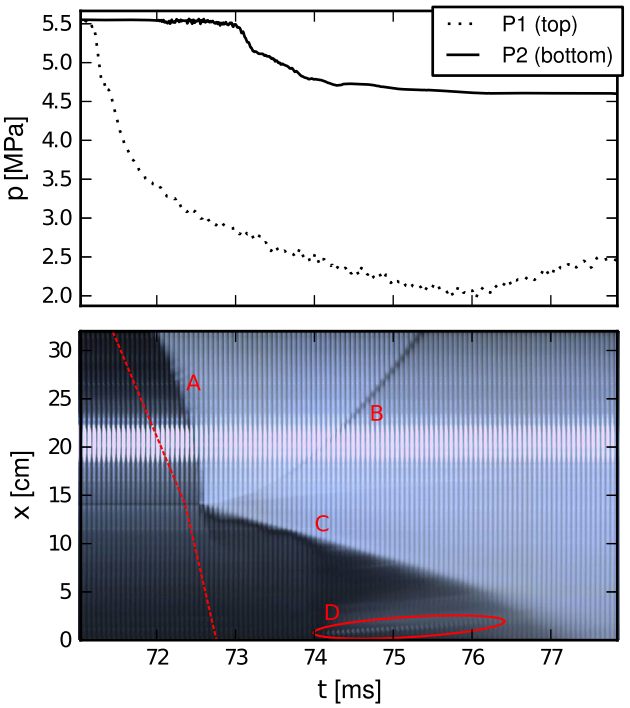

Fig. 2 Experimental results with vapor side membrane penetration. P_1 and P_2 refer to Fig. 1a. The time-scale is relative to the trigger mechanism of the membrane penetration device. The *red dotted line* is the trajectory of the first rarefaction wave traveling at the speed of sound as given by the Span–Wagner equation of state. *A* Condensation wave. *B* Vapor–mixture interface. *C* Evaporation wave. *D* Bubbles in liquid

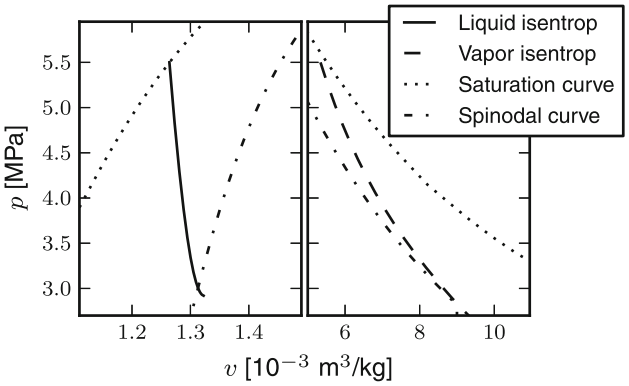

Fig. 3 Isentropic expansion from the initial conditions of saturation at 5.5 MPa in p-v space (Span–Wagner equation of state). The liquid isentrop intersects the spinodal curve at 3.0 MPa. The spinodal curve is defined by $\left(\frac{\partial p}{\partial v}\right)_T = 0$

At 1.4 ms after the initial pressure drop at P_1, the liquid starts to boil at the interface. The boiling propagates as a front into the liquid (line C in Fig. 2). At the same time, a front is seen accelerating upward into the vapor phase (line B in Fig. 2). This is most likely the contact surface between the the vapor and the liquid–vapor mixture that is produced by the boiling liquid. The evaporation front and the contact surface are plotted in Fig. 4. The evaporation front is fitted with a constant velocity of 25 ± 1 m/s and the contact surface is fitted with a constant acceleration of 40.8 ± 0.5 km/s^2. These fronts are well known phenomena in the context of evaporation waves, and are described among others by Pinhasi et al. [9]. The pressure at the top of the tube increases slightly after the contact surface passes, up to a level of 2.6 MPa. Using the Span–Wagner equation of state, the isentrop from the initial 5.5 MPa at saturated conditions intersects the spinodal curve at 3.0 MPa as shown in Fig. 3. While it is impossible to determine the exact pressure in the liquid–vapor mixture zone with the current experimental setup, it is possible that it is on the same order as the top pressure after the contact surface passes. If this is the case, the evaporation front could be close to a spinodal decomposition wave. It should also be noted that the increase in pressure following the exit of the contact surface could be the result of changed choking conditions at the tube exit. When the two-phase mixture is

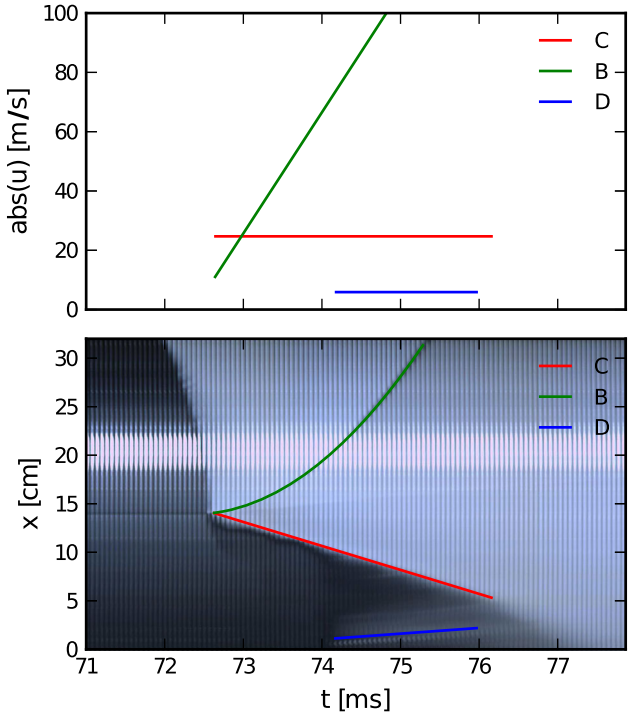

Fig. 4 Curve fittings of front positions and velocities from Fig. 2 plotted with time. *C* Evaporation wave. *B* Vapor–mixture interface. *D* Bubbles in liquid

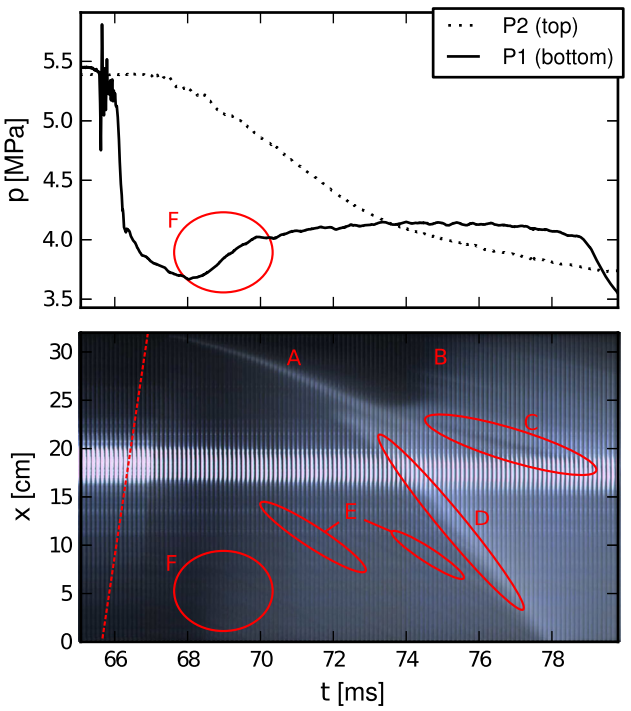

Fig. 5 Experimental results with liquid side membrane penetration. P_1 and P_2 refer to Fig. 1a. The time-scale is relative to the trigger mechanism of the membrane penetration device. The *red dotted line* is the trajectory of the first rarefaction wave traveling at the speed of sound as given by the Span–Wagner equation of state. *A* Liquid–vapor interface. *B* Condensation wave. *C* Vapor–mixture interface. *D* Evaporation wave. *E* Bubbles in liquid. *F* Homogeneous boiling

subject to the sudden pressure drop at the tube exit, some of the liquid will evaporate.

After t = 74 ms, the liquid appears to be boiling at the bottom of the tube (region D in Fig. 2). At this point, P_2 is stabilized at roughly 4.6 MPa. The pressure is most likely stabilized because of the boiling process in the liquid. The boiling appears to be non-homogeneous so it is most likely caused by impurities at the wall or at the tube end. Some structures are observed moving upwards. In Fig. 4, these structures are fitted to a constant velocity of 6.0 ± 0.5 m/s. This may be an indication of bulk fluid velocity.

3.2 Liquid side membrane placement

In these experiments, the membrane was placed at the bottom of the tube. Figure 5 shows the experimental results with the tube filled with liquid CO_2 up to the top of the visible portion. The dashed red line in the figure is the predicted path of the first rarefaction wave based on the Span–Wagner speed of sound. At 2.0 ms after the first drop in P_1, the first sign of boiling appears. It is interesting to note that the boiling appears to be initiated at the liquid–vapor interface at the top even though the membrane is located at the bottom of the tube. The liquid also boils at the membrane side, but the velocity of liquid flowing out of the tube is greater than that of the boiling, so the lower evaporation wave is never visible. The liquid–vapor interface is accelerating downward (line A in Fig. 5). The white area at the interface is expanding from barely visible at t = 68 ms to 1 cm in height at t = 72 ms. The white area could be liquid boiling at a low rate. At t = 75.5 ms the vapor phase becomes opaque (line B in Fig. 5). This is assumed to be caused by a condensation process in the sub-cooled vapor like in the previous setup. The condensation appears to be initiated at the liquid–vapor interface and propagates upward into the vapor for some time before the rest of the vapor condensates simultaneously. The liquid–vapor interface continues downward, but appears to decelerate (region C in Fig. 5). Around t = 72 ms, a new front appears (region D in Fig. 5) and accelerates downward into the liquid.

The accelerating front is most likely an evaporation wave similar to the one observed in the first series of experiments. Region C is then possibly a mixture-vapor contact surface. The difference is that in the first series, the liquid flow velocity was in the opposite direction of the evaporation wave. Here, the liquid phase is flowing out of the tube at an unknown, possibly increasing flow velocity. Figure 6 shows curve fittings of the liquid–vapor interface and the evaporation wave.

With careful consideration of Fig. 5, one can observe some white streaks in the liquid phase (region E in Fig. 5), cor-

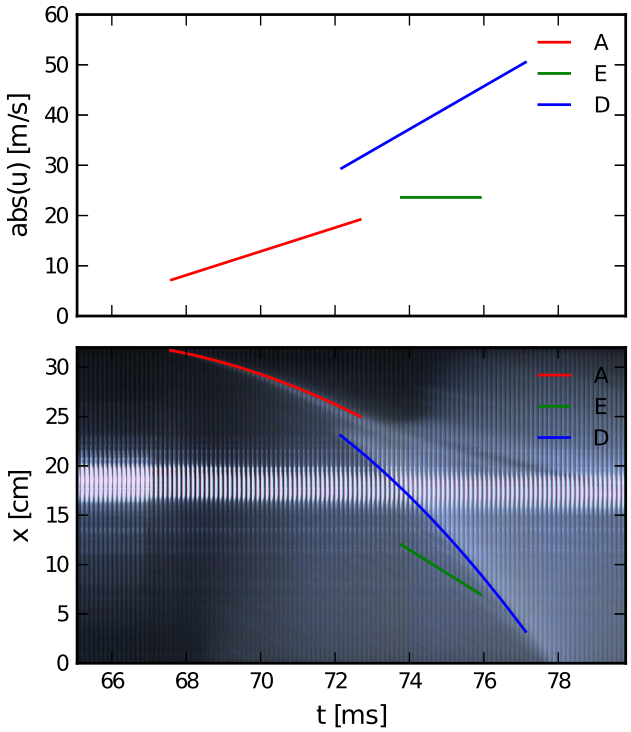

Fig. 6 Curve fittings of front positions and velocities from Fig. 5 plotted with time. *A* Liquid–vapor interface. *E* Bubbles in liquid. *D* Evaporation wave

responding to a velocity on the order of 20 m/s (line E in Fig. 6). Note that these streaks are barely visible. They are most likely small structures (bubbles) in the liquid that act as tracers from which the liquid velocity can be inferred, but the nature of the observations makes further investigations necessary to confirm this.

Between $t = 68$ ms and $t = 70$ ms, there is an increase in the bottom pressure as well as a distinct change in brightness in the liquid (region F in Fig. 5). The change appears to be homogeneous. This may be an indication of homogeneous nucleation.

Due to various reasons, only one complete data set exists for the setup with the membrane placed at the bottom of the tube. This implies that the repeatability of the results presented in this section is unknown and that these results may be unique.

4 Conclusion

- The current setup of high-speed photography is capable of capturing the propagation of evaporation waves and contact surfaces in a tube with liquid CO_2. Rarefaction waves were not observed.
- The small diameter of the tube makes it difficult to observe detailed structures, especially in the cross-sectional direction.
- When the membrane was burst on the vapor (top) side, an evaporation wave was observed that traveled into the liquid with a velocity on the order of 20–30 m/s. Another front, assumed to be the contact surface between the vapor and the liquid–vapor mixture, was also observed accelerating out of the tube.
- When the membrane was burst on the liquid (bottom) side, an evaporation wave and a contact surface still appeared at the top of the tube, but further experiments are needed to determine the front velocities. Some indications of homogeneous nucleation were observed in the superheated liquid.

Due to the lack of pressure measurements inside the tube, it is hard to say anything about the thermodynamic states in the observed structures. Knowledge about such states is critical for understanding the governing mechanisms in a BLEVE. A new experimental setup is needed to provide pressure and temperature readings at several places in the tube. Such a setup should also have a square tube profile or a much larger tube diameter to capture detailed structures in the boiling front.

References

1. Abbasi, T., Abbasi, S.A.: The boiling liquid expanding vapour explosion (BLEVE): mechanism, consequence assessment, management. J. Hazard. Mater. **141**, 489–519 (2007). doi:10.1016/j.jhazmat.2006.09.056
2. Hill, L.G.: An experimental study of evaporation waves in a superheated liquid. Dissertation (Ph.D.), California Institute of Technology (1990)
3. Simoes-Moreira, J.R., Shepherd, J.E.: Evaporation waves in superheated dodecane. J. Fluid Mech. **382**, 63–86 (1999). doi:10.1017/S0022112098003796
4. Reinke, P., Yadigaroglu, G.: Explosive vaporization of superheated liquids by boiling fronts. Int. J. Multiph. Flow **27**, 1487–1516 (2001). doi:10.1016/S0301-9322(01)00023-4
5. Bjerketvedt, D., Egeberg, K., Ke, W., Gaathaug, A., Vaagsaether, K., Nilsen, S.H.: Boiling liquid expanding vapour explosion in CO2 small scale experiments. Energy Procedia **4**, 2285–2292 (2011). doi:10.1016/j.egypro.2011.02.118
6. Saurel, R., Abgrall, R.: A multiphase Godunov method for compressible multifluid and multiphase flows. J. Comput. Phys. **150**, 425–467 (1999). doi:10.1006/jcph.1999.6187
7. Saurel, R., Petitpas, F., Abgrall, R.: Modelling phase transition in metastable liquids: application to cavitating and flashing flows. J. Fluid Mech. **607**, 313–350 (2008). doi:10.1017/S0022112008002061
8. Zein, A., Hantke, M., Warnecke, G.: Modeling phase transition for compressible two-phase flows applied to metastable liquids. J.

Comput. Phys. **229**, 2964–2998 (2010). doi:10.1016/j.jcp.2009.12.026

9. Pinhasi, G.A., Ullmann, A., Dayan, A.: 1D plane numerical model for boiling liquid expanding vapor explosion (BLEVE). Int. J. Heat Mass Transf. **50**, 4780–4795 (2007). doi:10.1016/j.ijheatmasstransfer.2007.03.016
10. Voort, M.M., Berg, A.C., Roekaerts, D.J.E.M., Xie, M., Bruijn, P.C.J.: Blast from explosive evaporation of carbon dioxide: experiment, modeling and physics. Shock Waves **22**, 129–140 (2012). doi:10.1007/s00193-012-0356-0
11. Xie, M.: Thermodynamic and Gasdynamic Aspects of a Boiling Liquid Expanding Vapour Explosion. PhD Thesis, Delft University of Technology, The Netherlands (2013)
12. Simoes-Moreira, J.R.: Oblique evaporation waves. Shock Waves **10**, 229–234 (2000). doi:10.1007/s001930000050
13. Span, R., Wagner, W.: A new equation of state for carbon dioxide covering the fluid region from the triple-point temperature to 1100 K at pressures up to 800 MPa. J. Phys. Chem. Ref. Data **25**, 1509–1596 (1996)

Modelling and Simulation of Phase Transition in Compressed Liquefied CO_2

Sindre Tosse, Per Morten Hansen and Knut Vaagsaether
Department of Process, Energy and Environmental Technology
University College of Southeast Norway
3918 Porsgrunn, Norway
Email: knut.vagsather@hit.no

***Abstract*—A model and solution method for phase transition in compressed liquefied gases is presented. The model is a two-phase 6-equation model with a common flow velocity for the two phases. The numerical method for solving the model is based on the 2. order shock capturing MUSCL-scheme with a HLLC Riemann solver. The van der Waal cubic equation of state is used for closing the set of equations. The phase transition model is based on thermodynamic and mechanical relaxation between the phases. The goal of the work is to present a numerical model capable of resolving the two-phase flow situation in the depressurization of a vessel or pipe containing liquefied CO_2. Simulation of expansion and phase transition in pressurized liquefied CO_2 is presented and compared with experimental data. The simulations are with a one dimensional geometry and the experiments are performed in a narrow tube. Wall effects in the experiments are not captured in the simulations. The wave structure seen in the experiments is reproduced by the simulation although not quantitatively. The simulations show that the fluid is in the metastable region before it undergoes a phase transition. The level of expansion of the metastable liquid shown in the in the simulations is not seen in the experiments.**

***Keywords*-Phase transition, liquefied gas, BLEVE, van der Waal, MUSCL**

I. Introduction

The focus of this paper is to present a numerical model capable of resolving the two-phase flow situation in the depressurization of a vessel or pipe containing liquefied CO_2. The methodology is attended for use with all types of liquefied pressurized gases. Sublimation of solid particles will not be addressed, since liquid-vapour interaction is the dominant process inside and in the immediate vicinity of the vessel. In order to get the necessary level of accuracy in the thermodynamic calculations, a non-monotonic equation of state is chosen. For CO_2, the most accurate liquid-vapour EOS available is the Span-Wagner multiparameter EOS [1]. It would be extremely challenging to implement this type of EOS into a numerical code, but the authors regards this as the end-goal of the present work. The usage of a non-monotonic EOS in a numerical solver raises a number of issues, since both the liquid and vapour states have a limited region of existence. In order to deal with these issues, the simplest form of a non-monotonic EOS, namely the cubic van der Waals EOS, is used in the development of a numerical code. Menikoff and Plohr [2] state that the Maxwell equal-area rule must be applied to modify the equation of state in order to avoid imaginary speed of sound in the van der Waals loop. Saurel et al. [3] propagate the misconception that the square speed of sound is negative in the spinodal zone. In the present work however, a less strict method is applied to allow metastable states, while maintaining a real speed of sound. While quantitatively inaccurate, the van der Waals equation of state provides a qualitative representation of every major feature of real gas behavior. Combined with its simple formulation, this makes it an often used EOS in model development and academic work. Using a non-monotonic equation of state in a numerical solver raises a number of issues. It is therefore necessary to develop robust solving algorithms that are capable of handling two phase flow in the vicinity of spinodal states. The van der Waals EOS is chosen to develop a proof of concept, because its simple formulation allows for analytical expressions for many thermodynamic parameters, e.g. the spinodal curve. Most compressible two-phase solvers use some form of stiffened gas equation of state or a more generalized Mie Gruneisen form equation of state. Even though it can be written on Mie-Gruneisen form, the van der Waals equation of state has been little used in the context of fluid dynamics. Slemrod [4] analyzed the dynamic phase transitions in a van der Waals fluid. Zheng et al. [5] used an interface capturing method with a generalized equation of state on the Mie-Gruneisen form where, among others, the van der Waals equation of state was used. To the authors knowledge, no solvers allowing metastable two-phase compressible flow with phase transition using the van der Waals equation of state exists.

Some work has been done to develop numerical models that are capable of describing evaporation waves. Saurel et al. [6] developed a Godunov method for compressible multiphase flow that was later applied to the subject of phase transition in metastable liquids [3]. They were able to qualitatively reproduce the evaporation front velocities measured by Simoes-Moreira and Shepherd [7]. In recent years, there have been several attempts to model BLEVE-type scenarios [8], [9], [10].

A. Metastable liquids

Figure 1 shows the pressure-volume diagram of CO_2 calculated from the Span-Wagner EOS. The spinodal curve is defined as $\left(\frac{\partial p}{\partial v}\right)_T = 0$ and is seen as an absolute boundary for an expanding liquid state. In the region between the liquid saturation curve and the spinodal curve a metastable liquid can exist. A metastable liquid is not in an equilibrium condition and a fluid can only stay in such a state for very short times. During a rapid expansion

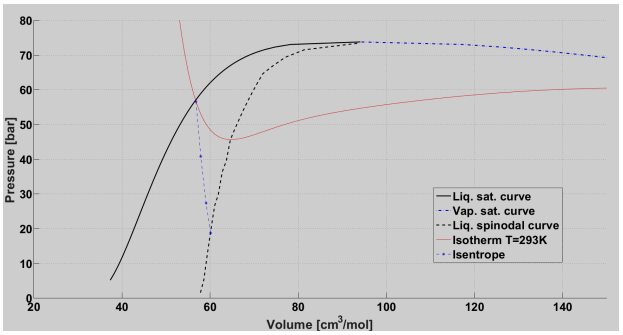

Figure 1. Pressure-volume diagram for CO_2 showing saturation curve, spinodal curve, an isotherm and an isentrope.

of a compressed liquefied gas metastable liquid states will occur behind propagating expansion waves before phase transition forces the thermodynamic state to change towards equilibrium conditions.

II. Model for two phase flow and phase transition

The numerical model used in this work solves the two-pressure 6-equation model given by Saurel et al [11]. Without heat and mass transfer, the model reads:

$$\frac{\partial \alpha_1}{\partial t} + u\frac{\partial \alpha_1}{\partial x} = \mu(p_1 - p_2), \tag{1}$$

$$\frac{\partial \alpha_1 \rho_1}{\partial t} + \frac{\partial \alpha_1 \rho_1 u}{\partial x} = 0, \tag{2}$$

$$\frac{\partial \alpha_2 \rho_2}{\partial t} + \frac{\partial \alpha_2 \rho_2 u}{\partial x} = 0, \tag{3}$$

$$\frac{\partial \rho u}{\partial t} + \frac{\partial \rho u^2 + (\alpha_1 p_1 + \alpha_2 p_2)}{\partial x} = 0, \tag{4}$$

$$\frac{\partial \alpha_1 \rho_1 e_1}{\partial t} + \frac{\partial \alpha_1 \rho_1 e_1 u}{\partial x} + \alpha_1 p_1 \frac{\partial u}{\partial x} = -p_I \mu (p_1 - p_2), \tag{5}$$

$$\frac{\partial \alpha_2 \rho_2 e_2}{\partial t} + \frac{\partial \alpha_2 \rho_2 e_2 u}{\partial x} + \alpha_2 p_2 \frac{\partial u}{\partial x} = p_I \mu (p_1 - p_2). \tag{6}$$

The right hand side terms corresponds to pressure relaxation. p_I is the interfacial pressure, estimated by

$$p_I = \frac{Z_2 p_1 + Z_1 p_2}{Z_1 + Z_2}, \tag{7}$$

where $Z_k = \rho_k c_k$ is the acoustic impedance of phase k. Where α_k is the volume fraction of phase k, ρ_k is the density of phase k, p_k is the pressure of phase k, e_k is the specific internal energy of phase k, Y_k is the mass fraction of phase k, c_k is the speed of sound of phase k, μ is the dynamic compaction viscosity and determines the rate of pressure relaxation, u is the flow velocity and an infinitesimal relaxation time, or large enough drag, is assumed leading to a common velocity between the phases. Phase 1 and phase 2 is vapour and liquid respectively. The mixture speed of sound used in this model is the frozen speed of sound,

$$c_f^2 = Y_1 c_1^2 + Y_2 c_2^2. \tag{8}$$

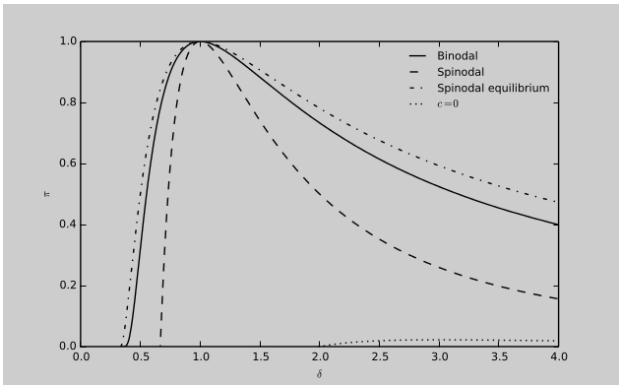

Figure 2. The binodal, spinodal and spinodal equilibrium curves of a van der Waals fluid in $\pi - \delta$ (reduced pressure and volume) space. The loci of zero speed of sound are also shown.

In the present work, we use stiff pressure relaxation ($\mu \to \infty$). As shown in [11], this means the recovery of the 5-equation model. Then the model is strictly hyperbolic with wave speeds $(u + c_f, u - c_f, u)$.

A. The van der Waals equation of state

The van der Waals equation of state (vdW-EOS) is the simplest form of a cubic equation of state. It is classified as cubic because it can be written on the form

$$v^3 + a_2 v^2 + a_1 v + a_0 = 0 \tag{9}$$

where v is the specific volume and a_k are pressure and/or temperature dependent coefficients. The vdW-EOS can be derived from the ideal gas EOS by adding correction terms for the excluded volume occupied by finite-sized particles and inter-molecular forces. On its classical form, the vdW-EOS reads

$$\left(p + \frac{n^2 a}{V^2}\right)(V - nb) = nR_M T \tag{10}$$

where n is the number of moles occupying the volume V at pressure p and temperature T. R_M is the ideal gas constant. a is a measure of the attraction between particles and b is the volume excluded by one mole of particles (molecules). As the volume tends to infinity, the vdW-EOS converges to the ideal gas law. The special case of $V = nb$ corresponds to a situation where the volume V is completely filled by the particles. At this point, the pressure tends to infinity. This implies that the van der Waals equation of state is only valid for $V > nb$. In terms of the volume at the critical point, this limit can be written as $\frac{v}{v_c} > \frac{1}{3}$.

Figure 2 shows the binodal, spinodal and spinodal equilibrium curves of a van der Waals fluid.

III. Solver

The equation set is solved by the 2. order accurate shock capturing MUSCL-scheme (Monotone Upstream-centered Scheme for Conservation Laws) combined with a HLLC (Harten Lax vanLeer Contact) Riemann solver for the interfacial fluxes [12]. This solver is used for the

hyperbolic part of the equation set i.e. the left hand side of equations 2 to 6.

The shock capturing method with the approximate Riemann solver solves shock waves and contact surfaces as very steep gradients with a numerical diffusion of a shock or contact discontinuity thickness of usually three control volumes. The equation set is closed by the van der Waals equation of state. The time step is variable and controlled by the Courant-Friedrich-Levy number.

A. Stiff pressure relaxation

The pressure relaxation step solves the equation set

$$\frac{\partial \alpha_1}{\partial t} = \mu(p_1 - p_2), \tag{11}$$

$$\frac{\partial \alpha_1 \rho_1 e_1}{\partial t} = -p_I \mu(p_1 - p_2), \tag{12}$$

$$\frac{\partial \alpha_2 \rho_2 e_2}{\partial t} = p_I \mu(p_1 - p_2) \tag{13}$$

in the limit $\mu \to \infty$. All other conserved variable groups are held constant during the relaxation step. According to [11], this system of equations can be replaced by

$$e_k(p, v_k) - e_k^0(p_k^0, v_k^0) + \hat{p}_I(v_k - v_k^0) = 0,\ k = 1, 2 \tag{14}$$

and the saturation constraint

$$(\alpha\rho)_1 v_1 + (\alpha\rho)_2 v_2 = 1 \tag{15}$$

where $(\alpha\rho)_k$ is constant during the relaxation step. The system can be closed by the van der Waal equation of state $e_k(\rho_k, p_k)$. Equation 14 can then be reformulated to $v_k(p)$ by using an estimate of $\hat{p}_I$. In the present work, the estimation $\hat{p}_I = p_I^0$ is used, but other estimates can also be used as shown by [11]. Finally, we insert the expressions for v_k into eq. 15 and solve for p.

Since the pressure estimated by this method is not guaranteed to be in agreement with the mixture equation of state $p(\rho, e, \alpha_1)$, this pressure is only used to find the relaxed volume fraction α_1. The relaxed pressure is then determined by the mixture equation of state and the internal energy from the redundant total energy equation. The conserved variables $(\alpha\rho e)_k$ are then re-initialized using the relaxed pressure and volume fraction. This ensures the conservation of mixture energy in the flow field.

Alternate relaxation methods can also be used. Both isentropic and isenthalpic relaxation methods has been tested with the same results as the method described here. This gives reason to assume that the thermodynamic relaxation path is of lesser importance, since it is only used to estimate the relaxed volume fraction. If the numerical method is expanded to a more complex EOS, this means that the pressure relaxation process most likely can be resolved with a less rigorous estimate of the thermodynamic relaxation path.

With the reduced vdW-EOS, eq. 14 can be written as

$$\pi(\delta_k) = \frac{2C_k\delta_k^2\hat{\pi}_I - 2\delta_k^3\hat{\pi}_I - 3\delta_k + 3}{\delta_k^2(3\delta_k - 1)}, \tag{16}$$

where

$$C_k = \delta_k^0 + \frac{1}{\hat{\pi}_I}\left[\frac{1}{2}(\pi_k^0 + \frac{3}{(\delta_k^0)^2})(3\delta_k^0 - 1) - \frac{3}{\delta_k^0}\right]. \tag{17}$$

Since we have no mass transfer, we can write

$$G_1\delta_1 + G_2\delta_2 = 1. \tag{18}$$

where $G_k = (\alpha\rho)_k v_c$. From this, we get

$$\delta_2(\delta_1) = \frac{1 - G_1\delta_1}{G_2} \tag{19}$$

The algorithm for stiff pressure relaxation solves the equation $f(\delta_1) = 0$ by the Newton-Raphson method, where

$$f(\delta_1) = \pi_1(\delta_1) - \pi_2(\delta_1),$$
$$\frac{\mathrm{d}\pi_k}{\mathrm{d}\delta_1} = \left(-\hat{\pi}_I\frac{6C_k - 2}{(3\delta_k - 1)^2} + \frac{6(3\delta_k^2 - 5\delta_k + 1)}{\delta_k^3(3\delta_k - 1)^2}\right)d_k,$$
$$d_1 = 1,\ d_2 = -\frac{G_1}{G_2}$$

Where π is reduced pressure and δ is reduced volume.

B. Stiff thermodynamic relaxation

The thermodynamic relaxation method used presently differs somewhat from the methods used by [3] and [13]. It is simpler in formulation and relatively easy to implement for any equation of state. We consider a two phase system with total density $\rho = \alpha_1\rho_1 + \alpha_2\rho_2$ and total internal energy $e = Y_1e_1 + Y_2e_2$. Since no mass or heat is added to the system during the relaxation step, these mixture properties are constant. We will consider the velocity of the two phases to be equal and constant during the relaxation step. Initially, the system is closed by the known variables ρ_1, ρ_2, e_1, e_2. In the numerical solver used presently, the two phases will be in mechanical equilibrium at the start of the relaxation step, but this is not a prerequisite of the procedure. The system can be uniquely determined by requiring complete thermodynamic equilibrium between the two phases:

$$p_1 = p_2 = p,\ T_1 = T_2 = T,\ g_1 = g_2 = g. \tag{20}$$

Where g is the Gibbs free energy. Note that this requirement is not possible for all ρ and e. This is indeed the case when there is only a single phase solution, that is when the limit of complete evaporation or condensation is reached. Since the numerical method is only valid for $\alpha_k > \xi$, where ξ is some small number (typically $\xi = 10^{-6}$), the single phase limit of phase 1 will be determined by

$$p_1 = p_2 = p,\ T_1 = T_2 = T,\ \alpha_1 = 1 - \xi \tag{21}$$

and equivalent for the single phase limit of phase 2. If a cubic equation of state is used, even this is not possible for all ρ and e. This will be the case when one phase reaches the spinodal state before thermal equilibrium is reached. If phase 2 is at the spinodal state, the system is determined by

$$\begin{gathered} p_1 = p_2 = p_{\mathrm{spin}}(v_2) = p, \\ T_1 = T(v_1, p),\ T_2 = T_{\mathrm{spin}}(v_2),\ \alpha_1 = 1 - \xi \end{gathered} \tag{22}$$

Table I
INITIAL SIMULATION CONDITIONS

	$x < 0.25$ m	$0.25m \geq x$ $x < 0.5m$	$x \geq 0.5m$
$p\ [Pa]$	$5.5 \cdot 10^6$	$5.5 \cdot 10^6$	10^5
$u\ [m/s]$	0	0	0
α	10^{-6}	$1 - 10^{-6}$	$1 - 10^{-6}$
$\rho_1\ [kg/m^3]$	175.00	175.00	1.8794
$\rho_2\ [kg/m^3]$	530.45	565.46	565.46

v_2 is determined by the mixture equation of state, and v_1 is determined by conservation of mass ($v = Y_1 v_1 + Y_2 v_2$). The subscript $spin$ denotes the thermodynamic spinodal state.

In the context of the van der Waals EOS, the three cases (20, 21 and 22) can be identified by the values of ρ and e. A fourth case is theoretically possible, namely $e < e(\rho)_{T=0}$, but this is not likely to occur in numerical calculations and is therefore not further examined.

The stiff thermodynamic relaxation procedure was used when $p_l < p_{\text{sat}}(T_l)$. An additional criterion $\xi_I < \alpha_1 < 1 - \xi_I$ can be used, where ξ_I represents the interface limit of the volume fraction (typically $\xi_I = 10^2\xi$ to $10^3\xi$). This last criterion is referred to as the interface criterion of the thermodynamic relaxation procedure and is used to allow for the formation of metastable liquid.

IV. EXPERIMENTS

The capabilities of the model to predict phase transition in pressurized liquid CO_2 by expansion is validated by comparing simulation results with experimental results. The experimental results are presented in [14]. Figure 3 shows a drawing of a experimental apparatus for rapid expansion of liquefied CO_2. The expansion tube is 9 mm inner diameter, 1.5 mm wall thickness polycarbonate. Before the beginning of the experiment, the tube is filled to about half level with saturated liquid CO_2 at room temperature, about 20^{o}C. The pressure in the tube is then 5.5 MPa. The top of the tube is closed with a diaphragm which is punctured by an arrow, releasing CO_2 to the atmosphere. Expansion waves then propagates down the tube and starts a boiling process due to the falling pressure. The expansion tube is transparent and a high speed digital camera captures the expansion and boiling process on a high speed movie which is later analyzed. The camera operates at 20 000 fps for this experiment. Typical wave trajectories is shown in figure 4.

V. SIMULATION SET-UP

The simulation domain is shown with initial conditions in figure 5. The calculation was run with an initial CFL number set to 0.2 for the first 200 time steps. The CFL number was then linearly increased to 0.5 over 50 time steps and was set to 0.5 for the rest of the calculation. The initial conditions for the simulation is shown in table I. The one dimensional domain was divided into 7000 control volumes with 10^{-4} m length.

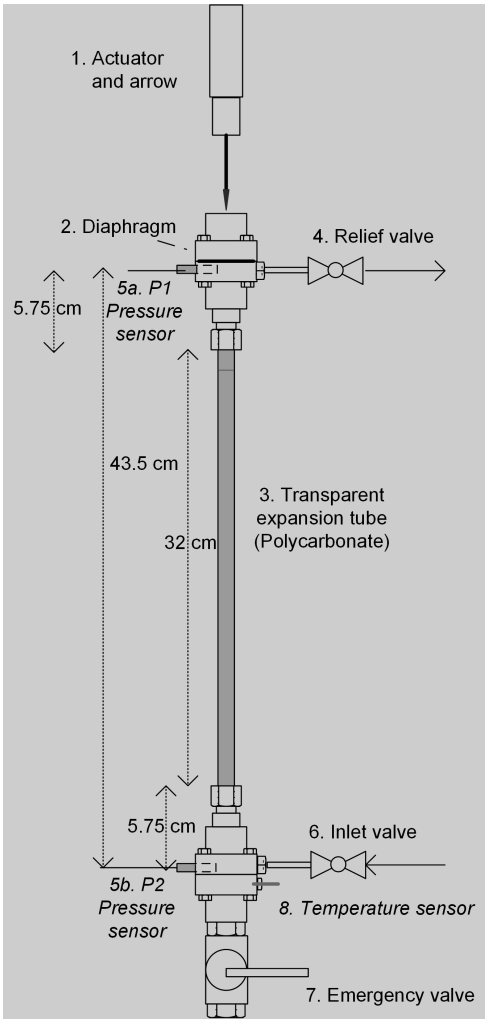

Figure 3. Experimental set-up.

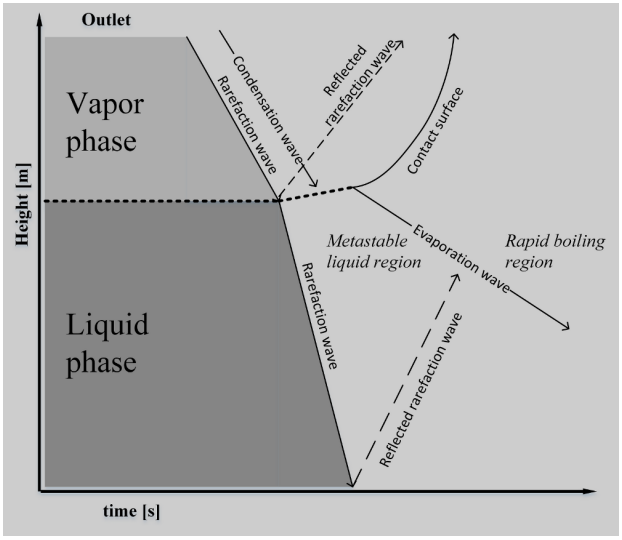

Figure 4. Schematic representation of the waves in the one dimensional expansion experiments.

VI. RESULTS AND DISCUSSION

The van der Waal EOS is not able to reproduce the thermodynamical states quantitatively, especially close to

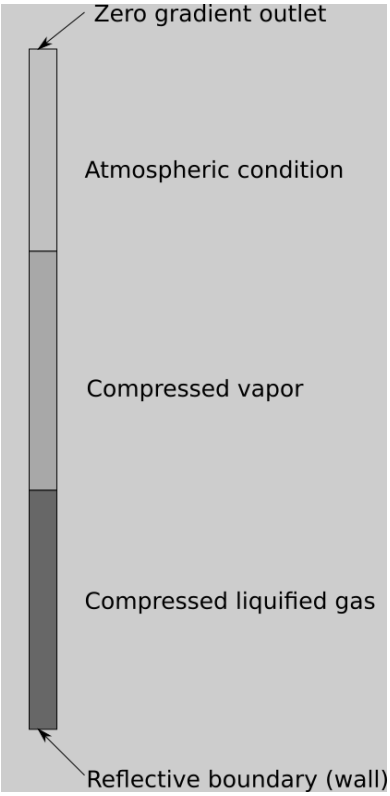

Figure 5. Initial and boundary conditions in the simulation domain.

saturation condition. The results are presented as scaled quantities to show the qualitative behaviour of the simulation method. The pressure is scaled with saturation pressure at initial temperature, ie. the initial pressure in the tube. The time is scaled by the average propagation time for an expansion wave along the total length of the pipe and the position is scaled by the tube length. The initial interphase in the experiments was 56 % of the tube length from the bottom. For comparison of the wave structures the interphase is moved to scaled position 0.5 like in the simulations. The wave structures in the experiments and simulations are shown as x-t diagrams. The experimental x-t diagram is extracted from the high speed movie. The pixel row from the central position of the tube is stacked along the time vector.

Figure 6 shows the simulated wave structure in the expansion tube. An initial expansion wave propagates downwards in the gas phase from scaled time 0. The expansion wave both reflects and transmits at the interphase, at scaled time 0.7, where the reflected wave is seen traveling upwards and the transmitted wave continues downwards into the liquid. A condensation phase transition occurs behind the reflected upwards traveling expansion wave. A phase transition in the liquid is initiated and the contact surface of the expanding liquid-gas mixture travels upwards following the reflected expansion wave. The expansion wave traveling through the liquid is reflected at the bottom of the tube and a faster phase transition is initiated there due to the high level of expansion. The phase transition initiated by the incident expansion wave is slow due to a

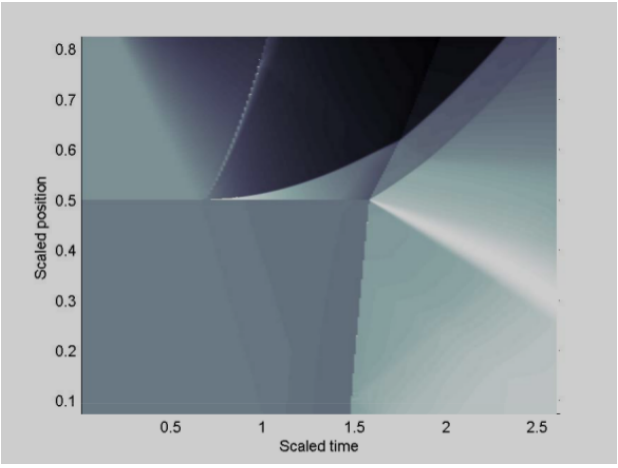

Figure 6. Scaled simulated density for expansion of CO_2 in 1D-domain. The results show the wave structure in the expansion process.

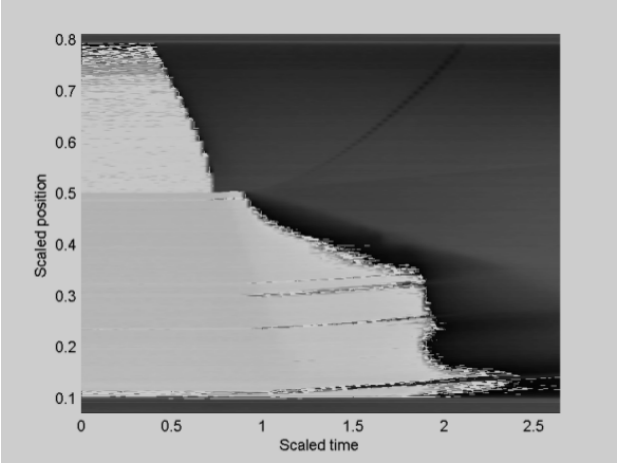

Figure 7. Experimental x-t diagram of expansion of CO_2 in a narrow tube. The results show the wave structure in the expansion process.

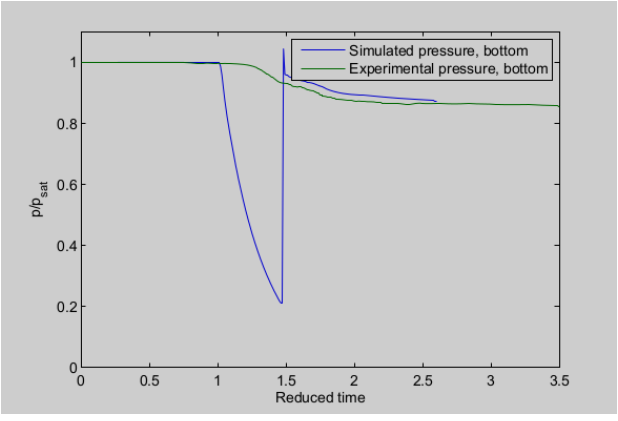

Figure 8. Simulated and experimental scaled pressure history at the bottom of the expansion tube.

low level of superheat. Once the expansion wave reflects at the bottom and again interactes with the initial interphase between liquid and vapour, at scaled time 1.6, a faster phase transition is triggered. Comparing these results to the experimental results seen in figure 7 shows the same

wave structures. In the experiments a condensation wave following the incident expansion wave occurs. This is not seen in the simulations. The reflected expansion wave is not clearly in seen in the experimental x-t diagram. The condensation seen in the simulations will not occur in experiments since the wave propagates into a two phase fluid.

Figure 8 shows the relative scaled pressure at the bottom of the tube vs. scaled time for simulation and experiment. The large drop in the simulated pressure, not seen in the experiments, is due to the expanding liquid. The thermodynamical state in the expansion wave is highly expanded metastable liquid. When the liquid pressure reaches the spinodal state at scaled time 1.5, a very rapid phase transition occurs and brings the pressure up towards equilibrium pressure. This creates a shock wave propagating upwards due to the fast expansion in the boiling. This shock is driven by a sudden change in thermodynamic state to equilibrium. This rapid phase transition propagates with the mesh speed, ie. $\Delta x/\Delta t$ and is an artefact of the phase transition model. The experimental pressure values does not drop as dramatically as the simulated pressure. The reason for this discrepancy can be that nucleation sites along the narrow tube will force a faster phase transition in the metastable liquid and keep the pressure at a higher level. The wall effects are not included in the simulation. After the rapid phase transition and formation of the shock wave the simulated pressure is close to the experimental pressure.

VII. Conclusion

A model and solver for rapid phase transition in compressed liquefied gases is presented. The phase transition model uses a mechanical and thermodynamical relaxation approach for phase transition. The present model and solver is capable of handling the wave types that can occur in a depressurization process however the combination of the van der Waals equation of state and an ideal geometry in one dimension will not produce the quantitative values seen in the experiments. Wall effects and low accuracy of the EOS close to saturation conditions and in metastable state causes a higher degree of superheat before a rapid phase transition can occur in the simulations. When the metastable liquid reaches the spinodal state, the model produces an unphysically fast evaporation wave. Future work to improve the simulation method will be to develop a kinetic based phase transition model in highly expanded metastable liquids. Such a model can reduce the possibility of low pressures seen in the metastable liquid during the reflection of rarefaction waves. A kinetic based transition rate can include wall effects and effects from impurities in the liquid. For higher accuracy the present method can be extended to more complex equations of states, like the Span-Wagner EOS.

References

[1] R. Span and W. Wagner, "A new equation of state for carbon dioxide covering the fluid region from the triple-point temperature to 1100 K at pressures up to 800 MPa", Journal of Physical and Chemical Reference Data, 25(6):1509–1596, 1996.

[2] R. Menikoff and B.J. Plohr, "The Riemann Problem for Fluid-Flow of Real Materials", Reviews of Modern Physics, 61(1):75–130, 1989.

[3] R. Saurel, F. Petitpas, and R. Abgrall, "Modelling phase transition in metastable liquids: application to cavitating and flashing flows", Journal of Fluid Mechanics, 607:313–350, 2008.

[4] M. Slemrod, "Dynamic phase transitions in a van der Waals fluid", Journal of Differential Equations, 52(1):1–23, 1984.

[5] H. W. Zheng, C. Shu, Y. T. Chew, and N. Qin, "A solution adaptive simulation of compressible multi-fluid flows with general equation of state", International Journal for Numerical Methods in Fluids., 67(5):616–637, 2011.

[6] R. Saurel, and R. Abgrall, "A multiphase Godunov method for compressible multifluid and multiphase flows", Journal of Computational Physics, 150(2):425–467, 1999.

[7] J.R. Simoes-Moreira and J.E. Shepherd, "Evaporation waves in superheated dodecane", Journal Of Fluid Mechanics, 382:63–86, 1999.

[8] G. A. Pinhasi, A. Ullmann, and A. Dayan, "1D plane numerical model for boiling liquid expanding vapor explosion (BLEVE)", International Journal of Heat and Mass Transfer, 50(23-24):4780–4795, 2007.

[9] M. M. Voort, A. C. Berg, D. J. E. M. Roekaerts, M. Xie, and P. C. J. Bruijn, "Blast from explosive evaporation of carbon dioxide: experiment, modeling and physics", Shock Waves, 22(2):129–140, 2012.

[10] M. Xie, "Thermodynamic and Gasdynamic Aspects of a Boiling Liquid Expanding Vapour Explosion", PhD thesis, Delft University of Technology, 2013.

[11] R. Saurel, F. Petitpas, and R. A. Berry, "Simple and efficient relaxation methods for interfaces separating compressible fluids, cavitating flows and shocks in multiphase mixtures", Journal of Computational Physics, 228(5):1678–1712, 2009.

[12] E. F. Toro, "Riemann solvers and numerical methods for fluid dynamics", Springer-Verlag, second edition, 1999.

[13] A. Zein, M. Hantke, and G. Warnecke, "Modeling phase transition for compressible two-phase flows applied to metastable liquids", Journal of Computational Physics, 229(8):2964–2998, 2010.

[14] P. M. Hansen, K. Vaagsaether, A. V. Gaathaug and D. Bjerketvedt, "CO_2 explosions - an experimental study of rapid phase transition", 8th International Seminar on Fire and Explosion Hazards, 25. – 28. April, Hefei, China, 2016.

Doctoral dissertation no. 20
2017

—

The rapid depressurization and evaporation of liquified carbon dioxide

Dissertation for the degree of Ph.D

—

Sindre Tøsse

—

ISBN 978-82-7206-435-7
ISSN 2464-2770

usn.no